A lattice model for prediction of ice failure in interaction with sloping structures

van Vliet, Renate

DOI
10.4233/uuid:4d27776a-9fe3-409e-8066-33b861792ba2

Publication date
2018

Document Version
Final published version

Citation (APA)
van Vliet, R. (2018). *A lattice model for prediction of ice failure in interaction with sloping structures*. [Dissertation (TU Delft), Delft University of Technology]. https://doi.org/10.4233/uuid:4d27776a-9fe3-409e-8066-33b861792ba2

A lattice model for prediction of ice failure in interaction with sloping structures

A lattice model for prediction of ice failure in interaction with sloping structures

Proefschrift

ter verkrijging van de graad van doctor
aan de Technische Universiteit Delft,
op gezag van de Rector Magnificus, prof. dr. ir. T.H.J.J. van der Hagen,
voorzitter van het College voor Promoties,
in het openbaar te verdedigen op vrijdag 16 november 2018 om 12:30 uur

door

Renate VAN VLIET

civiel ingenieur Technische Universiteit Delft, Nederland
geboren te Leiderdorp, Nederland.

Dit proefschrift is goedgekeurd door de promotor.

Samenstelling promotiecommissie bestaat uit:
Rector Magnificus, voorzitter
Prof. dr. A.V. Metrikine, Technische Universiteit Delft, promotor

Onafhankelijke leden:
Prof. dr. ir. J.G. Rots, Technische Universiteit Delft
Prof. dr. J. Tuhkuri, Aalto University, Finland
Prof. dr.-Ing. habil. H. Altenbach, Otto-von-Guericke-Universität Magdeburg, Duitsland
Prof. dr. ir. A. de Boer, Universiteit Twente
Prof. dr. K.V. Høyland, Norwegian University of Science and Technology, Noorwegen
Prof. dr. ir. S.N. Jonkman, Technische Universiteit Delft, reservelid

Overig lid:
Dr. ir. G.L. Kuiper, Shell Projects and Technology

Keywords: Lattice, ice, sloping structure, fracture

Printed by: Gildeprint

Front & Back: Kruiend ijs op de Houtribdijk tussen Enkhuizen en Lelystad, Januari 1996

ISBN 978-94-6366-092-1

An electronic version of this dissertation is available at
http://repository.tudelft.nl/

Contents

Summary

To study interaction between ice and sloping structures, numerical models are required that can predict failure of the ice based on physical ice properties, deformations and structural shape and size. An important element of these models is the set of failure criteria that is applied, as failure limits the loading of the ice on the structure. Failure in interaction with a sloping structure can occur in multi-directional tension, compression, bending, splitting or a combination of these, making it important to capture and combine all failure conditions in a single model. In this thesis, a lattice model is developed to simulate an ice plate and failure criteria are derived for the model, linked to field measurements and failure envelopes. Fracture patterns generated with the lattice model compare well with those observed in basin tests.

Lattice models are successfully used in modelling of fracture of brittle materials. To date, most of the lattice multi-dimensional (2D and 3D) models describe either in-plane or three-dimensional mechanics of the materials. Only a few lattice models are available in the literature for the description of the out-of-plane mechanics of plates. However, the parameters of those lattice models have not been linked to those of the classical plate models, such as Mindlin-Reissner plate theory, which is based on the classical continuum theory. To be able to simulate out-of-plane deformations of a plate, thereby enabling physically correct simulation of ice-structure interaction, a 2-dimensional lattice model is developed that reproduces the out-of-plane dynamics of a shear-deformable plate in the low frequency band. The developed model is composed of masses and springs whose morphology and properties were derived to match the out-of-plane deformations of thick plates as described by the Mindlin-Reissner theory. Bending, shear and torsion are taken into account. The eigenfrequencies and the steady-state response of the model to a sinusoidal-in-time point load are computed and compared to those of a corresponding continuum plate. It is proven that the developed lattice predicts the same dynamic behaviour as the corresponding continuum plate at relatively low frequencies, which are dominant in ice-structure interaction processes. At higher frequencies deviations occur. These are discussed in terms of the dispersion, anisotropy and specific boundary effects of the lattice model.

A lattice model for in-plane vibrations of a plate in plane strain conditions is described in literature and is adjusted in the current work to plane stress conditions and to reproduce the Poisson effect. Combined with the lattice model for out-of-plane deformations a single model is formed, which captures in- and out-of-plane deformation of a shear deformable plate under the assumption of small deformations.

Failure criteria were developed for the lattice model which are linked to field measurement data of ice. The deformation and failure criteria in the lattice model are based on first principles, enabling physically sound simulation of deformation and fracture processes of the ice plate material. Failure in compression, tension, bending and splitting are simulated with the lattice model, providing a complete set of failure scenarios relevant to study interaction between ice and sloping structures. It is shown that the criteria have minimal dependence on cell size and orientation and are applicable for multi-directional loading conditions. By means of numerical assessment, a multitude of structures and loading conditions can be analysed and structural shapes can be optimized for interaction with ice at reasonable costs.

Validation of the model against field measurements for ice in complex loading conditions of combined bending, shear and torsion as well as basin tests show that fracture location and fracture patterns can be predicted well with the lattice model. A 3-dimensional model, which would reduce computational efficiency, is required to accurately simulate out-of-plane shear and spalling failure of the ice, however in engineering applications these are often not governing over bending and tensile failure. Inclusion of ice rubbling and clearance processes as well as improving the simulation of the contact with a structure would further improve the model and ice load predictions.

Samenvatting

Om interactie tussen ijs en schuin aflopende constructies te bestuderen zijn numerieke modellen vereist, waarmee het breken van het ijs kan worden voorspeld, gebaseerd op fysieke eigenschappen en vervormingen van het ijs en de vorm en afmetingen van de constructie. Een belangrijk element van deze modellen zijn de criteria die worden toegepast voor het breken van het ijs, gezien dit de interactie-krachten tussen het ijs en de constructie limiteert. Het falen van ijs in interactie met een schuin aflopende constructie kan voorkomen in multidirectionele trek, druk, buiging, splijting of een combinatie hiervan, waardoor het belangrijk is om alle condities waarin het ijs kan falen in één model te combineren. Een raster-model is ontwikkeld in dit proefschrift, waarmee een ijsplaat kan worden gesimuleerd. Criteria voor het breken zijn ontwikkeld voor het model en gelinkt aan meetdata uit het veld en breuk-diagrammen. De breekpatronen die met het raster-model worden gegenereerd komen goed overeen met patronen die in modeltesten zijn geobserveerd.

Rastermodellen zijn succesvol gebruikt voor het modelleren van het breken van brosse materialen. Tot nu toe beschrijven de meeste multidimensionele (2D en 3D) modellen de mechanica van de plaat ofwel in het vlak van de plaat, ofwel in drie dimensies. Slechts een klein aantal rastermodellen zijn beschikbaar in de literatuur waarmee de mechanica uit het vlak van de plaat wordt beschreven. De parameters van deze rastermodellen zijn echter niet gelinkt aan die van klassieke plaat modellen, zoals de Mindlin-Reissner theorie die gebaseerd is op klassieke continuüm theorie. Om vervormingen uit het vlak van de plaat te kunnen simuleren, zodat interactie tussen ijs en constructies op fysisch correcte wijze kan worden gesimuleerd, is een 2-dimensionaal rastermodel ontwikkeld, dat de dynamica van een in afschuiving vervormbare plaat kan reproduceren voor lage frequenties. Het model bestaat uit massa's en veren waarvan de morfologie en eigenschappen zijn afgeleid zodat de vervormingen uit het vlak van een dikke plaat, zoals beschreven in de Mindlin-Reissner theorie, worden geëvenaard. Buiging, afschuiving en torsie zijn hierin meegenomen. De eigenfrequenties en reactie van het model op een puntbelasting die sinusvormig is in tijd zijn berekend en vergeleken met die van een overeenkomstige continue plaat. Het is bewezen dat het ontwikkelde rastermodel hetzelfde dynamische gedrag voorspelt als het continue model bij relatief lage frequenties, welke dominant zijn in de interactie tussen ijs en constructies. Bij hogere frequenties treden afwijkingen op. Deze worden besproken in termen van dispersie, anisotropie en randeffecten in het rastermodel.

Een rastermodel voor het simuleren van vibraties in het vlak van een plaat is beschreven in literatuur en aangepast in dit proefschrift om een ijsplaat te simuleren en om het Poisson effect te kunnen reproduceren. Gecombineerd met het rastermodel voor vervormingen uit het vlak van de plaat, is een model gevormd dat zowel vervormingen in het vlak als uit het vlak van een in afschuiving vervormbare plaat beschrijft, voor condities met relatief kleine vervormingen.

Criteria voor het breken van ijs die gelinkt zijn aan meetdata uit het veld zijn ontwikkeld in dit onderzoek. De vervorming en breek-criteria in het rastermodel zijn gebaseerd op basisprinciepen, waardoor fysisch correctie simulaties van vervormingen en breek-processen van de ijsplaat kunnen worden uitgevoerd. Breken in druk, trek, buiging en splijten worden gesimuleerd met het rastermodel, zodat een complete set van breek-scenario's die relevant zijn om interactie tussen ijs en een schuin aflopende constructie te bestuderen wordt geleverd. De breek-criteria hebben een minimale afhankelijkheid van de afmetingen en oriëntatie van de cellen in het rastermodel en zijn toepasbaar in multidirectionele belastingscondities. Door middel van numerieke simulatie kan een meervoud aan constructies en belastingscondities worden geanalyseerd en kan de vormgeving van een constructie worden geoptimaliseerd voor interactie met ijs tegen redelijke kosten.

Validatie van het model met veld-metingen van ijs in complexe belastingscondities van gecombineerde buiging, afschuiving en torsie en met schaalmodel-testen laten zien dat de locatie en breukpatronen van ijs goed kunnen worden voorspeld met het rastermodel. Een 3-dimensionaal model, wat de efficiëntie van de berekening zou reduceren, is nodig om afschuiving uit het vlak en afsplintering op accurate wijze te kunnen simuleren. In praktische toepassingen zijn deze condities echter veelal niet maatgevend vergeleken met breken in buiging en trek. Het toevoegen van het afbrokkelen van ijs en afvoer rondom de constructie en het verbeteren van de simulatie van het contact met een constructie zouden het model en voorspellingen van belasting door het ijs verder verbeteren.

1

Introduction

1.1 Background

In the past decades energy companies have been interested to build structures in Arctic environments due to the hydrocarbon potential. Since recent years, building structures in areas with potential presence of ice has become of interest to the offshore wind industry. Not only the energy industry is interested in building structures in (sub-) Arctic regions. Ice loads on for example bridges, piers, lighthouses and coastal protection should be accounted for in the design in areas where ice occurs. Structures in (sub-) Arctic environments are often designed with a sloping waterline shape to reduce ice loading compared to that on a vertical structure. The slope causes ice to fail in bending and as such limits the failure load of ice and with that the loading on the structure. Observations from model tests and full scale interaction show a combination of bending and splitting failure near the structure (Lu, 2014). To reduce risk of damaging and building costs of these structures it is desired to improve the prediction of ice loads acting on them.

ISO19906 (ISO, 2010), an internationally used design standard for Arctic offshore structures, describes the following methods to determine ice actions: full scale measurements, model experiments and theoretical methods (analytical or numerical). Limited full-scale measurements on sloping structures are available due to the complexity and costs to obtain these. Examples are the Kemi I lighthouse (Hoikkanen, 1985), the Confederation Bridge cone (Brown et al., 2010), platform JZ20-2 in the Bohai Bay (Li et al. 2003), the sloping barrier in the Caspian Sea (Croasdale et al., 2011) and circular drillship Kulluk (Wright, 2001). As model tests are less complicated and less costly than full scale measurements, quite a number of model test campaigns have been executed (for example Irani and Timco, 1993; Lau, 1999; Sodhi, 1995). Comfort et al. (1999) collected and analysed general trends of an extensive dataset of ice model tests for floating, moored structures for different ice conditions, test techniques and structure types. Theoretical models are often used in design as they are quick and inexpensive to apply. A review of differences in theoretical models that are prescribed by codes and standards for determination of level ice and ice ridge loads on sloping offshore structures was made by Bruun and Gudmestad (2006). Analytical models include the model developed by Croasdale (1980) which is based on an elastic beam on an elastic foundation. Later this model was modified to include three-dimensional effects as well as in-plane compression (Croasdale and Cammaert, 1994). Ralston (1977) used plastic analysis to determine the forces on a conical structure. Terms in the formulation are related to breaking of the ice sheet and broken ice pieces sliding over the surface of the cone. A model for wedge-shaped beams failing adjacently based on continuum theory of a semi-infinite plate resting on an elastic foundation was developed by Nevel (1992).

Several research institutes and companies have developed numerical assessment tools to study breaking of ice in interaction with sloping structures, in the form of 1D, 2D or 3D models. Aksnes (2010) and Wille, Kuiper, & Metrikine (2011) simulated bending failure of ice in interaction with a downward sloping conical structure using a beam model. As beam models are 1-dimensional, multi-directional loading cannot be simulated and the models are inaccurate in the prediction of loading frequencies and breaking length of the ice in case of circular or ship-shaped structures. Izumiyama et al. (1993) presented a numerical method to compute the ice forces on a faceted conical structure. Lubbad and Løset (2011) adopted the model of wedge-shaped beams by Nevel (1992) to simulate real-time ice-structure interaction. Ice failure was modelled in a similar manner in the SIBIS simulator by Metrikin et al. (2015) to study ice interacting with a floating drillship. Bonnemaire et al. (2014) employed a semi-empirical model to simulate the response of a moored floating structure in ice and Shi et al. (2016) applied a semi-empirical model to study dynamic ice–structure interaction of an offshore wind turbine in drifting level ice. A 1D finite element model with non-linear Timoshenko beam elements by Paavilainen et al. (2009) was extended to 2D by

Lilja et al. (2017b). In this model, a cohesive fracture model prevents stress singularities near the crack tip. It is used to simulate crack formation and propagation. Sand and Fransson (2006) used finite element analysis to determine ice loading on an upward sloping structure. Models based on discrete elements were applied in simulation of ice structure interaction and ice clearance around structures (Hansen and Løset, 1999a, 1999b; Herman, 2016; Hopkins, 2004; Lau, 2001; Ji et al. 2015; Liu and Ji 2017).

By using numerical models, loads on structures of various shapes and sizes and in different ice conditions could be assessed in a timely manner and at low costs compared to basin tests or full-scale measurements. An important step in improving numerical ice load prediction is to further develop the simulations of the breaking processes of the ice. Most of the models developed so far focus on correctly simulating one failure mode, for example bending or splitting. None of the models include failure criteria that correctly simulate failure of the ice in multi-directional loading. In addition, failure in discrete models could be dependent on the size or orientation of the cells of the mesh (Chen et al., 2014; Monette and Anderson, 1999). To enable accurate simulation of interaction between ice and sloping structures it is desired to develop a numerical model that can simulate in-plane as well as out-of-plane deformations and predict fracture based on physical ice parameters that can be measured in the ice field.

1.2 Development of a lattice model for multi-directional ice-fracture simulation

In this thesis, a lattice model is developed to simulate deformation and fracture of an ice plate in interaction with a structure. First, a lattice model for out-of-plane deformation of a shear-deformable plate is derived, with which the bending deformation and vibration of a thick ice plate in interaction with a structure can be simulated. An existing lattice model for in-plane vibrations of a plate in plane-strain conditions is adjusted to plane stress conditions and combined with the lattice model for out-of-plane deformations to a single model that captures in- and out-of-plane deformation under the assumption of geometrical linearity. Then failure criteria are developed for the lattice model which are applicable in multi-directional loading in compression, tension, bending and splitting, and which result in fracture behaviour with minimal dependence on cell-size and -orientation. The model and failure criteria are validated by simulating a basin test of interaction between ice floes of different size and shape and a sloping structure.

A lattice model was selected to simulate the ice because of its simplicity and properties that are advantageous for fracture simulation. In contrast to a continuum model, where stress and strain describe responses to structural loading, the cells in the lattice model consist of a single layer of masses and springs, which form connections to neighbouring cells and, by assigning particular mass and spring stiffness, represent the reactivity to loading or deformation of a material. Stress singularities that occur near the crack tip in a continuum model (see for example Sih (1977)) cannot occur in the lattice structure. Simulation of failure is done by removing connections from the lattice model, such that re-meshing is not required.

Development of lattice models starts with Hrennikoff (1940), who used a framework of elastic bars to describe two-dimensional stress problems and static bending of thin plates. Woźniak (1970) analysed a framework of beams, taking account of curvature change of spring bond connections between the nodes. Later, lattice models based on bar and beam connections between nodes were applied in fracture mechanics studies of, for example, particle composites that are loaded in uni- or multi-axial tension or compression (Bolander et al., 1996; Herrmann and Roux, 1990; Lilliu and van Mier, 2007; Schlangen and van Mier, 1992; van Mier, 1986). Ostoja-Starzewski (1997) applied a two-dimensional spring network model to analyse damage patterns and constitutive responses of matrix-inclusion composites.

The advantage of using springs in the lattice model rather than beams or bars is that bending, torsion and shear are decoupled. Ostoja-Starzewski (2008) presented an overview of basic concepts and applications of spring network models. Edvardsson and Uesaka (2010) and Attar et al. (2014) used one-dimensional lattice-spring models to study dynamics of the open-draw section in a paper machine and a cracked beam respectively. Suiker et al. (2001a and 2001b) used a lattice-spring model to study response to harmonically vibrating loads in the ballast layer of a railway track. This model was adopted in this thesis to plane stress conditions to simulate in-plane deformations of the ice plate. In Suiker et al. (2001c), a method is described to study the correspondence of a two-dimensional discrete lattice-spring model to a Cosserat continuum in the long wave approximation. Only a few lattice models are available in the literature for the description of the out-of-plane mechanics of plates and the parameters of those lattice models have not been linked to those of the classical plate models, such as Mindlin-Reissner plate theory, based on the classical continuum theory. To close this gap, in this study a lattice model is developed for out-of-plane vibration of a shear-deformable plate, to be applied in the analysis of mechanics of floating ice sheets. The model is verified by comparison of deflection and rotation to analytical results obtained for a simply supported plate on a Kelvin foundation under a sinusoidal point load.

In the past, lattice models have been successfully applied to simulate fracture of various materials, such as rock (Potyondy and Cundall, 2004) and concrete (Cusatis et al., 2003; Schlangen and Garboczi, 1997; van Mier et al., 2002). Several criteria for failure of the lattice elements have been used in these models, based on energy, force or strain. Jirasek and Bazant (1995) described different constitutive laws for breaking links in a lattice. Herrmann et al. (1989) derived a criterion for breaking lattice beams that was based on Von Mises' yielding criterion. The force stretching the bond and moments acting on the two ends contribute to the criterion. Dai and Frantziskonis (1994) used a failure stress criterion in connecting bars in a lattice structure to simulate fracture of brittle materials. In Attar et al. (2014) the effects of transverse open cracks in a lattice model of a Timoshenko beam, consisting of masses, rotational springs and shear springs, were modelled by decreasing the stiffness of the rotational springs at crack locations. Schlangen and Garboczi (1997) studied the influence of the type and orientation of lattice elements in application to fracture simulation of concrete.

To simulate sea-ice fracture, lattice models have been applied in in-plane and out-of-plane loading conditions. Sayed (1997) and Sayed and Timco (1998) used elastic and visco-elastic bonds in normal direction between the masses and applied a force limit as fracture criterion. Dorival, Metrikine, & Simone (2008) developed a lattice model to simulate ice crushing against a structure and used critical spring deformation as criterion for the onset of failure. A 3-dimensional lattice model to simulate deformation of ice in in-plane as well as out of plane loading conditions was presented by Van den Berg (2016), using translational and rotational springs in six degrees of freedom. None of the existing models accounts for failure in multi-directional tension, compression, bending and splitting at the same time. Therefore, new failure criteria are derived for the lattice model in this thesis.

The failure criteria that are derived in this study for a 2D lattice model for sea-ice, consider both in-plane and out-of-plane deformations. Ice property measurements and tests of ice in multi-axial plate compression, splitting, beam bending and combined bending and torsion are used to derive failure criteria. The failure criteria are based on first principles, enabling physically sound simulation of failure processes that occur in ice-structure interaction processes. Dependency on directionality of loading and mesh size are given special attention. It is shown that when stress concentrations are accounted for, various in- and out-of-plane loading conditions, irrespective of orientation of the lattice cells and including conditions with concentrating stresses, can be simulated with the lattice model.

To validate the lattice model and its failure criteria for simulation of ice-structure interaction, a bending test, a test with combined bending, shear and torsion, a splitting test and a basin test for ice floes of different shape and size in interaction with a downward sloping conical structure are simulated. Fracture patterns are predicted well with the lattice model. Collection of ice rubble near the structure and clearance processes are not simulated and therefore the loading of the ice on the structure predicted by the lattice model is lower than the loading measured in basin tests. This research is limited to simulating deformation and fracture of the ice. To simulate ice clearance processes, it is recommended to link the lattice model to existing models, for example Discrete Element Method (DEM), which has been successfully used to simulate ice clearance processes around structures.

Numerical simulations allow for assessment of a multitude of structural shapes and ice parameters at relatively low costs and time. With the development of the lattice model and failure criteria for ice-structure interaction in multi-directional loading conditions an important gap is closed in prediction of ice loading on a sloping structure. The lattice model properties and failure criteria are based on physical ice parameters that can be measured in the field, to enable physically sound simulation of fracture during ice-structure-interaction processes.

1.3 Thesis outline

This thesis is structured as follows:

Chapter 2 describes the derivation of the lattice model for out-of-plane vibrations of a shear-deformable plate, which is applied to model bending deformations of ice. The equations of motion of the cells in the lattice model and spring stiffness parameters were derived to match the continuum Mindlin-Reissner model in the long wave approximation. To verify the lattice model, its predictions are compared to analytical results obtained for a simply supported plate on a Kelvin foundation under a sinusoidal point load, with input parameters representative of a floating ice plate. Comparison is carried out in terms of the deflections and rotations. Eigenfrequencies of the lattice model are also studied and compared to the analytical figures based on the continuum theory. An expected discrepancy is observed at higher vibration frequencies, which is attributed to the dispersion, anisotropy and specific boundary effects of the lattice model. The dispersion and anisotropy are quantified by studying the angular-frequency characteristics of the wave propagation.

In Chapter 3 parameters of the lattice model are derived to include in-plane deformations. Study of the Poisson effect show discrepancies between theory and deformations found with the lattice model. Alternative spring stiffnesses for the lattice model are derived based on the method presented by Hrennikoff (1940), resulting in proper capturing of the Poisson effect. By repeating the dynamic verification exercise from Chapter 2, it is shown that for vibration frequencies associated with ice-structure-interaction the new parameters are equally well applicable to simulate deformations of the ice as those derived in Chapter 2. For Poisson's ratio of 1/3, which is often applied for sea ice, both methods give the same parameters for the lattice model. This parameter is used for continuation of the research, while the new stiffness parameters derived in this Chapter are used to quantify effects of Poisson's ratio.

In Chapter 4 failure criteria for the lattice model are derived, considering both in-plane and out-of-plane deformations. The criteria are based on first principles, enabling physically sound simulation of failure processes that occur in ice-structure interaction. The failure criteria are linked to ice property measurements and failure envelopes are presented. Near a crack tip, strains concentrate. After deriving failure criteria for an intact plate, strain concentrations are studied and special failure criteria for application near crack tips are derived and linked to field measurements, completing the set of failure criteria that is required to simulate ice-structure interaction scenarios. It is shown that the failure criteria give behaviour with minimal dependence on cell-size and -orientation. Field tests of splitting and bending failure of an ice plate are simulated to validate the failure criteria and to demonstrate how the criteria are applied.

In Chapter 5, the onset of failure is analysed for complex loading conditions: combined bending, shear and torsion, using the failure criteria derived in Chapter 4. To keep the number of nodes and that of the equations in the model limited, there is only one layer of particles in out-of-plane-direction of the plate. As a consequence of this, out-of-plane spalling failure under high confinement, which is described in literature, cannot be accurately simulated and a limiting failure cap is set for this failure mode in Chapter 4. Shear springs are present in the lattice model with which shear deformation in out-of-plane direction is simulated. In Chapter 5, it is shown that in case of dominating out-of-plane shear deformations, the level of strain in the out-of-plane shear springs could be used to define the onset of shear failure.

To further validate the lattice model and the failure criteria, interaction between ice and a downward sloping conical structure is simulated with the lattice model in Chapter 6 and compared with observations from basin tests. Fracture patterns in interaction with ice floes of different size and shape as well as failure loads are analysed, confirming the applicability of the lattice model for fracture simulation in interaction with a structure and indicating the requirement to simulate ice rubble and clearance processes as well as to further develop the contact simulation with the structure to improve the ice loading predictions.

In Chapter 7 the main findings of this study are summarized.

2

Derivation and verification of a lattice model for bending vibration of a plate

2.1 Introduction

In this Chapter, a lattice model for out-of-plane vibrations of a shear-deformable plate is derived, which is used to model bending deformations of ice. To verify the lattice model, its predictions are compared to analytical results obtained for a simply supported plate on a Kelvin foundation under a sinusoidal point load. Comparison is carried out in terms of the deflections and rotations. Eigenfrequencies of the lattice model are also studied and compared to the analytical figures based on the continuum theory. An expected discrepancy is observed at higher vibration frequencies, which is attributed to the dispersion, anisotropy

---

This chapter has been published in ZAMM **432**, 23 (2017) (van Vliet and Metrikine, 2017a). Parts of the publication have been moved to other Chapters for consistency.

and specific boundary effects of the lattice model. The dispersion and anisotropy are quantified by studying the angular-frequency characteristics of the wave propagation in the plate.

2.2 Governing equations

A plate is modelled with a square lattice of particles of mass M. Each particle is connected to eight neighbouring particles with bending, shear and torsional springs. This configuration is depicted in Figure 2-1. Three types of particles can be distinguished, namely (i) the inner particles, situated in the interior of the plate, (ii) the boundary particles, situated at the free edges and (iii) the corner particles, situated at the corners of the plate. For all three types of particles the equations of motion are derived in this section, considering the continuum limit, similar to previous work for various infinite lattice systems (Askar, 1985) and for in-plane vibrations of a finite layer of discrete particles (Suiker et al., 2001a, 2001c).

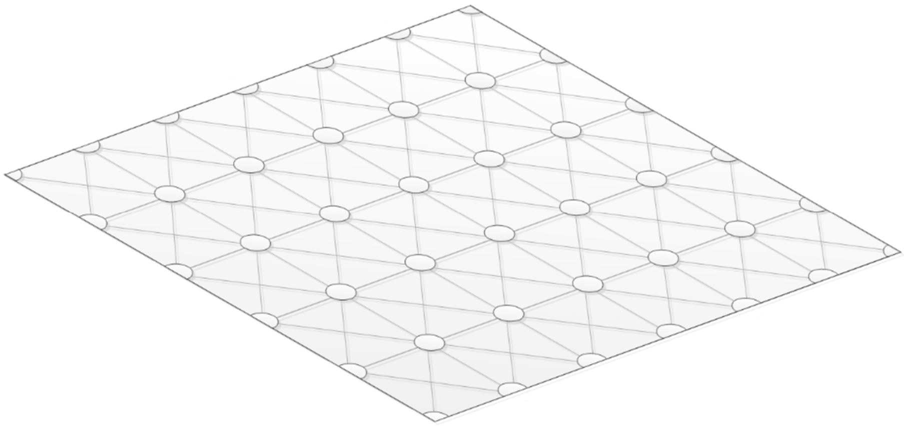

Figure 2-1: Rectangular plate, modelled with a square lattice of particles (masses). Spring connections between the masses are displayed as connecting lines

2.2.1 Equations of motion for an inner particle

Figure 2-2 shows an inner particle of the lattice. The particle position is characterized by indices (m,n) as indicated in Figure 2-2. Each particle is connected via axial springs to the nearest particles on the same horizontal and vertical axes, numbered 1 to 4 in Figure 2-2 and via diagonal springs to the nearest particles on the same diagonal axes, numbered 5 to 8 in Figure 2-2. Axial distance between the particles is d; diagonal distance is $d\sqrt{2}$. $K_{s,axi}$, $G_{r,axi}$ and $G_{t,axi}$ are the stiffnesses of the axial shear, bending and torsional springs respectively. $K_{s,dia}$, $G_{r,dia}$ and $G_{t,dia}$ are the stiffnesses of the diagonal shear, bending and torsional springs, respectively. The lattice structure and the axial and diagonal connections are depicted in Figure 2-3 and in Figure 2-4. The particles have three degrees of freedom: deflection w in the out-of-plane z-direction and rotations about the x-axis and y-axis $\{\varphi_y, \varphi_x\}$.

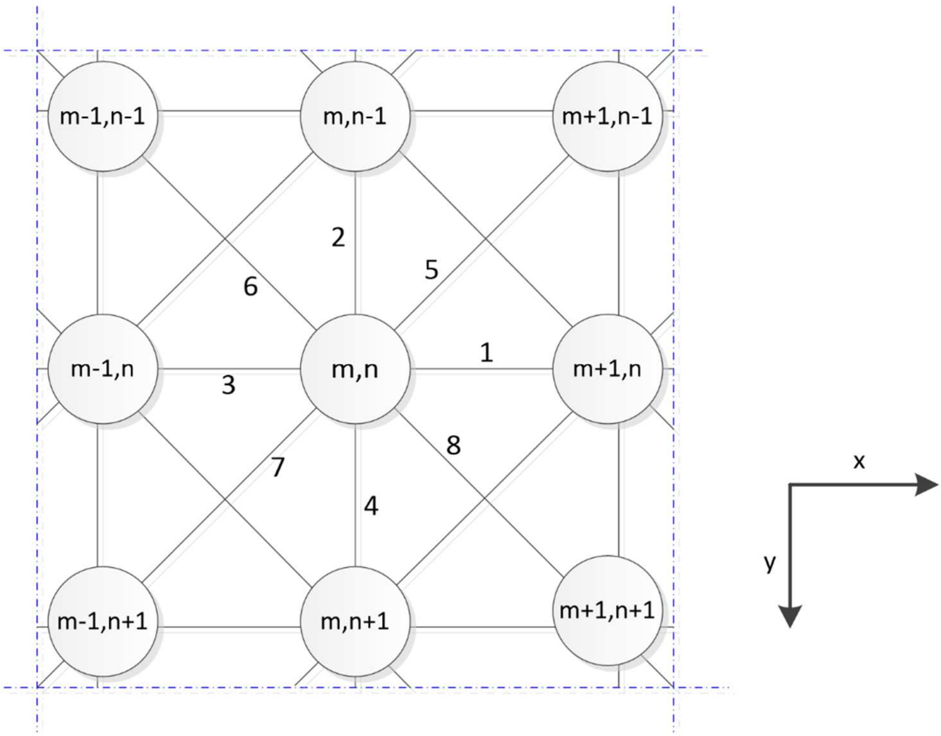

Figure 2-2: Node and connection numbering of the inner particle and its neighbouring particles

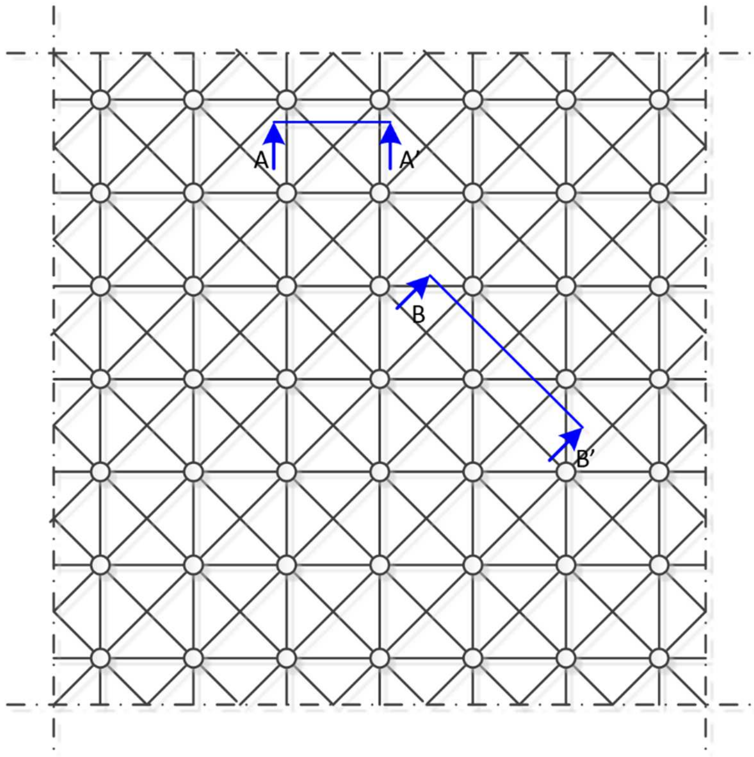

Figure 2-3: Structure of the lattice model; the circles represent lumped masses and the lines the connections between masses

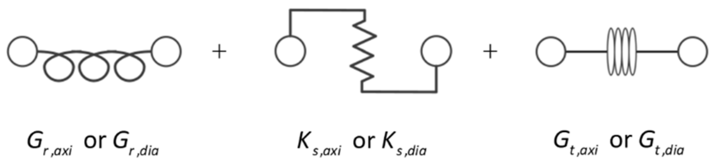

Figure 2-4: Axial and diagonal connections between the nodes in the lattice model, consisting of bending, shear and torsional springs (A-A' and B-B' in Figure 2-3)

Equations of motion for the particles in the plate will be obtained using the Lagrangian formalism. For the adopted lattice structure the Lagrangian function for the inner particle (m,n) and its connections can be written as:

$$L^{(m,n)} = E_{kin}{}^{(m,n)} - E_{pot}{}^{(m,n)}, \tag{2.1}$$

with the kinetic energy $E_{kin}{}^{(m,n)}$ and the potential energy $E_{pot}{}^{(m,n)}$. The potential energy for the inner particle is:

$$\begin{aligned} E_{pot}{}^{(m,n)} &= \frac{1}{2}\sum_{i=1}^{4}\left(\Delta s_{(i)}{}^2 K_{s,axi} + \Delta r_{(i)}{}^2 G_{r,axi} + \Delta p_{(i)}{}^2 G_{t,axi}\right) \\ &+ \frac{1}{2}\sum_{i=5}^{8}\left(\Delta s_{(i)}{}^2 K_{s,dia} + \Delta r_{(i)}{}^2 G_{r,dia} + \Delta p_{(i)}{}^2 G_{t,dia}\right), \end{aligned} \tag{2.2}$$

where $\Delta s_{(i)}$ is the elongation of shear spring i, $\Delta r_{(i)}$ is the rotation of the rotational spring i and $\Delta \mathrm{p}_{(i)}$ is the twist of the torsional spring i. The above-introduced deformations of the springs, in the linear approximation, can be described as:

$$\begin{aligned}
\Delta s_{(1)} &= w^{(m+1,n)} - w^{(m,n)} + \frac{1}{2}d\left(\varphi_x{}^{(m+1,n)} + \varphi_x{}^{(m,n)}\right) \\
\Delta s_{(2)} &= w^{(m,n)} - w^{(m,n-1)} + \frac{1}{2}d\left(\varphi_y{}^{(m,n-1)} + \varphi_y{}^{(m,n)}\right) \\
\Delta s_{(3)} &= w^{(m,n)} - w^{(m-1,n)} + \frac{1}{2}d\left(\varphi_x{}^{(m-1,n)} + \varphi_x{}^{(m,n)}\right) \\
\Delta s_{(4)} &= w^{(m,n+1)} - w^{(m,n)} + \frac{1}{2}d\left(\varphi_y{}^{(m,n+1)} + \varphi_y{}^{(m,n)}\right) \\
\Delta s_{(5)} &= w^{(m+1,n-1)} - w^{(m,n)} + \frac{1}{2}d\left(\varphi_x{}^{(m+1,n-1)} + \varphi_x{}^{(m,n)} - \varphi_y{}^{(m+1,n-1)} - \varphi_y{}^{(m,n)}\right) \\
\Delta s_{(6)} &= w^{(m,n)} - w^{(m-1,n-1)} + \frac{1}{2}d\left(\varphi_x{}^{(m-1,n-1)} + \varphi_x{}^{(m,n)} + \varphi_y{}^{(m-1,n-1)} + \varphi_y{}^{(m,n)}\right) \\
\Delta s_{(7)} &= w^{(m,n)} - w^{(m-1,n+1)} + \frac{1}{2}d\left(\varphi_x{}^{(m-1,n+1)} + \varphi_x{}^{(m,n)} - \varphi_y{}^{(m-1,n+1)} - \varphi_y{}^{(m,n)}\right) \\
\Delta s_{(8)} &= w^{(m+1,n+1)} - w^{(m,n)} + \frac{1}{2}d\left(\varphi_x{}^{(m+1,n+1)} + \varphi_x{}^{(m,n)} + \varphi_y{}^{(m+1,n+1)} + \varphi_y{}^{(m,n)}\right)
\end{aligned} \tag{2.3}$$

$$
\begin{aligned}
\Delta r_{(1)} &= \varphi_x{}^{(m+1,n)} - \varphi_x{}^{(m,n)} \\
\Delta r_{(2)} &= \varphi_y{}^{(m,n)} - \varphi_y{}^{(m,n-1)} \\
\Delta r_{(3)} &= \varphi_x{}^{(m,n)} - \varphi_x{}^{(m,n-1)} \\
\Delta r_{(4)} &= \varphi_y{}^{(m,n+1)} - \varphi_y{}^{(m,n)} \\
\Delta r_{(5)} &= \frac{1}{2}\sqrt{2}\left(\varphi_x{}^{(m+1,n-1)} - \varphi_x{}^{(m,n)} - \varphi_y{}^{(m+1,n-1)} + \varphi_y{}^{(m,n)}\right) \\
\Delta r_{(6)} &= \frac{1}{2}\sqrt{2}\left(\varphi_x{}^{(m,n)} - \varphi_x{}^{(m-1,n-1)} + \varphi_y{}^{(m,n)} - \varphi_y{}^{(m-1,n-1)}\right) \\
\Delta r_{(7)} &= \frac{1}{2}\sqrt{2}\left(\varphi_x{}^{(m,n)} - \varphi_x{}^{(m-1,n+1)} - \varphi_y{}^{(m,n)} + \varphi_y{}^{(m-1,n+1)}\right) \\
\Delta r_{(8)} &= \frac{1}{2}\sqrt{2}\left(\varphi_x{}^{(m+1,n+1)} - \varphi_x{}^{(m,n)} + \varphi_y{}^{(m+1,n+1)} - \varphi_y{}^{(m,n)}\right)
\end{aligned} \tag{2.4}
$$

$$
\begin{aligned}
\Delta p_{(1)} &= \varphi_y{}^{(m+1,n)} - \varphi_y{}^{(m,n)} \\
\Delta p_{(2)} &= \varphi_x{}^{(m,n)} - \varphi_x{}^{(m,n-1)} \\
\Delta p_{(3)} &= \varphi_y{}^{(m,n)} - \varphi_y{}^{(m,n-1)} \\
\Delta p_{(4)} &= \varphi_x{}^{(m,n+1)} - \varphi_x{}^{(m,n)} \\
\Delta p_{(5)} &= \frac{1}{2}\sqrt{2}\left(\varphi_x{}^{(m+1,n-1)} - \varphi_x{}^{(m,n)} - \varphi_y{}^{(m+1,n-1)} + \varphi_y{}^{(m,n)}\right) \\
\Delta p_{(6)} &= \frac{1}{2}\sqrt{2}\left(\varphi_x{}^{(m,n)} - \varphi_x{}^{(m-1,n-1)} + \varphi_y{}^{(m,n)} - \varphi_y{}^{(m-1,n-1)}\right) \\
\Delta p_{(7)} &= \frac{1}{2}\sqrt{2}\left(\varphi_x{}^{(m,n)} - \varphi_x{}^{(m-1,n+1)} - \varphi_y{}^{(m,n)} + \varphi_y{}^{(m-1,n+1)}\right) \\
\Delta p_{(8)} &= \frac{1}{2}\sqrt{2}\left(\varphi_x{}^{(m+1,n+1)} - \varphi_x{}^{(m,n)} + \varphi_y{}^{(m+1,n+1)} - \varphi_y{}^{(m,n)}\right)
\end{aligned} \tag{2.5}
$$

The kinetic energy of the inner particle, $E_{kin}{}^{(m,n)}$ is:

$$E_{kin}{}^{(m,n)} = \frac{1}{2}M\left(\dot{w}^{(m,n)}\right)^2 + \frac{1}{2}I\left(\dot{\varphi}_x{}^{(m,n)}\right)^2 + \frac{1}{2}I\left(\dot{\varphi}_y{}^{(m,n)}\right)^2 , \tag{2.6}$$

where M is the mass of the inner cell, $\dot{w}^{(m,n)}$ is the velocity of the inner cell in the out-of-plane direction, I is the mass moment of inertia of the inner cell, $\dot{\varphi}_x{}^{(m,n)}$ is the angular velocity of the inner cell around the y-axis and $\dot{\varphi}_y{}^{(m,n)}$ is the angular velocity of the inner cell around the x-axis. Substitution of the above-defined Lagrange function into the Euler-Lagrange equations gives the following equations of motion for the inner particle:

$$\begin{aligned} M\ddot{w}^{(m,n)} &= -\frac{1}{2}K_{s,axi}\begin{pmatrix} 8w^{(m,n)} - 2w^{(m+1,n)} - 2w^{(m,n-1)} - 2w^{(m-1,n)} - 2w^{(m,n+1)} \\ -d\varphi_x{}^{(m+1,n)} + d\varphi_x{}^{(m-1,n)} + d\varphi_y{}^{(m,n-1)} - d\varphi_y{}^{(m,n+1)} \end{pmatrix} \\ &-\frac{1}{2}K_{s,dia}\begin{pmatrix} 8w^{(m,n)} - 2w^{(m+1,n-1)} - 2w^{(m-1,n-1)} - 2w^{(m-1,n+1)} - 2w^{(m+1,n+1)} \\ -d\varphi_x{}^{(m+1,n-1)} + d\varphi_x{}^{(m-1,n-1)} + d\varphi_x{}^{(m-1,n+1)} - d\varphi_x{}^{(m+1,n+1)} \\ +d\varphi_y{}^{(m+1,n-1)} + d\varphi_y{}^{(m-1,n-1)} - d\varphi_y{}^{(m-1,n+1)} - d\varphi_y{}^{(m+1,n+1)} \end{pmatrix} \end{aligned} \tag{2.7}$$

$$\begin{aligned} I\ddot{\varphi}_x{}^{(m,n)} &= -\frac{1}{2}K_{s,axi}\left(dw^{(m+1,n)} - dw^{(m-1,n)} + d^2\varphi_x{}^{(m,n)} + \frac{1}{2}d^2\varphi_x{}^{(m+1,n)} + \frac{1}{2}d^2\varphi_x{}^{(m-1,n)} \right) \\ &-\frac{1}{2}G_{r,axi}\left(4\varphi_x{}^{(m,n)} - 2\varphi_x{}^{(m+1,n)} - 2\varphi_x{}^{(m-1,n)}\right) - \frac{1}{2}G_{t,axi}\left(4\varphi_x{}^{(m,n)} - 2\varphi_x{}^{(m,n-1)} - 2\varphi_x{}^{(m,n+1)}\right) \\ &-\frac{1}{2}K_{s,dia}\begin{pmatrix} dw^{(m+1,n-1)} - dw^{(m-1,n-1)} - dw^{(m-1,n+1)} + dw^{(m+1,n+1)} + 2d^2\varphi_x{}^{(m,n)} \\ +\frac{1}{2}d^2\varphi_x{}^{(m+1,n-1)} + \frac{1}{2}d^2\varphi_x{}^{(m-1,n-1)} + \frac{1}{2}d^2\varphi_x{}^{(m-1,n+1)} + \frac{1}{2}d^2\varphi_x{}^{(m+1,n+1)} \\ -\frac{1}{2}d^2\varphi_y{}^{(m+1,n-1)} + \frac{1}{2}d^2\varphi_y{}^{(m-1,n-1)} - \frac{1}{2}d^2\varphi_y{}^{(m-1,n+1)} + \frac{1}{2}d^2\varphi_y{}^{(m+1,n+1)} \end{pmatrix} \\ &-\frac{1}{2}G_{r,dia}\begin{pmatrix} 4\varphi_x{}^{(m,n)} - \varphi_x{}^{(m+1,n-1)} - \varphi_x{}^{(m-1,n-1)} - \varphi_x{}^{(m-1,n+1)} - \varphi_x{}^{(m+1,n+1)} \\ +\varphi_y{}^{(m+1,n-1)} - \varphi_y{}^{(m-1,n-1)} + \varphi_y{}^{(m-1,n+1)} - \varphi_y{}^{(m+1,n+1)} \end{pmatrix} \\ &-\frac{1}{2}G_{t,dia}\begin{pmatrix} 4\varphi_x{}^{(m,n)} - \varphi_x{}^{(m+1,n-1)} - \varphi_x{}^{(m-1,n-1)} - \varphi_x{}^{(m-1,n+1)} - \varphi_x{}^{(m+1,n+1)} \\ +\varphi_y{}^{(m+1,n-1)} - \varphi_y{}^{(m-1,n-1)} + \varphi_y{}^{(m-1,n+1)} - \varphi_y{}^{(m+1,n+1)} \end{pmatrix} \end{aligned} \tag{2.8}$$

$$I\ddot{\varphi}_y^{(m,n)} = -\frac{1}{2}K_{s,axi}\left(dw^{(m,n+1)} - dw^{(m,n-1)} + d^2\varphi_y^{(m,n)} + \frac{1}{2}d^2\varphi_y^{(m,n-1)} + \frac{1}{2}d^2\varphi_y^{(m,n+1)} \right)$$
$$-\frac{1}{2}G_{r,axi}\left(4\varphi_y^{(m,n)} - 2\varphi_y^{(m,n-1)} - 2\varphi_y^{(m,n+1)}\right) - \frac{1}{2}G_{t,axi}\left(4\varphi_y^{(m,n)} - 2\varphi_y^{(m+1,n)} - 2\varphi_y^{(m-1,n)}\right)$$
$$-\frac{1}{2}K_{s,dia}\begin{pmatrix} -dw^{(m+1,n-1)} - dw^{(m-1,n-1)} + dw^{(m-1,n+1)} + dw^{(m+1,n+1)} + 2d^2\varphi_y^{(m,n)} \\ -\frac{1}{2}d^2\varphi_x^{(m+1,n-1)} + \frac{1}{2}d^2\varphi_x^{(m-1,n-1)} - \frac{1}{2}d^2\varphi_x^{(m-1,n+1)} + \frac{1}{2}d^2\varphi_x^{(m+1,n+1)} \\ +\frac{1}{2}d^2\varphi_y^{(m+1,n-1)} + \frac{1}{2}d^2\varphi_y^{(m-1,n-1)} + \frac{1}{2}d^2\varphi_y^{(m-1,n+1)} + \frac{1}{2}d^2\varphi_y^{(m+1,n+1)} \end{pmatrix} \tag{2.9}$$
$$-\frac{1}{2}G_{r,dia}\begin{pmatrix} 4\varphi_y^{(m,n)} + \varphi_x^{(m+1,n-1)} - \varphi_x^{(m-1,n-1)} + \varphi_x^{(m-1,n+1)} - \varphi_x^{(m+1,n+1)} \\ -\varphi_y^{(m+1,n-1)} - \varphi_y^{(m-1,n-1)} - \varphi_y^{(m-1,n+1)} - \varphi_y^{(m+1,n+1)} \end{pmatrix}$$
$$-\frac{1}{2}G_{t,dia}\begin{pmatrix} 4\varphi_y^{(m,n)} + \varphi_x^{(m+1,n-1)} - \varphi_x^{(m-1,n-1)} + \varphi_x^{(m-1,n+1)} - \varphi_x^{(m+1,n+1)} \\ -\varphi_y^{(m+1,n-1)} - \varphi_y^{(m-1,n-1)} - \varphi_y^{(m-1,n+1)} - \varphi_y^{(m+1,n+1)} \end{pmatrix}$$

In the equations above, $\ddot{w}^{(m,n)}$ is the acceleration of particle (m,n) in the out-of-plane direction, whereas $\ddot{\varphi}_x^{(m,n)}$ and $\ddot{\varphi}_y^{(m,n)}$ are the angular accelerations of the particle about the y-axis and x-axis, respectively.

2.2.2 Equations of motion for a boundary particle

Deriving the equations of motion for the boundary (excluding the corner) particles is done in a similar manner as deriving the equations of motion for the inner particles. At the top boundary $(n=1)$, for example, particle $(m,1)$ is connected via springs 1, 3, 4, 7 and 8 as shown in Figure 2-5. The stiffness of the springs on the boundaries is half of the stiffness of inner connections. Accordingly, the potential energy for the boundary particle $(m,1)$ is given as:

$$E_{pot}^{(m,1)} = \frac{1}{4}\left(\Delta s_{(1)}^{\;2}K_{s,axi} + \Delta r_{(1)}^{\;2}G_{r,axi} + \Delta p_{(1)}^{\;2}G_{t,axi}\right)$$
$$+\frac{1}{4}\left(\Delta s_{(3)}^{\;2}K_{s,axi} + \Delta r_{(3)}^{\;2}G_{r,axi} + \Delta p_{(3)}^{\;2}G_{t,axi}\right) + \frac{1}{2}\left(\Delta s_{(4)}^{\;2}K_{s,axi} + \Delta r_{(4)}^{\;2}G_{r,axi} + \Delta p_{(4)}^{\;2}G_{t,axi}\right) \tag{2.10}$$
$$+\frac{1}{2}\sum_{i=7}^{8}\left(\Delta s_{(i)}^{\;2}K_{s,dia} + \Delta r_{(i)}^{\;2}G_{r,dia} + \Delta p_{(i)}^{\;2}G_{t,dia}\right)$$

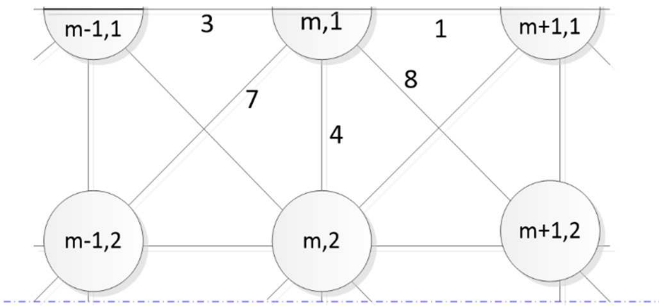

Figure 2-5: Connections of a top boundary particle

The mass M and mass moment of inertia I of the boundary particle are half the mass and mass moment of inertia of the inner particle. Accordingly, the kinetic energy of the boundary particle at the top edge of the plate, ${E_{kin}}^{(m,1)}$ reads:

$$ {E_{kin}}^{(m,1)} = \frac{1}{4} M \left(\dot{w}^{(m,1)} \right)^2 + \frac{1}{4} I \left({\dot{\varphi}_x}^{(m,1)} \right)^2 + \frac{1}{4} I \left({\dot{\varphi}_y}^{(m,1)} \right)^2 \tag{2.11} $$

Application of the Euler-Lagrange equations gives the equations of motion for the boundary particle $(m,1)$. Equations of motion for the particles on the other edges of the plate are derived in the same manner.

2.2.3 Equations of motion for a corner particle

The derivation of the equations of motion for the corner particles is again done in a similar manner. At the top left corner, for example, particle $(1,1)$ is connected via springs 1, 4 and 8 as shown in Figure 2-6. The stiffness of the springs on the boundaries is half of the stiffness of the corresponding inner connections. The potential energy for the corner particle $(1,1)$ is, therefore, given as:

$$ \begin{aligned} {E_{pot}}^{(1,1)} &= \frac{1}{4} \left(\Delta {s_{(1)}}^2 K_{s,axi} + \Delta {r_{(1)}}^2 G_{r,axi} + \Delta {p_{(1)}}^2 G_{t,axi} \right) \\ &+ \frac{1}{4} \left(\Delta {s_{(4)}}^2 K_{s,axi} + \Delta {r_{(4)}}^2 G_{r,axi} + \Delta {p_{(4)}}^2 G_{t,axi} \right) + \frac{1}{2} \left(\Delta {s_{(8)}}^2 K_{s,dia} + \Delta {r_{(8)}}^2 G_{r,dia} + \Delta {p_{(8)}}^2 G_{t,dia} \right) \end{aligned} \tag{2.12} $$

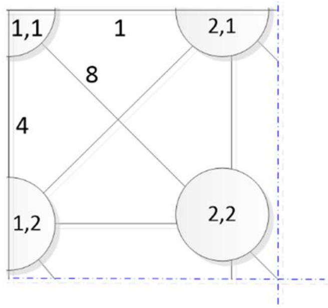

Figure 2-6: Connections of the top left corner particle

The mass M and mass moment of inertia I of the corner particle are a quarter of the mass and mass moment of inertia of the inner particle. The kinetic energy of the top left corner particle, ${E_{kin}}^{(1,1)}$, is:

$${E_{kin}}^{(1,1)} = \frac{1}{8}M\left(\dot{w}^{(1,1)}\right)^2 + \frac{1}{8}I\left({\dot{\varphi}_x}^{(1,1)}\right)^2 + \frac{1}{8}I\left({\dot{\varphi}_y}^{(1,1)}\right)^2 \tag{2.13}$$

Applying Euler-Lagrange equations one obtains the equations of motion for the corner particle. Equations of motion for the other corner particles are derived in the same manner.

2.3 Lattice parameters as functions of those of corresponding continuum plate

The lattice model has to be consistent with a corresponding continuum plate model in the long-wave limit, in which the scale of deformations, i.e. the wavelength corresponding to the process that is simulated, is much larger than the dimension of the lattice cell. In this section, relations are derived between parameters of the lattice and those of the Mindlin-Reissner plate, which assure this consistency.

2.3.1 Spring stiffness of the connections

To make the lattice model consistent with the isotropic Mindlin-Reissner plate in the long-wave limit, the lattice is continualized assuming the following Taylor series based relations between the generalized displacements of the nodes of the lattice:

$$\begin{aligned}&\left[w^{(m+p,n+q)}(t)\quad \varphi_x^{(m+p,n+q)}(t)\quad \varphi_y^{(m+p,n+q)}(t)\right]^T \approx \Bigg\{\left[\tilde{w}(x,y,t)\quad \tilde{\varphi}_x(x,y,t)\quad \tilde{\varphi}_x(x,y,t)\right]^T \\ &+pad\left[\frac{\partial \tilde{w}}{\partial x}\quad \frac{\partial \tilde{\phi}_x}{\partial x}\quad \frac{\partial \tilde{\phi}_y}{\partial x}\right]^T + qd\left[\frac{\partial \tilde{w}}{\partial y}\quad \frac{\partial \tilde{\phi}_x}{\partial y}\quad \frac{\partial \tilde{\phi}_y}{\partial y}\right]^T + \frac{1}{2}p^2d^2\left[\frac{\partial^2 \tilde{w}}{\partial x^2}\quad \frac{\partial^2 \tilde{\phi}_x}{\partial x^2}\quad \frac{\partial^2 \tilde{\phi}_y}{\partial x^2}\right]^T \\ &+\frac{1}{2}pqd^2\left[\frac{\partial^2 \tilde{w}}{\partial x\partial y}\quad \frac{\partial^2 \tilde{\phi}_x}{\partial x\partial y}\quad \frac{\partial^2 \tilde{\phi}_y}{\partial x\partial y}\right]^T + \frac{1}{2}q^2d^2\left[\frac{\partial^2 \tilde{w}}{\partial y^2}\quad \frac{\partial^2 \tilde{\phi}_x}{\partial y^2}\quad \frac{\partial^2 \tilde{\phi}_y}{\partial y^2}\right]^T\Bigg\}_{x=(m-1)d,\, y=(n-1)d}\end{aligned} \tag{2.14}$$

Substituting (2.14) into (2.7) to (2.9) and disregarding terms of the order higher than d^2 one obtains the continualized equations of motion of the lattice which are valid in the long wave limit:

$$M\ddot{\tilde{w}} = d^2\left(K_{s,axi} + 2K_{s,dia}\right)\left(\frac{\partial^2 \tilde{w}}{\partial x^2} + \frac{\partial^2 \tilde{w}}{\partial y^2} + \frac{\partial \tilde{\varphi}_x}{\partial x} + \frac{\partial \tilde{\varphi}_y}{\partial y}\right) \tag{2.15}$$

$$\begin{aligned}I\ddot{\tilde{\varphi}}_x &= d^2\left(G_{r,axi} + G_{r,dia} + G_{t,dia}\right)\frac{\partial^2 \tilde{\varphi}_x}{\partial x^2} + d^2\left(G_{r,dia} + G_{t,dia} + G_{t,axi}\right)\frac{\partial^2 \tilde{\varphi}_x}{\partial y^2} \\ &+2d^2\left(G_{r,dia} + G_{t,dia}\right)\frac{\partial^2 \tilde{\varphi}_y}{\partial x\partial y} - \left(K_{s,axi} + 2K_{s,dia}\right)\left(d^2\frac{\partial \tilde{w}}{\partial x} + d^2\tilde{\varphi}_x\right)\end{aligned} \tag{2.16}$$

$$\begin{aligned}I\ddot{\tilde{\varphi}}_y &= d^2\left(G_{r,axi} + G_{r,dia} + G_{t,dia}\right)\frac{\partial^2 \tilde{\varphi}_y}{\partial y^2} + d^2\left(G_{r,dia} + G_{t,dia} + G_{t,axi}\right)\frac{\partial^2 \tilde{\varphi}_y}{\partial x^2} \\ &+2d^2\left(G_{r,dia} + G_{t,dia}\right)\frac{\partial^2 \tilde{\varphi}_x}{\partial x\partial y} - \left(K_{s,axi} + 2K_{s,dia}\right)\left(d^2\frac{\partial \tilde{w}}{\partial y} + d^2\tilde{\varphi}_y\right)\end{aligned} \tag{2.17}$$

The spring stiffness of the connections $K_{s,axi}$, $G_{r,axi}$, $G_{t,axi}$, $K_{s,dia}$, $G_{r,dia}$ and $G_{t,dia}$ and the inertia coefficients M and I are determined by relating (2.15) - (2.17) to the equations of motion of the Mindlin-Reissner theory for continuum plates, given, for example, by Rao (2007):

$$\rho h \ddot{w} = k^2 G h \left(\frac{\partial^2 w}{\partial x^2} + \frac{\partial^2 w}{\partial y^2} + \frac{\partial \varphi_x}{\partial x} + \frac{\partial \varphi_y}{\partial y} \right) \tag{2.18}$$

$$\frac{\rho h^3}{12} \ddot{\varphi}_x = \frac{D}{2} \left[(1-\nu) \left(\frac{\partial^2 \varphi_x}{\partial x^2} + \frac{\partial^2 \varphi_x}{\partial y^2} \right) + (1+\nu) \left(\frac{\partial^2 \varphi_x}{\partial x^2} + \frac{\partial^2 \varphi_y}{\partial x \partial y} \right) \right] - k^2 G h \left(\varphi_x + \frac{\partial w}{\partial x} \right) \tag{2.19}$$

$$\frac{\rho h^3}{12} \ddot{\varphi}_y = \frac{D}{2} \left[(1-\nu) \left(\frac{\partial^2 \varphi_y}{\partial y^2} + \frac{\partial^2 \varphi_y}{\partial x^2} \right) + (1+\nu) \left(\frac{\partial^2 \varphi_y}{\partial y^2} + \frac{\partial^2 \varphi_x}{\partial x \partial y} \right) \right] - k^2 G h \left(\varphi_y + \frac{\partial w}{\partial y} \right), \tag{2.20}$$

where ρ is the mass density of the plate, h is the thickness, $D = Eh^3 / 12(1-\nu^2)$ is the plate bending stiffness, E is Young's modulus, ν is Poisson's ratio, $k^2 = 5/(6-\nu)$ is the shear correction factor of a rectangular cross-section and $G = E/(2(1+\nu))$ is the shear modulus.

Equations (2.15) - (2.17) and (2.18) - (2.20) are in agreement when the following properties are assigned to the parameters in the lattice model:

$$M = \rho h d^2 \tag{2.21}$$

$$I = \frac{1}{12} \rho h^3 d^2 \tag{2.22}$$

$$K_{s,axi} + 2K_{s,dia} = k^2 G h \tag{2.23}$$

$$G_{r,axi} = \frac{D}{4}(3-\nu) \tag{2.24}$$

$$G_{t,axi} = \frac{D}{4}(1-3\nu) \tag{2.25}$$

$$G_{r,dia} + G_{t,dia} = \frac{D}{4}(1+\nu) \tag{2.26}$$

2.3.2 Kelvin foundation

The prior analysis was carried out under assumption that the plate is unsupported. In many engineering applications including sea-ice, which is considered in this thesis, the plate is supported by a fluid or solid medium. A simplistic way to account for this is by means of the visco-elastic Kelvin foundation. This foundation is included in the model (see Figure 2-7) by adding a term $-k_{Kelvin}w^{(m,n)} - c_{Kelvin}\dot{w}^{(m,n)}$ to the right hand side of equation (2.7) for out-of-plane deflection inertia. In the case of floating sea ice $k_{Kelvin} = \rho_w g d^2$ is the foundation stiffness, where ρ_w is the water density and g is the gravitational acceleration. c_{Kelvin} is the damping coefficient, representing effective hydrodynamic dissipation by geometrical radiation.

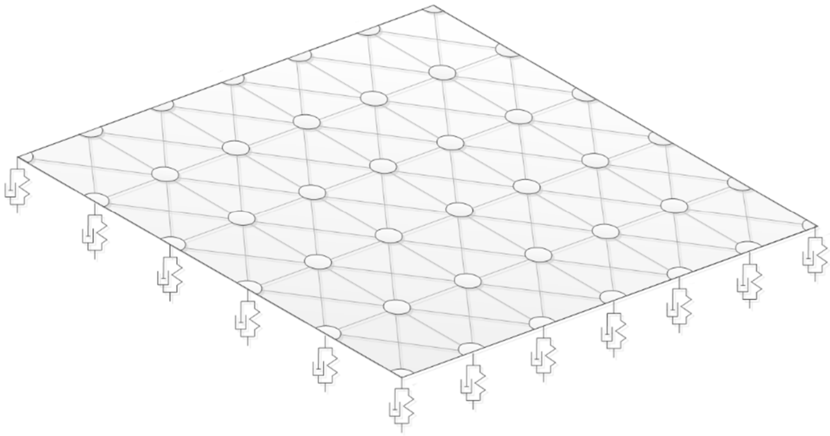

Figure 2-7: A Kelvin foundation is included in the lattice model, representing buoyancy and hydrodynamic dissipation under a sheet of sea-ice

2.3.3 Material damping

Part of the energy of a material in motion will be converted to heat and dampen the material response. To account for this effect, damping proportional to the bending, shear and torsion rates of the plate are included in equations (2.18) - (2.20), giving:

$$\rho h\ddot{w} = k^2 Gh\left(1+\alpha\frac{\partial}{\partial t}\right)\left(\frac{\partial^2 w}{\partial x^2}+\frac{\partial^2 w}{\partial y^2}+\frac{\partial \varphi_x}{\partial x}+\frac{\partial \varphi_y}{\partial y}\right) \tag{2.27}$$

$$\begin{aligned}\frac{\rho h^3}{12}\ddot{\varphi}_x &= \frac{D}{2}\left(1+\alpha\frac{\partial}{\partial t}\right)\left[(1-\nu)\left(\frac{\partial^2 \varphi_x}{\partial x^2}+\frac{\partial^2 \varphi_x}{\partial y^2}\right)+(1+\nu)\left(\frac{\partial^2 \varphi_x}{\partial x^2}+\frac{\partial^2 \varphi_y}{\partial x \partial y}\right)\right]\\ &-k^2 Gh\left(1+\alpha\frac{\partial}{\partial t}\right)\left(\varphi_x+\frac{\partial w}{\partial x}\right)\end{aligned} \tag{2.28}$$

$$\begin{aligned}\frac{\rho h^3}{12}\ddot{\varphi}_y &= \frac{D}{2}\left(1+\alpha\frac{\partial}{\partial t}\right)\left[(1-\nu)\left(\frac{\partial^2 \varphi_y}{\partial y^2}+\frac{\partial^2 \varphi_y}{\partial x^2}\right)+(1+\nu)\left(\frac{\partial^2 \varphi_y}{\partial y^2}+\frac{\partial^2 \varphi_x}{\partial x \partial y}\right)\right]\\ &-k^2 Gh\left(1+\alpha\frac{\partial}{\partial t}\right)\left(\varphi_y+\frac{\partial w}{\partial y}\right)\end{aligned} \tag{2.29}$$

Where α is the damping coefficient. In the lattice model, the same effect is captured by including dampers in parallel with the springs. The new connections are depicted in Figure 2-8.

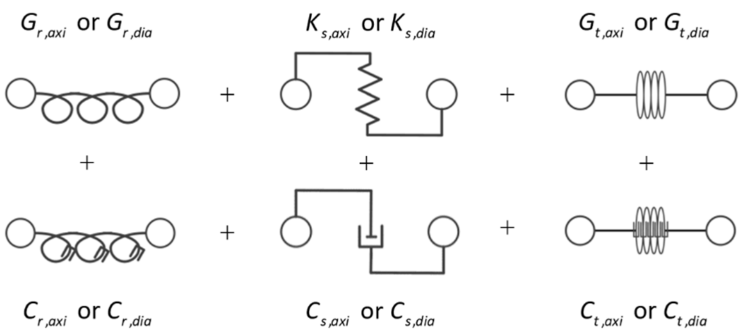

Figure 2-8: Damping is included in the axial and diagonal connections between the nodes in the lattice model, now consisting of springs and dashpots in bending, shear and torsional direction (A-A' and B-B' in Figure 2-3)

The dashpot coefficients are set proportional to the spring stiffness by damping coefficient α :

$$C_{s,axi} + 2C_{s,dia} = \alpha\left(K_{s,axi} + 2K_{s,dia}\right) \tag{2.30}$$

$$C_{r,axi} = \alpha G_{r,axi} \tag{2.31}$$

$$C_{t,axi} = \alpha G_{t,axi} \tag{2.32}$$

$$C_{r,dia} + C_{t,dia} = \alpha\left(G_{r,dia} + G_{t,dia}\right) \tag{2.33}$$

$C_{s,axi}$, $C_{r,axi}$ and $C_{t,axi}$ are the coefficients of the axial shear, rotational and torsional dampers, respectively. $C_{s,dia}$, $C_{r,dia}$ and $C_{t,dia}$ are the coefficients of the diagonal shear, rotational and torsion dampers respectively.

2.4 Wave dynamics and vibrations of the lattice

In this section, the wave propagation in the lattice is analysed. The wave propagation characteristics are compared to those of the corresponding isotropic continuum plate model. This analysis allows to distinguish the underlying reasons for the differences in the responses at higher frequencies and attribute those to the dispersion and anisotropy in the lattice model. Analogously, the analysis of wave dispersion characteristics of a lattice-spring model in comparison with classic elastic continuum theory were carried out previously in 1D (Askar, 1985) and 2D (Suiker et al., 2001a). Wave dispersion characteristics and anisotropy were studied for a lattice-spring model in comparison with a Cosserat continuum in Suiker et al. (2001c).

The dispersion of plane harmonic waves in the lattice is compared to the wave dispersion in the Mindlin-Reissner plate. The displacements of the lattice nodes w, φ_x and φ_y in a plane wave can be described as:

$$w^{(m,n)}\left(t\right) = \mathrm{W}\mathrm{e}^{\mathrm{i}(\omega t - k_x ma - k_y na)} \tag{2.34}$$

$$\varphi_x^{(m,n)}\left(t\right) = \Phi_x\,\mathrm{e}^{\mathrm{i}(\omega t - k_x ma - k_y na)} \tag{2.35}$$

$$\varphi_y^{(m,n)}\left(t\right) = \Phi_y\,\mathrm{e}^{\mathrm{i}(\omega t - k_x ma - k_y na)}, \tag{2.36}$$

where W , Φ_x and Φ_y are the complex wave amplitudes, ω is the angular frequency and k_x and k_y are the wave numbers in x- and y-direction, respectively. Substituting (2.34)-(2.36) in the equations of motion of the lattice model (2.7)-(2.9) one obtains the following system of three algebraic equations:

$$\begin{aligned}
&\Big[-2\big(\cos(K_x)+\cos(K_y)\big)\\
&+2\frac{K_{s,dia}}{K_{s,axi}}\big(2-\cos(K_x-K_y)-\cos(K_x+K_y)\big)-\Omega^2+\frac{k_s}{K_{s,axi}}+4\Big]W\\
&+\left[i\left(\frac{K_{s,dia}}{K_{s,axi}}\big(\sin(K_x-K_y)+\sin(K_x+K_y)\big)+\sin(K_x)\right)\right]\Phi_x\\
&+\left[i\left(\frac{K_{s,dia}}{K_{s,axi}}\big(-\sin(K_x-K_y)+\sin(K_x+K_y)\big)+\sin(K_y)\right)\right]\Phi_y=0
\end{aligned} \tag{2.37}$$

$$\begin{aligned}
&\left[-i\left(\frac{K_{s,dia}}{K_{s,axi}}\big(\sin(K_x-K_y)+\sin(K_x+K_y)\big)+\sin(K_x)\right)\right]W\\
&+\Bigg[2\frac{G_{r,axi}}{a^2K_{s,axi}}\big(1-\cos(K_x)\big)+\left(\frac{G_{r,dia}+G_{t,dia}}{a^2K_{s,axi}}\right)\big(2-\cos(K_x-K_y)-\cos(K_x+K_y)\big)\\
&+2\frac{G_{t,axi}}{a^2K_{s,axi}}\big(1-\cos(K_y)\big)+\frac{1}{2}\frac{K_{s,dia}}{K_{s,axi}}\big(2+\cos(K_x-K_y)+\cos(K_x+K_y)\big)\\
&+\frac{1}{2}\big(1+\cos(K_x)\big)-\frac{I}{Ma^2}\Omega^2\Bigg]\Phi_x+\Bigg[\left(\frac{G_{r,dia}+G_{t,dia}}{a^2K_{s,axi}}\right)\big(\cos(K_x-K_y)-\cos(K_x+K_y)\big)\\
&+\frac{1}{2}\frac{K_{s,dia}}{K_{s,axi}}\big(-\cos(K_x-K_y)+\cos(K_x+K_y)\big)\Bigg]\Phi_y=0
\end{aligned} \tag{2.38}$$

$$\begin{aligned}
&\left[-i\left(\frac{K_{s,dia}}{K_{s,axi}}\left(\sin\left(K_x-K_y\right)-\sin\left(K_x+K_y\right)\right)+\sin\left(K_y\right)\right)\right]W\\
&+\left[\left(\frac{G_{\mathrm{r},dia}+G_{t,dia}}{aK_{s,axi}}\right)\left(\cos\left(K_x-K_y\right)-\cos\left(K_x+K_y\right)\right)\right.\\
&\left.+\frac{1}{2}\frac{K_{s,dia}}{K_{s,axi}}\left(-\cos\left(K_x-K_y\right)+\cos\left(K_x+K_y\right)\right)\right]\Phi_x\\
&+\left[2\frac{G_{\mathrm{r},axi}}{aK_{s,axi}}\left(1-\cos\left(K_y\right)\right)+\left(\frac{G_{\mathrm{r},dia}+G_{t,dia}}{aK_{s,axi}}\right)\right.\\
&\left(2-\cos\left(K_x-K_y\right)-\cos\left(K_x+K_y\right)\right)+2\frac{G_{\mathrm{t},axi}}{aK_{s,axi}}\left(1-\cos\left(K_x\right)\right)\\
&\left.+\frac{1}{2}\frac{K_{s,dia}}{K_{s,axi}}\left(2+\cos\left(K_x-K_y\right)+\cos\left(K_x+K_y\right)\right)+\frac{1}{2}\left(1+\cos\left(K_y\right)\right)-\frac{I}{Ma^2}\Omega^2\right]\Phi_y=0,
\end{aligned} \tag{2.39}$$

where $\Omega=\omega\sqrt{M/K_{s,axi}}$ is a dimensionless angular frequency and $K_x=k_xd$ and $K_y=k_yd$ are dimensionless wavenumbers in x-and y-direction, respectively.

For the continuum model, the plane waves in the plate are described as:

$$w(x,y,t)=\mathrm{W}\mathrm{e}^{\mathrm{i}(\omega t-k_xx-k_yy)} \tag{2.40}$$

$$\varphi_x(x,y,t)=\Phi_x\,\mathrm{e}^{\mathrm{i}(\omega t-k_xx-k_yy)} \tag{2.41}$$

$$\varphi_y(x,y,t)=\Phi_y\,\mathrm{e}^{\mathrm{i}(\omega t-k_xx-k_yy)}, \tag{2.42}$$

where W, Φ_x and Φ_y are the complex wave amplitudes, ω is the angular frequency, k_x and k_y are the wave numbers in x- and y-direction respectively.

Substituting (2.40)-(2.42) into the equations of motion for the continuous plate (2.18)-(2.20) gives a system of three algebraic equations:

$$\left[G_b(k_x{}^2+k_y{}^2)-\omega^2+\omega_0{}^2\right]W+\left[iG_bk_x\right]\Phi_x+\left[iG_bk_y\right]\Phi_y=0 \tag{2.43}$$

$$\begin{aligned}&\left[-12iG_bk_x\right]W+\left[D_bh^2(2k_x{}^2+k_y{}^2(1-\nu))-\omega^2h^2+12G_b\right]\Phi_x\\&\qquad+\left[D_bh^2k_xk_y(1+\nu)\right]\Phi_y=0\end{aligned} \tag{2.44}$$

$$\begin{aligned}&\left[-12iG_bk_y\right]W+\left[D_bh^2k_xk_y(1+\nu)\right]\Phi_x\\&\qquad+\left[D_bh^2(k_x{}^2(1-\nu)+2k_y{}^2)-\omega^2h^2+12G_b\right]\Phi_y=0,\end{aligned} \tag{2.45}$$

where $G_b = k^2 G / \rho$, $D_b = 6D / (\rho \mathrm{h}^3)$ and $\omega_0 = \sqrt{k_s / (\rho \mathrm{h})}$.

The two systems of equations (2.37) - (2.39) and (2.43) - (2.45) have non-trivial solutions if and only if the determinants $\Delta(\Omega, \mathrm{K_x}, \mathrm{K_y})$ for (2.37) - (2.39) and $\Delta(\omega, \mathrm{k_x}, \mathrm{k_y})$ for (2.43)-(2.45) are equal to zero, giving the dispersion relations of the lattice and continuum system respectively.

For computation of the dispersion curves that are presented in Figure 2-9, input parameters in Table 2-1 are used, representing a floating ice plate with thickness of 1.5m. Dispersion curves are plotted for various magnitudes of the interparticle distance, both larger than, equal to and smaller than the plate thickness.

The graphs in Figure 2-9 show dependencies of the wave frequency of the bending and rotational waves on the normalized wave number $k_x d$ under the assumption that $k_y = 0$. Each graph in Figure 2-9 contains six curves. The continuous lines correspond to the continuum model, whereas the dashed ones correspond to the lattice model. The lines marked with triangles represent the waves which primarily involve the out-of-plane deflection of the plate (note that all waves in each model are coupled, hence these are defined with reference to the primary motion at low wavenumbers). These waves are referred to as deflection waves. The lines marked with diamonds are related to the waves in which the primary motion is rotational and parallel to the propagation direction of the wave (hereafter referred to as longitudinal rotational waves). Finally, the lines marked with circles are related to the waves in which the primary motion is rotational and perpendicular to the propagation direction of the wave (hereafter referred to as transversal rotational waves).

As expected for long waves, $k_x d << 1$, the dispersion curves of the waves in the lattice match very closely with those of the continuum plate. The shorter the waves (the higher the wave number) the worse the correspondence. These results are fully in line with the expectations. Yet these results are of importance for the developed model as they show (i) that the lattice model matches the continuum one in the long-wave limit and (ii) for every lattice cell size there is a specific value of the frequency/wavenumber starting from which the lattice response to a load will be different from that of the continuum plate due to the difference in the dispersion characteristics.

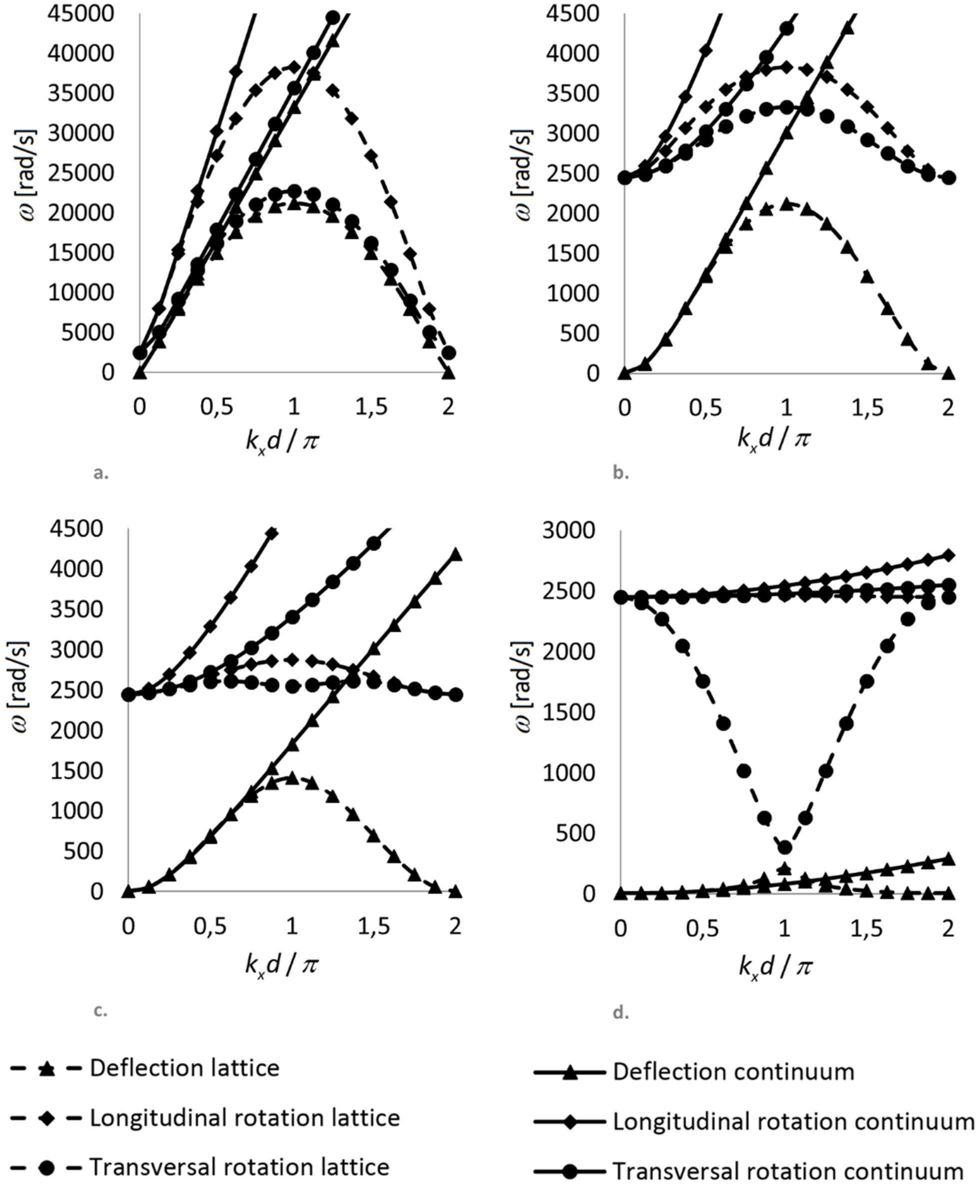

Figure 2-9: Dispersion curves for the Mindlin-Reissner continuum and the lattice model. a) Cell size 0.1mx0.1m. b) Cell size 1mx1m. c) Cell size 1.5mx1.5m (cell size equals plate thickness). d) Cell size 10mx10m

Table 2-1: Input parameters of an ice plate, used for comparison of the lattice model with the continuum Mindlin-Reissner plate

Parameter	Symbol	Quantity	Unit
Poisson's ratio	ν	0.3	-
Plate density	ρ	900	kg/m3
Load	F	10	kN
Young's modulus	E	3.E+9	N/m2
Plate thickness	h	1.5	m
Water density	ρ_w	1025	kg/m3

In addition to the differences in wave dispersion, the lattice is also anisotropic in contrast to the isotropic continuum plate model at hand. To discover the frequencies at which the anisotropy plays a role, contours of constant frequency are plotted in Figure 2-10 and in Figure 2-11 in the $k_x d - k_y d$ plane in accordance with the dispersion equations. An interparticle distance of 1m is used to produce the contours. For angular frequencies up to 2000 rad/s only the deflection wave (the wave in which the particles deflect out-of-plane and little rotation of the particles takes place) is present. Figure 2-10 shows that up to approximately 500 rad/s the deflection waves are nearly isotropic which corresponds to almost circular contours in the plot.

For lower-frequency deflections of 500 rad/s there is good agreement between the dispersion curves for the models. For higher frequencies deviation can be observed and the effects originating from the anisotropy of the lattice become visible as the curves start losing their circular shape. As can be seen in Figure 2-10, the curves remain quasi-circular up to 2000 rad/s. At higher frequencies, as Figure 2-11 shows for 3000 rad/s, the wave propagation in the lattice becomes significantly anisotropic. One can also see that the number of curves per frequency in Figure 2-11 is tripled with respect to the number of those in Figure 2-10. This is because the frequencies represented in Figure 2-11 are above the cut-off frequency of the rotational waves. At 3000 rad/s the deflection wave in the continuum model and that in the lattice model are significantly different.

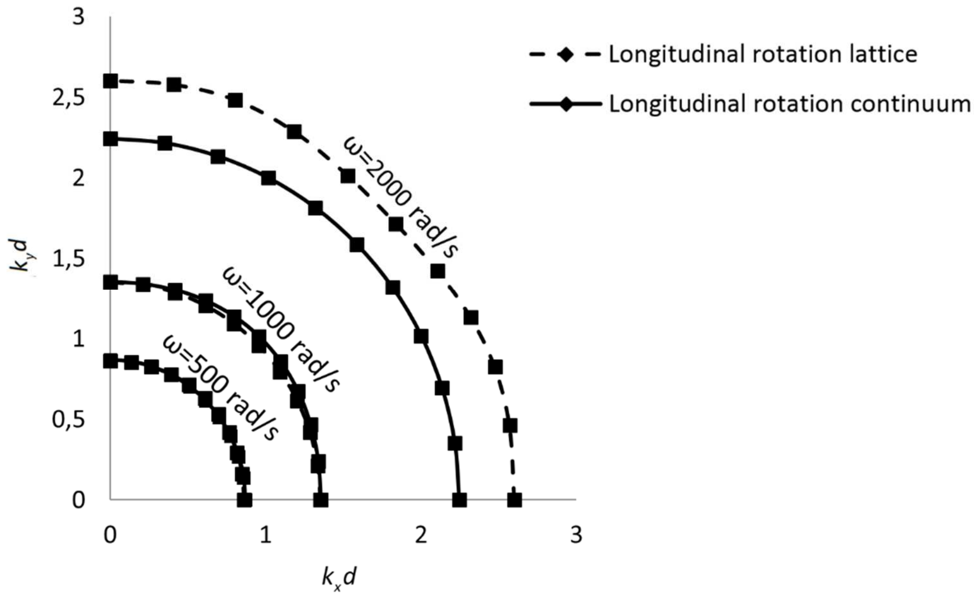

Figure 2-10: Directional characteristics of deflection and rotational waves propagating through the Mindlin-Reissner continuum (solid lines) and the lattice of cell size a=1m (dashed lines) for various wave frequencies

Thus, the anisotropy of the lattice contributes to the reduced agreement between the lattice model and the Mindlin-Reissner continuum for higher angular frequencies. The larger the interparticle distance, the lower the frequency at which the anisotropy starts to play a role. The effects of the anisotropy simulated in the range of higher vibration frequencies are not realistic for ice, since the structure of the ice, which does not have a clear internal length scale, is not modelled with the lattice.

According to Figure 2-9, the angular frequency of the waves in the continuum plate model tends to infinity as the wavenumber increases. The lattice model allows for wave propagation only up to a certain frequency, depending on the cell size of the lattice. The maximum frequency in the lattice is achieved at a normalised wave number $kd = \pi$. The slope of the dispersion curve, which represents the group velocity, is zero at this this wavenumber, resulting in a standing wave in the lattice. Wavelengths smaller than two times the cell size cannot be described with the lattice model.

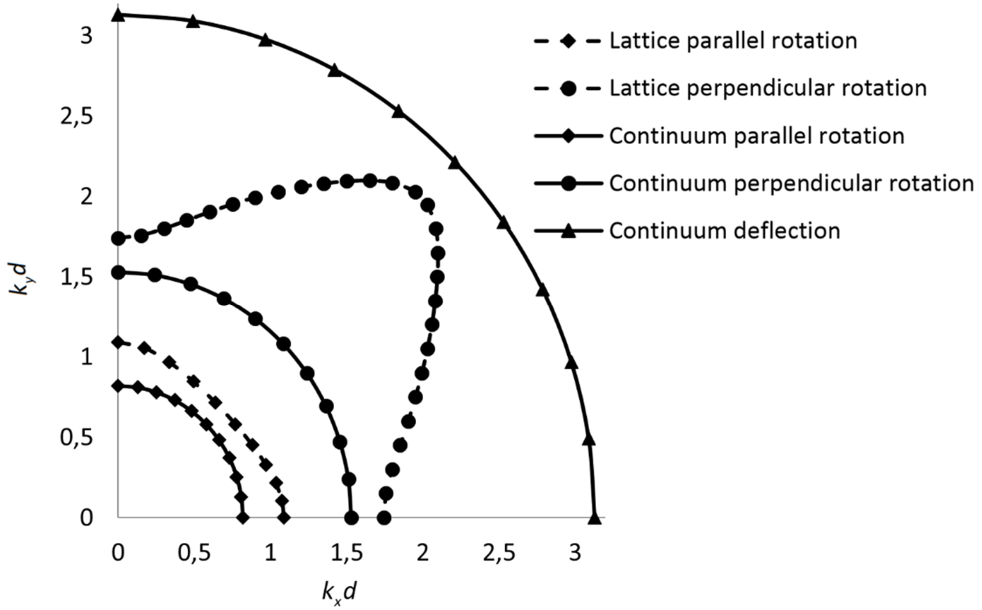

Figure 2-11: Directional characteristics of deflection and rotational waves propagating through the Mindlin-Reissner continuum (solid lines) and the lattice of cell size a=1m (dashed lines) for a wave frequency of 3000 rad/s. Longitudinal rotational waves are marked with diamonds and transversal rotational waves are marked with circles

2.5 Verification against analytical solution of a rectangular plate under sinusoidal load

To verify the predictive capabilities of the lattice model, the steady-state plate response to a harmonic out-of-plane point load is investigated. The response of the continuum model is found analytically, whereas the lattice response is found by means of solving numerically the governing equations in the frequency domain. A rectangular plate on Kelvin foundation, simply supported at the edges is used for this verification study as shown in Figure 2-12, Figure 2-13 and Figure 2-14. The eigenfrequencies, deflection and rotations are analysed. The effect of the number of particles in the lattice model as well as the effect of the hydrodynamic (modelled as viscous damping on the Kelvin foundation) and material damping coefficients are studied.

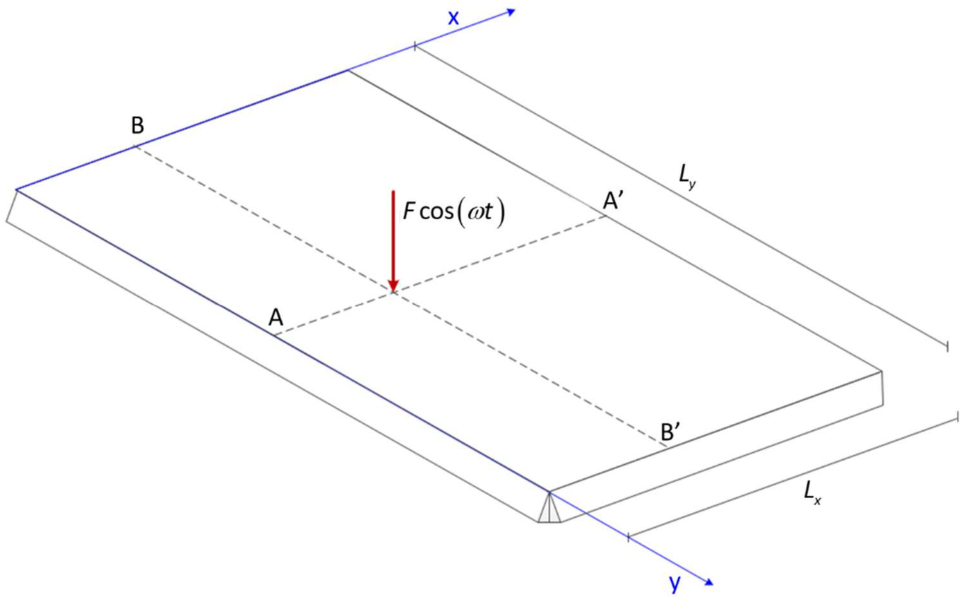

Figure 2-12: Rectangular plate supported by a Kelvin foundation, simply supported at the edges and loaded by a sinusoidal point load in out-of-plane direction

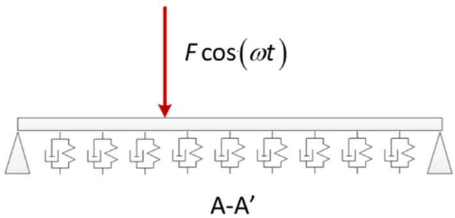

Figure 2-13: Cross section A-A'

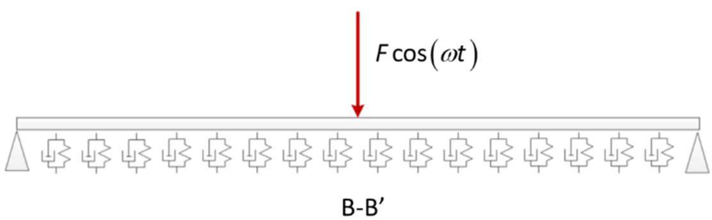

Figure 2-14: Cross section B-B'

2.5.1 Analytical solution

Equations (2.18) - (2.20) are the governing analytical equations of free vibrations of a thick plate according to Reissner-Mindlin theory. Buoyancy effects, external load and material damping are added to the equations of motion, resulting in:

$$\begin{aligned}\rho h\ddot{w} + c_s\dot{w} + k_s w = k^2 Gh\left(1+\alpha\frac{\partial}{\partial t}\right)\left(\frac{\partial^2 w}{\partial x^2}+\frac{\partial^2 w}{\partial y^2}+\frac{\partial \varphi_x}{\partial x}+\frac{\partial \varphi_y}{\partial y}\right)\\ +F\cos(\omega \mathrm{t})\delta(x-x_0)\delta(y-y_0)\end{aligned} \tag{2.46}$$

$$\begin{aligned}\frac{\rho h^3}{12}\ddot{\varphi}_x = \frac{D}{2}\left(1+\alpha\frac{\partial}{\partial t}\right)\left[(1-\nu)\left(\frac{\partial^2 \varphi_x}{\partial x^2}+\frac{\partial^2 \varphi_x}{\partial y^2}\right)+(1+\nu)\left(\frac{\partial^2 \varphi_x}{\partial x^2}+\frac{\partial^2 \varphi_y}{\partial x\partial y}\right)\right]\\ -k^2 Gh\left(1+\alpha\frac{\partial}{\partial t}\right)\left(\varphi_x+\frac{\partial w}{\partial x}\right)\end{aligned} \tag{2.47}$$

$$\begin{aligned}\frac{\rho h^3}{12}\ddot{\varphi}_x = \frac{D}{2}\left(1+\alpha\frac{\partial}{\partial t}\right)\left[(1-\nu)\left(\frac{\partial^2 \varphi_x}{\partial x^2}+\frac{\partial^2 \varphi_x}{\partial y^2}\right)+(1+\nu)\left(\frac{\partial^2 \varphi_x}{\partial x^2}+\frac{\partial^2 \varphi_y}{\partial x\partial y}\right)\right]\\ -k^2 Gh\left(1+\alpha\frac{\partial}{\partial t}\right)\left(\varphi_x+\frac{\partial w}{\partial x}\right),\end{aligned} \tag{2.48}$$

where $k_s = \rho_w g$ is the stiffness of the Kelvin foundation, c_s is the hydrodynamic damping coefficient, F is the amplitude of the load, ω is the angular frequency of the loading on the plate and $\delta(\dots)$ is the Dirac delta function. Boundary conditions for the simply supported plate are:

At $x=0$ and $x=L_x$:

$$w=0 \tag{2.49}$$

$$\varphi_y=0 \tag{2.50}$$

$$m_{xx} = D\left(1+\alpha\frac{\partial}{\partial t}\right)\left(\frac{\partial \varphi_x}{\partial x}+\nu\frac{\partial \varphi_y}{\partial y}\right)=0, \tag{2.51}$$

where m_{xx} is the bending moment about the y-axis.

At $y=0$ and $y=L_y$:

$$w=0 \tag{2.52}$$

$$\varphi_x=0 \tag{2.53}$$

$$m_{yy}=D\left(1+\alpha\frac{\partial}{\partial t}\right)\left(\nu\frac{\partial\varphi_x}{\partial x}+\frac{\partial\varphi_y}{\partial y}\right)=0 \tag{2.54}$$

where m_{yy} is the bending moment about the x-axis. The analytical solution for the response of the plate is derived in Appendix 1.

2.5.2 Comparison of results of the undamped lattice model and analytical solution

The eigenfrequencies, deflection and rotations, evaluated both with the lattice and continuum model are compared in this section. Input for the analysis is based on sea ice properties and summarised in Table 2-1 in the previous section. In addition, the dimensions of the plate L_x and L_y are 60m and 100m respectively. Hydrodynamic and material damping are initially set to zero.

The deflected shape of the plate under static loading is shown in Figure 2-15. Both the continuum model and the lattice model give the same deflected shape.

The eigenfrequencies of the continuum model are compared to the eigenfrequencies of the lattice model for three different cell sizes: 19 nodes in x- and 31 nodes in y-direction, 31 nodes in x- and 51 nodes in y-direction and 61 nodes in x- and 101 nodes in y-direction. Results are presented in Table 2-2.

For low frequencies (up to mode 6), the eigenfrequencies of the 19x31 nodes lattice and continuum model correspond very well. For higher frequency vibrations a finer mesh is required to assure the correspondence. Some differences remain even in the case of the smallest cell size. These can always be minimized by making the lattice finer.

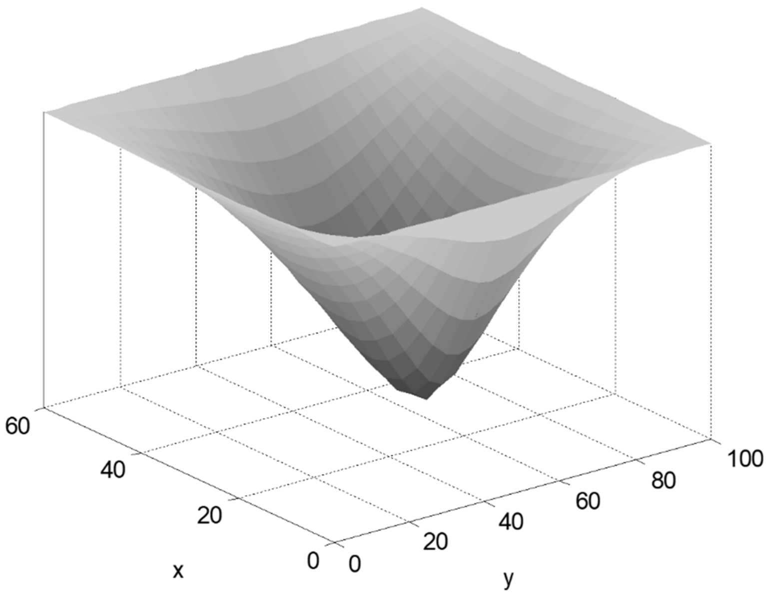

Figure 2-15: Deformation of the simply supported plate on Kelvin foundation under static load F

The deflection amplitude at the loading point normalized by the static deflection is plotted for different excitation frequencies in Figure 2-16. The continuum model response is displayed with a solid line, whereas the lattice response is shown by the dashed lines. At the natural frequencies the deflection of the node approaches infinity as no damping is accounted for. Results obtained with the lattice model for two different mesh sizes are plotted: 19 nodes in x- and 31 nodes in y-direction and 31 nodes in x- and 51 nodes in y-direction. The lattice model predictions correspond to those of the continuum model very well for low excitation frequencies. For higher frequencies (starting from about 6 Hz) a smaller cell size is required to predict the resonance frequencies more accurately. It can be noted that a number of eigenmodes, for example mode 2, cannot be identified from this graph due to the fact that the modal shape for these eigenmodes have a node right at the loading point (this corresponds to zero amplitude in the graph).

Table 2-2: Eigenfrequency [Hz] of the lattice model for three different cell sizes compared with those of the continuum model

Mode	Continuum	Lattice 19x31	Lattice 31x51	Lattice 61x101
1	0.655348	0.655400	0.655460	0.655486
2	0.981122	0.980178	0.980844	0.981126
3	1.586581	1.586147	1.586449	1.586592
4	1.627973	1.632654	1.629670	1.628438
5	2.003042	2.001152	2.002364	2.002905
6	2.465026	2.470323	2.466879	2.465510
7	2.633494	2.622802	2.629628	2.632550
8	3.378501	3.409284	3.389306	3.381193
9	3.519075	3.500945	3.512461	3.517431
10	3.603406	3.624535	3.610731	3.605226
11	3.757975	3.772677	3.762984	3.759215
12	4.389615	4.379851	4.385800	4.388645
13	4.655891	4.636690	4.648665	4.654066
14	4.991826	5.044982	5.010098	4.996319
15	5.271395	5.232394	5.256989	5.267768
16	5.829436	5.933866	5.865418	5.838279
17	6.038309	6.030671	6.034657	6.037315
18	6.205250	6.280565	6.230735	6.211467
19	6.399836	6.331901	6.374797	6.393525
20	6.621979	6.730615	6.658921	6.631006

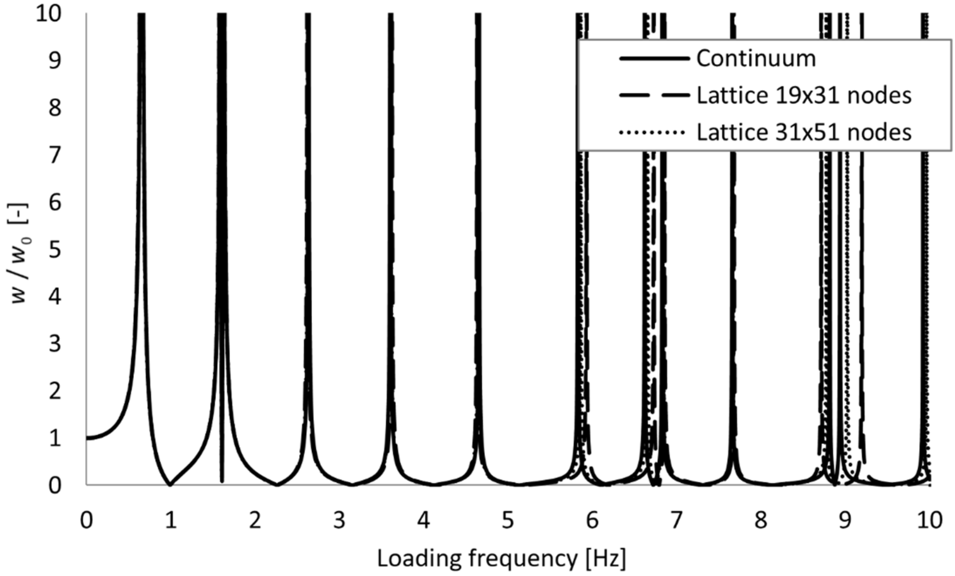

Figure 2-16: Amplitude of the deflection at the point under the load, normalized by the deflection of the same point under static load as function of the loading frequencies for various cell sizes

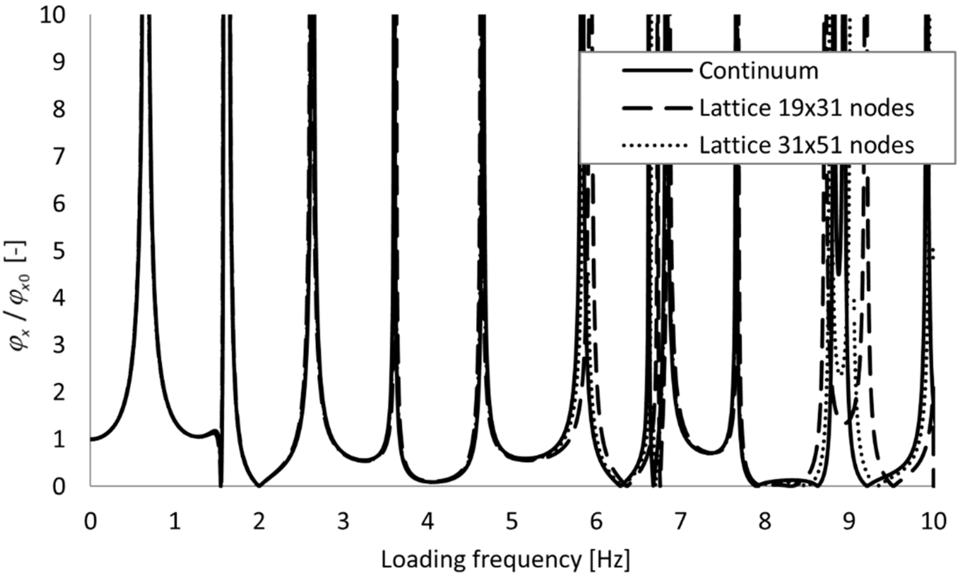

Figure 2-17: Normalized amplitude of the rotation in x-direction at the loading point as function of the loading frequency for various cell sizes

The amplitude of rotation under the load in x-direction of the plate normalized by the static rotation is plotted for different excitation frequencies in Figure 2-17. Similar correspondence is found as for the amplitude of the displacement of the plate.

To confirm the influence of the mesh size of the lattice model, the directional characteristics of the deflection wave propagating through the continuum and the lattice structure are presented in Figure 2-18. For low frequency waves there is no difference between the lattice model and the continuum model. For higher loading frequency, in Figure 2-18b, the lattice model of cell size 1m (61x101 nodes) is in good agreement with the continuum solution. For larger mesh size, the results obtained with the lattice model start deviating from the results obtained with the continuum solution and the influence of the lattice anisotropy becomes clear from the loss of circular shape of the lattice solution. The variations originating from anisotropy in the lattice model are small and the clear differences between the lattice and continuum response at >5Hz loading frequency (31rad/s) in Figure 2-16 and in Figure 2-17 are mainly attributed to boundary effects of the lattice model, amplifying the small differences originating from anisotropy in the finite lattice model.

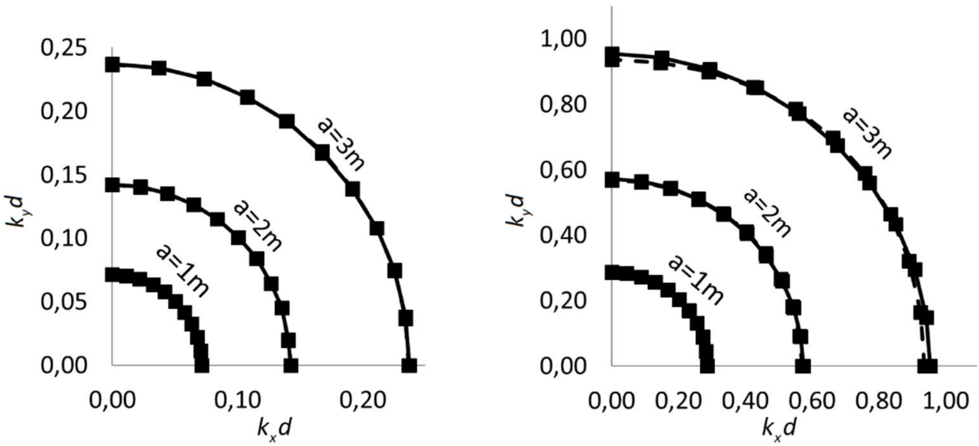

Figure 2-18: Directional characteristics of deflection waves propagating through the Mindlin-Reissner continuum (solid lines) and the lattice model (dashed lines) for various cell size for angular frequency of a) 5rad/s and b) 66rad/s

2.5.3 Comparison of results with hydrodynamic damping

The influence of the hydrodynamic damping coefficient on the response amplitude of deflection and rotation of the plate is studied in this subsection. Three damping coefficients were applied and set proportional to the mass of the plate and the stiffness of the Kelvin foundation. Results are presented in Figure 2-19 for deflection and in Figure 2-20 for rotation in x-direction. The mesh size of the lattice model was 19x31 nodes in all cases. The continuum response is displayed with a solid line, dashed line and dash-dotted line for various damping coefficients, whereas the lattice response is for all damping coefficients indicated with a dotted line, which starts deviating from the corresponding continuum curve at higher frequencies.

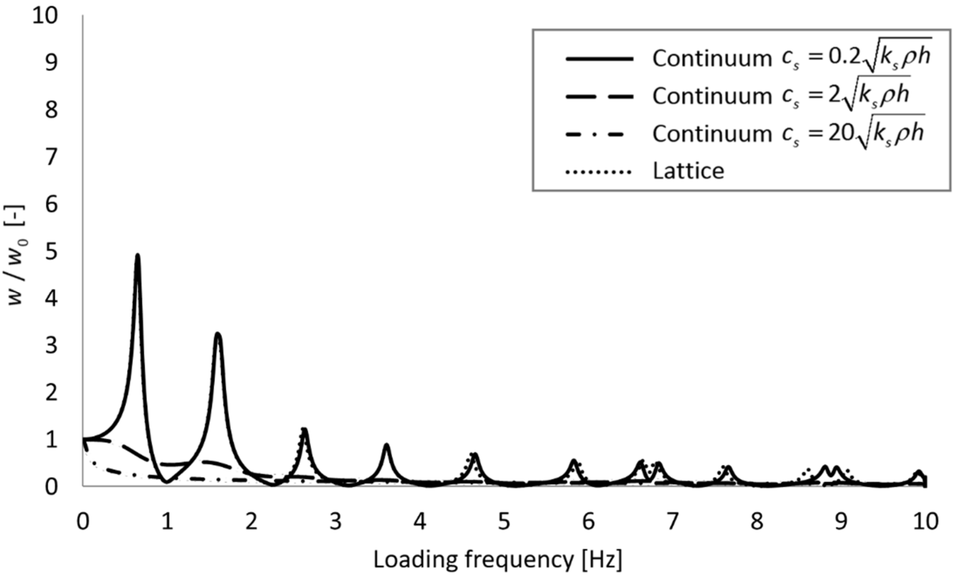

Figure 2-19: Amplitude of the deflection at the point under the dynamic load, relative to the deflection of the same point under static loading for various loading frequencies. Different line styles represent different hydrodynamic damping coefficients. The dotted lines show the predictions of the lattice model.

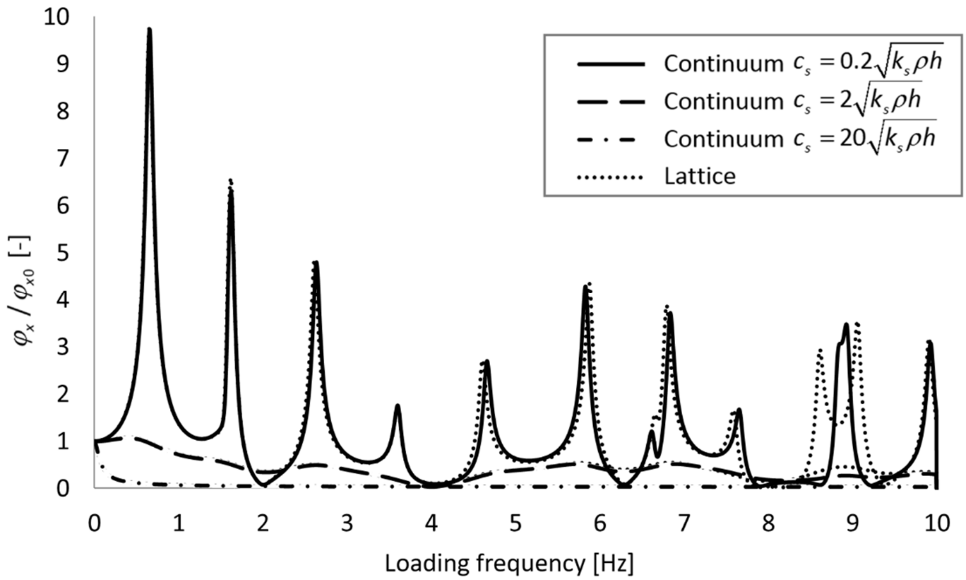

Figure 2-20: Amplitude of the rotation in x-direction at the point under the dynamic load, relative to the deflection of the same point under static loading for various loading frequencies. Different line styles represent different hydrodynamic damping coefficients. The dotted lines show the predictions of the lattice model.

For the lower frequencies the lattice model predicts the response amplitudes very well in all cases. For the higher frequencies the lattice of 19x31 nodes gives difference in results, when compared to the analytical solution. In cases with high damping this difference is not observed.

2.5.4 Comparison of results with material damping

The influence of the material damping coefficient on the response amplitude of deflection and rotation of the plate is studied in this subsection. Stiffness proportional damping is applied in this study, where the damping force is proportional to the rotational and translational velocity of the particles. For sea ice, a representative stiffness-proportional damping coefficient was not found in literature. Marchenko and Cole (2017) described three physical mechanisms of energy dissipation in sea ice: an-elastic and viscous deformations, friction loss due to migration brine and friction on the ice-water interface. The assumption that the energy dissipation is directly proportional to the velocity of deformations in the lattice is a simplification. It is expected that the material damping has a negligible effect compared to the hydrodynamic damping in case of out-of-plane deformations.

Results for three different damping coefficients are presented in Figure 2-21 for deflection and in Figure 2-22 for rotation in x-direction. The mesh size of the lattice model was 19x31nodes in all cases. The continuum response is displayed with a solid line, dashed line and dash-dotted line for various material damping coefficients, whereas the lattice response is for all damping coefficients indicated with a dotted line, which starts deviating from the corresponding continuum curve at higher frequencies.

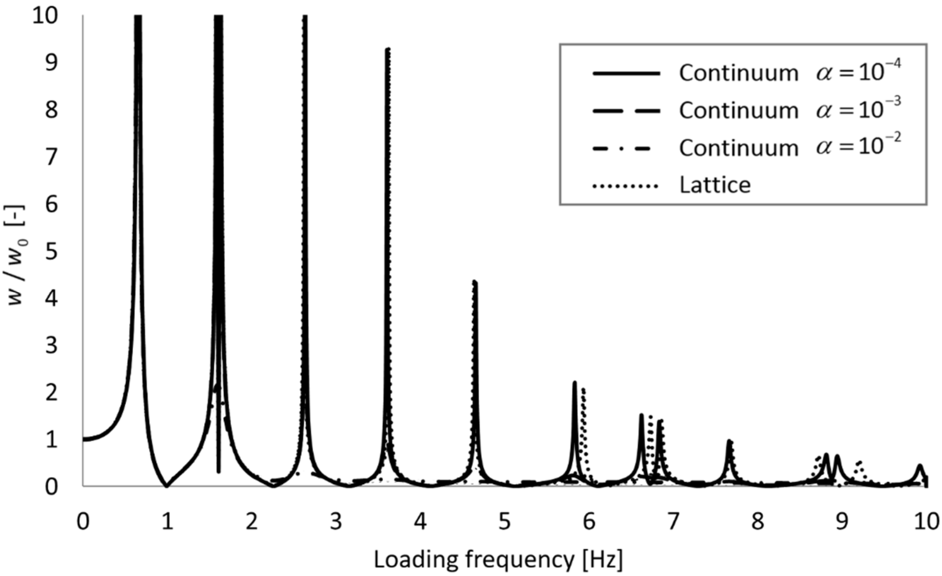

Figure 2-21: Amplitude of the deflection at the point under the dynamic load, relative to the deflection of the same point under static loading for various loading frequencies. Different line styles represent different material damping coefficients in the continuum model. The dotted lines show the predictions of the lattice model.

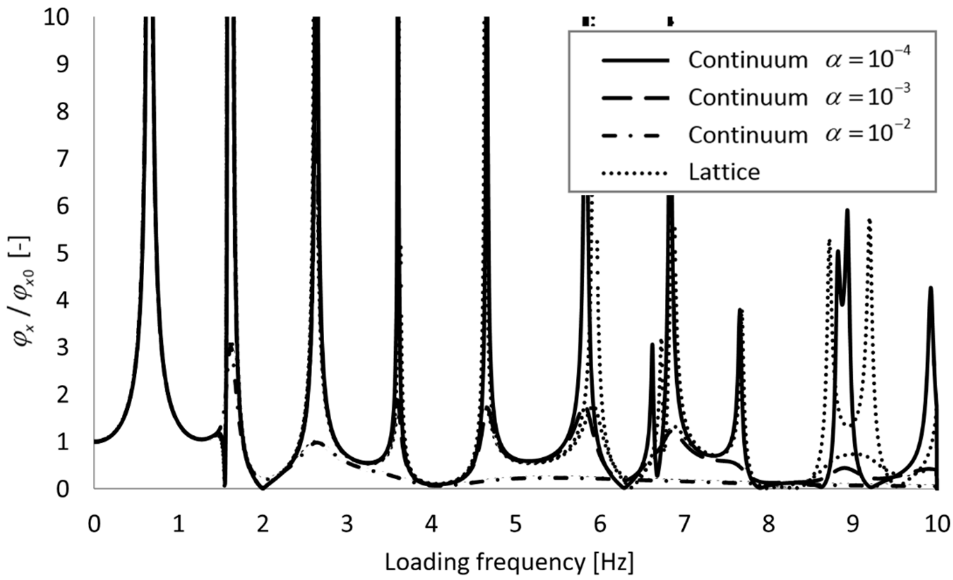

Figure 2-22: Amplitude of the rotation in x-direction at the point under the dynamic load, relative to the deflection of the same point under static loading for various loading frequencies. Different line styles represent different material damping coefficients in the continuum model. The dotted lines show the predictions of the lattice model.

Again, for the lower frequencies the lattice model predicts the response amplitudes very well in all cases. For the higher frequencies the lattice of 19x31 nodes gives difference in results, when comparing to the analytical solution. In cases with high damping this difference is not observed.

For low-frequency motions, the material damping has limited effect in case $\alpha \leq 10^{-3}$ is selected. This is applied in further examples in this document, where in most cases the out-of-plane deformations are governing and loading frequencies are low.

2.6 Conclusions

For the first time a lattice model for the out-of-plane dynamics of a shear-deformable plate has been formulated. The model is composed of masses and springs whose morphology and properties were derived to match, in the long-wave approximation, the out-of-plane deformations of thick plates as described by the Mindlin-Reissner theory.

The model can be applied in various fields of engineering, but is discussed taking example of an ice sheet, as it was derived with the intention to simulate ice-structure interaction. Focussing upon linear dynamics of the model, consistency with a continuum plate theory in the low frequency band is shown and differences emerging at higher frequencies are attributed to the dispersion, anisotropy and specific boundary effects (in case of finite dimensions) of the lattice model.

Wave dispersion analysis shows that for long waves the dispersion curves of the waves in the lattice match very closely with those of the continuum plate. For shorter waves with a higher wave number correspondence reduces. These results are in line with expectations, yet they show that for every lattice period there is a specific value of the frequency/wavenumber starting from which the lattice response to a load will be different from that of the continuum plate due to the difference in the dispersion characteristics.

A study of directional characteristics of propagating waves in the lattice model shows good correspondence between the lattice model and continuum plate for long waves. The agreement between the lattice model and the Mindlin-Reissner continuum solution reduces for higher angular frequencies due to the anisotropy of the lattice. The larger the interparticle distance, the lower the frequency at which the anisotropy starts to play a role. Wavelengths smaller than two times the cell size cannot be described with the lattice model.

The eigenfrequencies and the steady-state response of the lattice model, representing a simply supported plate of ice of finite dimensions, to a sinusoidal in time point load are computed and compared to those of a corresponding continuum plate. It is proven that at low frequencies the developed lattice predicts the same dynamic behaviour as the corresponding continuum plate. For larger lattice period, the results obtained with the lattice model start deviating from those obtained using the continuum theory. The deviations originating from anisotropy in the lattice model are small at these frequencies and the differences between the lattice and continuum response are attributed to boundary effects of the lattice model. Effects of hydrodynamic and material damping have been effectively included in the model and have shown good correspondence with the continuum solution.

The advantage of using springs in the lattice model rather than beams or bars is that bending, torsion and shear are decoupled. Compared to a continuum model, the lattice model has advantages regarding modelling of fracture. This makes the lattice model an enabler for material modelling in various fields of engineering, one of which is simulation of ice-structure interaction.

3

Spring stiffnesses for in- and out-of-plane deformations and resulting Poisson effect

3.1 Introduction

As presented in Chapter 2, the equations of motion of the cells in the lattice model and spring stiffness parameters were derived to match the continuum model of a shear-deformable plate in the long wave approximation. A study of dynamic behaviour, wave dispersion and directional characteristics of propagating waves in the lattice model showed good correspondence between the lattice model and continuum plate for long waves. In this Chapter, parameters of the lattice model are derived to include in-plane deformations. Alternative spring stiffnesses for the lattice model were derived based on the method presented by Hrennikoff (1940). Study of the Poisson effect showed discrepancies between expected deformations and deformations found with the lattice model, when applying stiffness parameters with the original method, but not when applying stiffness parameters derived with the method based on the work by Hrennikoff (1940). The dynamic verification exercise from Chapter 2 was repeated to test the applicability of the new stiffness parameters in simulating dynamic behaviour of an ice plate. For Poisson's ratio of $\nu = \frac{1}{3}$, which is often applied for sea ice, both methods give the same parameters for the lattice model.

3.2 Equations of motion for in-plane deformations of the lattice model

In a similar manner to the derivation of the equations of motion for out-of-plane deformation of a shear deformable plate in Chapter 2, the equations of motion for the inner cell were derived for in-plane deformations in literature (Suiker et al., 2001a). The continualised equations of motion from this work are used here. This gives, for the axis system presented in Figure 2-2 and connections presented in Figure 3-1:

$$\begin{aligned} \frac{M}{d^2}\ddot{\tilde{u}}_x &= \left(K_{sip,axi} + K_{nip,dia} + K_{sip,dia}\right)\frac{\partial^2 \tilde{u}_x}{\partial x^2} + 2\left(K_{nip,dia} + K_{sip,dia}\right)\frac{\partial^2 \tilde{u}_y}{\partial x \partial y} \\ &+ \left(K_{nip,axi} + K_{nip,dia} + K_{sip,dia}\right)\frac{\partial^2 \tilde{u}_x}{\partial y^2} \end{aligned} \tag{3.1}$$

$$\begin{aligned} \frac{M}{d^2}\ddot{\tilde{u}}_y &= \left(K_{nip,axi} + K_{nip,dia} + K_{sip,dia}\right)\frac{\partial^2 \tilde{u}_y}{\partial y^2} + 2\left(K_{nip,dia} + K_{sip,dia}\right)\frac{\partial^2 \tilde{u}_x}{\partial x \partial y} \\ &+ \left(K_{sip,axi} + K_{nip,dia} + K_{sip,dia}\right)\frac{\partial^2 \tilde{u}_y}{\partial x^2} \end{aligned} \tag{3.2}$$

where $K_{nip,axi}$ and $K_{sip,axi}$ are the axial and shear stiffness respectively of the springs in axial in-plane direction and $K_{nip,dia}$ and $K_{sip,dia}$ are the axial and shear stiffness respectively of the springs in diagonal in-plane direction. $\tilde{u}_x$ and $\tilde{u}_y$ follow from the Taylor approximations of the continuous field variables $u_x^{(m+p,n+q)}$ and $u_y^{(m+p,n+q)}$ for in-plane deformation in x- and y-direction respectively.

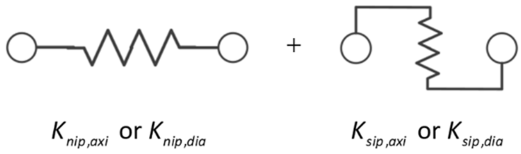

Figure 3-1: Axial and diagonal connections between the nodes in the lattice model for in-plane deformations, consisting of normal and shear springs (A-A' and B-B' in Figure 2-3)

Equations of motion for a shear deformable plate loaded in in-plane and out-of-plane direction, assuming plane stress state, excluding thermal effects and assuming small strains and rotations, are presented in, for example, Reddy (1999):

$$\rho h\ddot{u}_x = \frac{Eh}{1-\nu^2}\left(\frac{\partial^2 u_x}{\partial x^2}\right) + \frac{\nu Eh}{1-\nu^2}\left(\frac{\partial^2 u_y}{\partial x\partial y}\right) + \frac{Eh}{2(1+\nu)}\left(\frac{\partial^2 u_x}{\partial y^2} + \frac{\partial^2 u_y}{\partial x\partial y}\right) \tag{3.3}$$

$$\rho h\ddot{u}_y = \frac{Eh}{1-\nu^2}\left(\frac{\partial^2 u_y}{\partial y^2}\right) + \frac{\nu Eh}{1-\nu^2}\left(\frac{\partial^2 u_x}{\partial x\partial y}\right) + \frac{Eh}{2(1+\nu)}\left(\frac{\partial^2 u_y}{\partial x^2} + \frac{\partial^2 u_x}{\partial x\partial y}\right) \tag{3.4}$$

$$\rho h\ddot{w} = k^2 Gh\left(\frac{\partial^2 w}{\partial x^2} + \frac{\partial^2 w}{\partial y^2} + \frac{\partial \varphi_x}{\partial x} + \frac{\partial \varphi_y}{\partial y}\right) \tag{3.5}$$

$$\frac{\rho h^3}{12}\ddot{\varphi}_x = \frac{D}{2}\left[(1-\nu)\left(\frac{\partial^2 \varphi_x}{\partial x^2} + \frac{\partial^2 \varphi_x}{\partial y^2}\right) + (1+\nu)\left(\frac{\partial^2 \varphi_x}{\partial x^2} + \frac{\partial^2 \varphi_y}{\partial x\partial y}\right)\right] - k^2 Gh\left(\varphi_x + \frac{\partial w}{\partial x}\right) \tag{3.6}$$

$$\frac{\rho h^3}{12}\ddot{\varphi}_y = \frac{D}{2}\left[(1-\nu)\left(\frac{\partial^2 \varphi_y}{\partial y^2} + \frac{\partial^2 \varphi_y}{\partial x^2}\right) + (1+\nu)\left(\frac{\partial^2 \varphi_y}{\partial y^2} + \frac{\partial^2 \varphi_x}{\partial x\partial y}\right)\right] - k^2 Gh\left(\varphi_y + \frac{\partial w}{\partial y}\right) \tag{3.7}$$

Equations (3.5) to (3.7) are matched in the long-wave approximation for the lattice model for out-of-plane deformations, as shown in Chapter 2. Equations (3.3) and (3.4) are matched by assigning the following parameters to the in-plane connections of the plate:

$$K_{n,axi} = \frac{(3-\nu)Eh}{4(1-\nu^2)} \tag{3.8}$$

$$K_{n,dia} = \frac{Eh}{4(1-\nu)} \tag{3.9}$$

$$K_{s,axi} = \frac{(1-3\nu)Eh}{4(1-\nu^2)} \tag{3.10}$$

$$K_{s,dia} = 0 \tag{3.11}$$

These stiffnesses will be referred to in this document as the stiffnesses derived with the "Equations-matching" method. The mass of the cells is the same as for the out-of-plane equations, derived in Chapter 2.

3.3 Alternative method of deriving stiffness parameters for the lattice model

Hrennikoff (1940) presented a method to replace a solid medium by a framework of articulated elastic bars. For a lattice with the same pattern as that considered in Chapter 2, the parameters of the axial springs are given via $K = \frac{EA}{L}$ where K is the spring stiffness A is the bar area and L is the length. For a framework of springs with layout presented in Figure 2-2 and connections presented in Figure 3-1, this would result in:

$$K_{nip,axi} = \frac{Eh}{(1+\nu)} \tag{3.12}$$

$$K_{nip,dia} = \frac{\nu Eh}{(1-\nu^2)} \tag{3.13}$$

The framework equation for shear is only satisfied if $\nu = \frac{1}{3}$ in plane stress condition. This problem can be overcome by using shear springs on the axial connections. The shear spring stiffness for these connections is:

$$K_{sip,axi} = \frac{Eh}{1+\nu} - 2\frac{\nu Eh}{1-\nu^2} \tag{3.14}$$

The shear spring stiffness is positive for $\nu \le \frac{1}{3}$.

For bending of thin plates the framework parameters are found via $G = \frac{EI}{L}$, where G is the stiffness of the bending spring, I is the moment of inertia of the beam in the framework and L is the length of the beam. For a framework of springs with layout presented in Figure 2-2 and connections presented in Figure 2-4, this would result in:

$$G_{r,axi} = (1-\nu)D \tag{3.15}$$

$$G_{t,dia} = \nu D \tag{3.16}$$

Torsion conditions are only satisfied for $\nu = \frac{1}{3}$. An axial torsion beam is included to resolve this with the stiffness:

$$G_{t,axi} = (1-3\nu)D \tag{3.17}$$

The axial torsion spring stiffness is positive for $\nu \le \frac{1}{3}$. These stiffnesses will be further referred to in this document as the stiffnesses derived with the "Hrennikoff" method.

3.4 Study of the Poisson effect by different parameter sets

Poisson's ratio of a material is the ratio between transverse and axial strain when stretched or compressed. For a square lattice cell in a plate model that is loaded in in-plane condition by distributed load f at two opposing edges, as shown in Figure 3-2, it is expected that the axial strain in the connections between nodes 1 and 2 and 3 and 4 is three times higher than the contraction in the connections between nodes 1 and 3 and 2 and 4. Appendix 2 explains how the strains in the connections of the lattice are calculated for these loading conditions. For Poisson's ratio of $\nu = \frac{1}{3}$, the stiffnesses of the lattice cells are the same for both the "Equations-matching" and the "Hrennikoff" method and the strain and contraction in the connections is as expected.

If Poisson's ratio of $\nu = \frac{1}{4}$ is applied, the contraction of the plate in y-direction is expected to be 0.25 times the elongation in x-direction. However, for a square lattice cell with stiffness parameters obtained with the "Equations-matching" method, a length increase in x-direction of 0.32 times the length increase in y-direction is found. When stiffnesses are applied that are obtained with the "Hrennikoff" method, the ratio between strain in x- and y- direction is as expected. Similarly, substituting Poisson's ratio $\nu = 0$ should give zero diagonal spring stiffness, such that there is no deformation in y-direction. This is only the case for the spring stiffnesses derived with the "Hrennikoff" method.

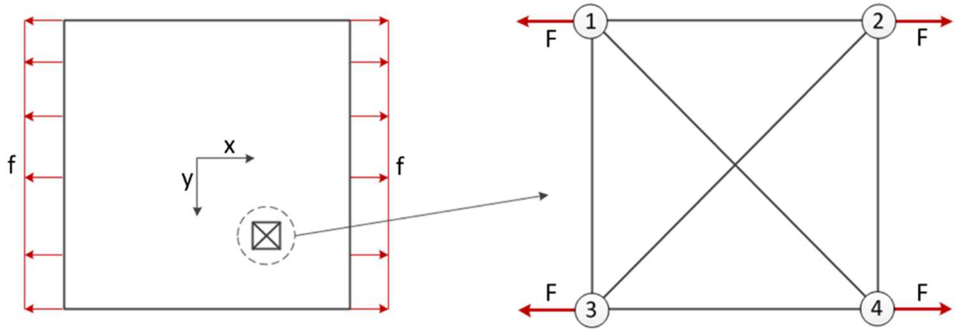

Figure 3-2: Square lattice cell in uni-axial stress condition. F is the load that is transferred to the lattice cell

Only the parameters derived with "Hrennikoff" method result in the expected Poisson's effect in the lattice model. To check the applicability of these parameters to simulate dynamic behaviour of an ice plate, the dynamic verification exercise from Chapter 2 is repeated, where a simply supported plate under cyclic loading conditions was studied. Hereto, the stiffness parameters of the lattice connections are changed from values obtained with the "Equations-matching" method to values obtained with the "Hrennikoff" method. Stiffnesses from the "Hrennikoff" method are associated with a thin plate and therefore do not include out-of-plane shear stiffness. This is included as per "Equations-matching" method (equation (2.23)). A grid of 19x31 masses and Poisson's ratio of $\nu = 0.15$ was selected to generate results. Other parameters are reported in Sections 2.4 and 2.5. For comparison, the same simulation is done with the stiffnesses from "Equations-matching" method and reduced Poisson's ratio of $\nu = 0.15$.

Normalised deflection and rotation at the loading point for varying frequency are presented in Figure 3-3 and Figure 3-4 respectively. For low loading frequency, there is good agreement between lattice model and continuum response, for stiffnesses derived with both methods. For higher frequencies, the results obtained with the lattice model deviate from the continuum results and the deviation is slightly larger and observed at lower frequencies with the lattice model with “Hrennikoff” stiffnesses.

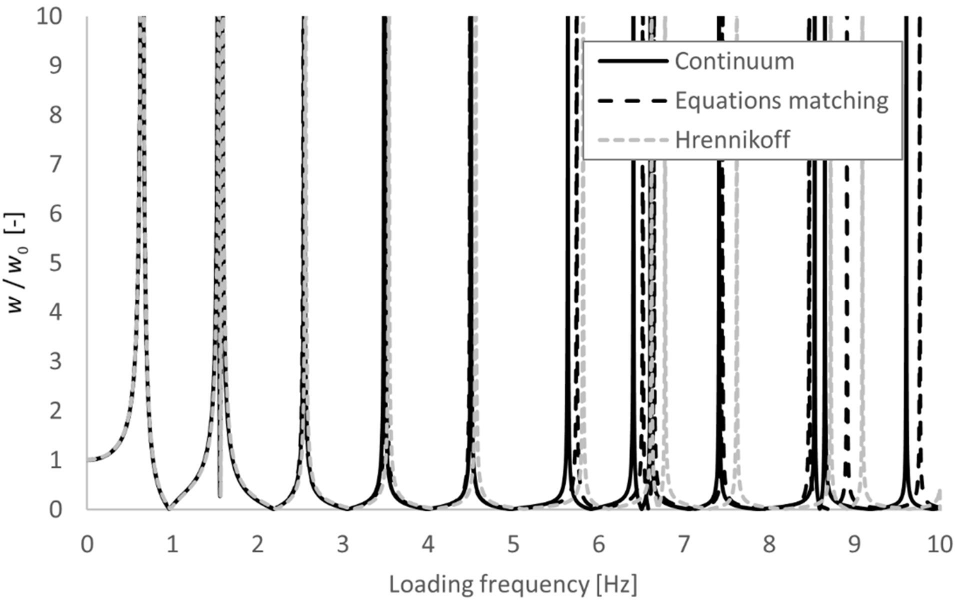

Figure 3-3: Amplitude of the deflection at the point under the load, normalized by the deflection of the same point under static load as function of the loading frequencies for a continuum and a lattice with stiffness parameters derived with the “Equations-matching” and the “Hrennikoff” method

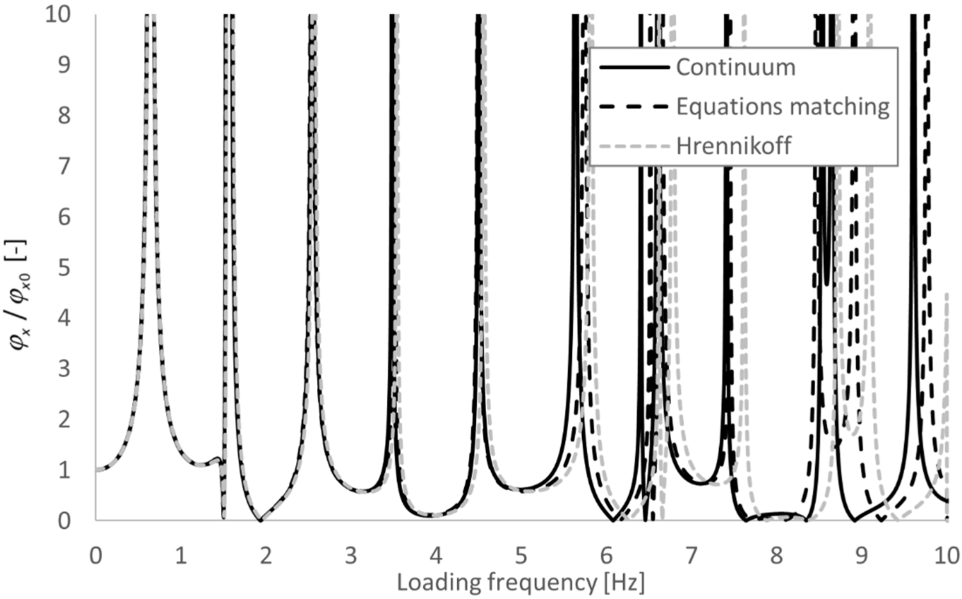

Figure 3-4: Normalized amplitude of the rotation in x-direction at the loading point as function of the loading frequency for a continuum and a lattice with stiffness parameters derived with the "Equations-matching" and the "Hrennikoff" method

The most relevant processes in failure of ice interacting with sloping structures are associated with the lower frequencies, where both methods provide good agreement with the continuum. The parameters obtained with "Hrennikoff" method result in proper inclusion of the Poisson effect in the lattice cells. Therefore, the parameters derived with this method are used for further study of sea ice fracture in this thesis:

$$M = \rho h d^2 \tag{3.18}$$

$$I = \frac{1}{12} \rho h^3 d^2 \tag{3.19}$$

$$K_{nip,axi} = \frac{Eh}{(1+\nu)} \tag{3.20}$$

$$K_{sip,axi} = \frac{Eh}{1+\nu} - 2\frac{\nu Eh}{1-\nu^2} \text{ with } \nu \le \frac{1}{3} \tag{3.21}$$

$$K_{nip,dia} = \frac{\nu Eh}{(1-\nu^2)} \tag{3.22}$$

$$K_{s,axi} = k^2 Gh \tag{3.23}$$

$$G_{r,axi} = (1-\nu)D \tag{3.24}$$

$$G_{t,axi} = (1-3\nu)D \text{ with } \nu \leq \frac{1}{3} \tag{3.25}$$

$$G_{t,dia} = \nu D \tag{3.26}$$

For $\nu = \frac{1}{3}$ the stiffness parameters derived with both methods are in agreement. This is a typical value for sea ice and therefore this value is used in practical examples in this document.

3.5 Discussion

The Poisson effect cannot be captured with the lattice model that was derived in Chapter 2. This could mean that a lattice model with a regular mesh and only closest neighbour interactions is only applicable for modelling of a shear deformable plate loaded in-plane and out-of-plane in case Poisson's ratio equals $\nu = \frac{1}{3}$.

The limit of Poisson's ratio is a known problem in lattice models composed of translational springs with central forces based on distance alone (Donzé and Magnier, 1995; Hrennikoff, 1940; Pan et al., 2018). Different Poisson's ratios can arise from deviations, such as non-central forces between particles in the solid, forces which do not depend on distance alone, or anisotropy (Lakes, 1991).

One of the solutions described in literature is the inclusion of shear springs (Kawai, 1978; Zubelewicz and Bažant, 1987; Zhao et al., 2011), giving a similar model to that derived with the "Hrennikoff" method in this Chapter. These models are not directly linked to those of the classical plate models, such as Mindlin-Reissner plate theory, which is the case with the model derived in Chapter 2. Other solutions to the limit of Poisson's ratio of lattice models described in literature include addition of an energy term for the resistance to volume change of the lattice cell (Grassl et al., 2006), introducing an extra fourth-dimensional interaction to the lattice (Zhao, 2017), inclusion of angular springs (Ostoja-starzewski, 2002) and introducing anisotropy (Kot and Nagahashi, 2017).

A lattice model that corresponds with classic continuum theory could perhaps be created by including additional degrees of freedom, dimensions, or active energy supply. With a lattice model with a regular mesh and only closest neighbour interactions a corresponding model is limited to Poisson's ratio $\nu = \frac{1}{3}$.

3.6 Conclusions

Parameters of the lattice model are derived to include in-plane deformations, such that, combined with the work presented in Chapter 2, in the long-wave limit the lattice dynamics reduces to the plate equations of a shear deformable plate loaded in in-plane and out-of-plane direction.

Alternative spring stiffnesses for the lattice model were derived based on the method presented by Hrennikoff (1940). A study of the Poisson effect showed discrepancies between theory and deformations found with the lattice model, when applying stiffness parameters obtained with the original method, but not when stiffness parameters derived with the method based on the work by Hrennikoff (1940) were used.

The steady-state response of the lattice model, representing a simply supported plate of ice, to a sinusoidal in time point load is computed and compared to that of a corresponding continuum plate, using original stiffnesses and those derived with the method based on Hrennikoff (1940). For low loading frequency, there is good agreement between lattice model and continuum response, for stiffnesses derived with both methods. For higher frequencies, the results obtained with the lattice model deviate from the continuum results and the deviation is slightly larger and observed at lower frequencies with the lattice model with "Hrennikoff" stiffnesses.

The most relevant processes in failure of ice interacting with sloping structures are associated with the lower frequencies, where both methods provide good agreement with the continuum. The parameters obtained with "Hrennikoff" method result in proper inclusion of the Poisson effect in the lattice cells. Therefore, the parameters derived with this method are used for further study of sea ice fracture.

For Poisson's ratio of $\nu = \frac{1}{3}$ the stiffness parameters derived with both methods are in agreement. This is a typical value for sea ice and therefore this value is selected for practical examples of ice failure in the next Chapters of this document.

The limit of Poisson's ratio is a known problem in lattice models composed of translational springs with central forces based on distance. A lattice model that corresponds with classic continuum theory could perhaps be created by including additional degrees of freedom, dimensions, or active energy supply. With a lattice model with a regular mesh and only closest neighbour interactions a corresponding model is limited to Poisson's ratio $\nu = \frac{1}{3}$.

4

Failure criteria for simulation of sea-ice fracture in interaction with a sloping structure

In this Chapter, failure criteria are derived to simulate ice failure in interaction with sloping structures. In the second and third Chapter, the lattice model for in- and out-of-plane deformations of a shear deformable plate is described and it is shown that the equations of motion of the plate match the Mindlin Reissner equations in the long wave approximation. By linking the lattice model to continuum theory following the method by Hrennikoff (1940), the Poisson effect is accounted for.

The main focal area of this chapter is the derivation of failure criteria for a 2D lattice model for sea-ice, considering both in-plane and out-of-plane deformations. The criteria are based on first principles, enabling physically sound simulation of failure processes that occur in

---

This chapter is submitted to Cold Regions Science and Technology to be considered for publication. Parts have been moved to other Chapters for consistency.

ice-structure interaction. The failure criteria are linked to ice property measurements and failure envelopes are presented. Near a crack tip, strains concentrate. After deriving failure criteria for an intact plate, strain concentrations are studied and special failure criteria for application near crack tips are derived and linked to field measurements, completing the set of failure criteria that is required to simulate ice-structure interaction scenarios. It is shown that the failure criteria have a minimal dependence on cell-size and -orientation. The lattice model and failure criteria are further validated in Chapter 5 and 6 by simulation of field and basin tests.

4.1 Failure criteria for a continuous ice plate

For cells in an intact mesh, i.e. for those that are not located near a crack-tip or other discontinuities where stresses concentrate, failure criteria are derived in this section. First, the failure criteria for in-plane deformations are derived and linked to multi-axial compression and tension measurement data. Then the failure criteria for out-of-plane bending deformations are derived and linked to measurement parameters. By translating deformation in bending into corresponding strain at the outer fibre of the plate, bending and tensile deformations can be combined into a single failure criterion. Near discontinuities the mesh size influences the magnitude of local deformations and special failure criteria are required. For the latter conditions failure criteria are derived in Section 4.2.

4.1.1 In-plane tensile and compressive failure

Failure of sea-ice plates in in-plane loading has been studied by Richter-Menge and Jones (1993) for tensile loading and by Schulson et al. (2006) for multi-axial compressive loading. Results were presented in a combined failure envelope in the latter study, and copied here for reference in Figure 4-1. Square shaped ice plates were loaded in two directions with stresses σ_{11} and σ_{22} and failure load combinations are indicated with dots. Compressive loading has a positive sign in the figure. Different loading conditions resulted in different failure modes in the tests: splitting under unconfined loading, Coulombic shear friction under lower confinement and spalling under higher confinement. Figure 4-1 shows the effect of multi-axial loading: under low confinement the compressive loading in one direction influences the magnitude of the load that gives failure in the other direction.

The objective of this section is to define failure criteria for tensile and compressive loading of an ice plate, such that the different failure modes are captured and the effects of multi-axial loading are accounted for. The failure envelope in Figure 4-2 is achieved, which, when compared with Figure 4-1, captures well the tensile failure and multi-axial compressive failure under low confinement. To simulate spalling failure under higher confinement, where cracks parallel to the plate surface are created, a 3-dimensional model is required for accurate simulations. In this study, a 2-dimensional model is considered and a limiting failure criterion is defined to approach the failure envelope in spalling conditions.

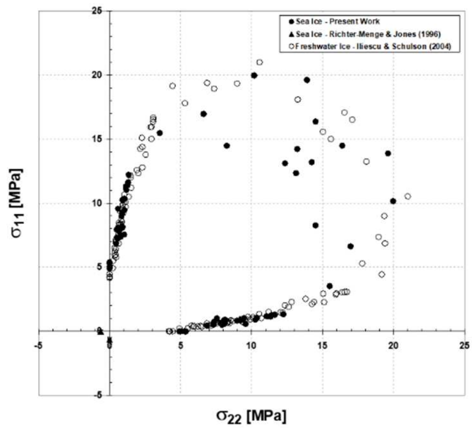

Figure 4-1: Comparison of the brittle failure envelopes at -10°C for first-year sea ice and freshwater ice [from Iliescu and Schulson (2004)] of similar grain size and growth texture. From: Schulson et al. (2006). Note that tension is negative in this figure and compression positive

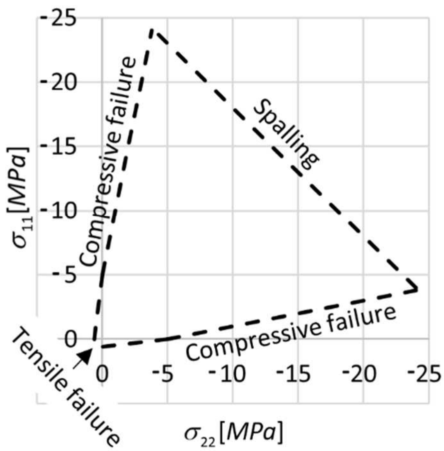

Figure 4-2: Failure envelope for the lattice model

Compressive failure criterion

Figure 4-3 shows a plate with an internal lattice cell, which has orientation α with respect to the x- axis. The plate has free boundaries and is loaded in its plane, with stresses σ_{xx} in x-direction and σ_{yy} in y-direction. Tensile loading is of positive sign. Appendix 1 explains how the axial and shear strains of the connections in the lattice cell under these loading conditions are calculated under varying angle α .

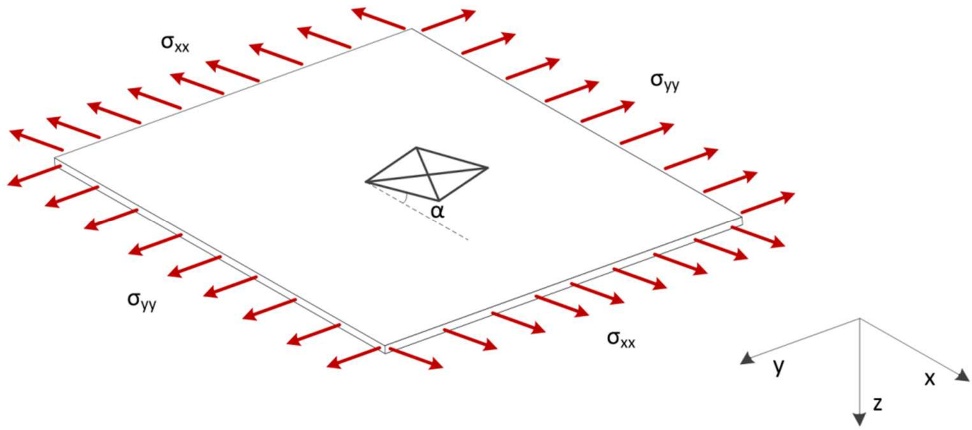

Figure 4-3: Plate loaded in multi-axial tension with internal lattice cell oriented with rotation α relative to the x-axis

Figure 4-4 presents Mohr diagrams for the axial ε_{11} versus shear strain ε_{12} in the axial connections, multiplied by Young's modulus over load ratio $\left(E/\sigma_{xx}\right)$, for varying orientation of the lattice cell from 0 to 180° and varying 'confinement' (relative magnitude of σ_{yy} compared to σ_{xx}). Uni-axial loading is represented with the solid curve. Poisson's ratio of $\nu = \frac{1}{3}$ was selected as a representative value for sea ice. Each orientation α of the lattice cell has a corresponding point on the Mohr circle. The radius and centre point of the circle are not affected by the orientation of the lattice cell.

The radius of the Mohr diagram for axial and shear strain in the axial connections reduces with increasing confinement (dashed and dash-dotted curve). This characteristic is used to capture the increasing capacity of the plate with increasing confinement in multi-axial compressive loading; a failure criterion for compressive loading is therefore based on axial and shear deformation of the axial connections.

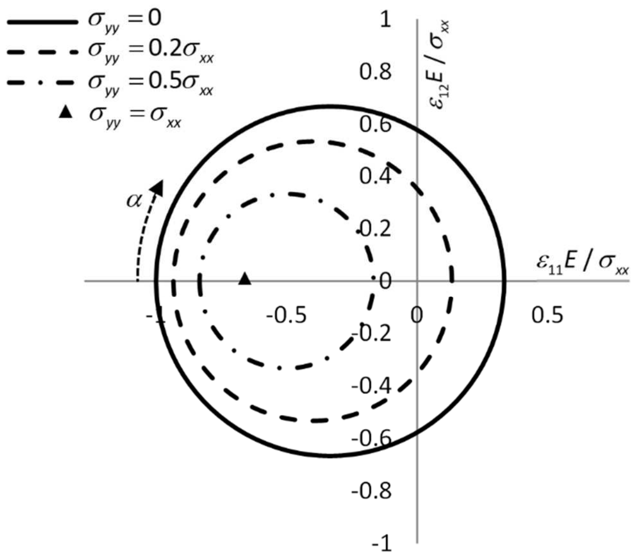

Figure 4-4: Mohr diagram of normal strain and shear strain for uni-axial and multi-axial compressive loading.

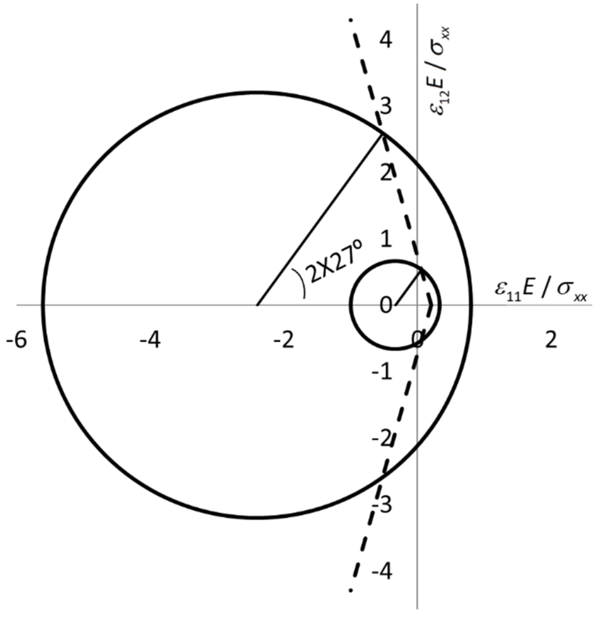

Figure 4-5: Failure occurs if the point on the Mohr diagram at 2x27° with the tensile direction exceeds the linear threshold curve (dashed line). The solid lines indicate Mohr diagrams for different loading conditions: for the larger circle σ_{xx}=-30MPa and σ_{yy}=-6MPa and for the smaller circle σ_{xx}=-5MPa and σ_{yy}=-0. For this plot σ_c=E=5MPa

Applying a Mohr-Coulomb type failure criterion (Coulomb, 1776) would impose failure to occur if the Mohr diagram for stress would exceed a curve with a given slope and intercept parameter. A similar type of failure criterion is applied in the lattice model. In compressive loading conditions under low confinement, the ice failed in Coulombic shear faulting mode in the tests by Schulson et al. (2006). The macroscopic plane of the fault had an angle of $27^{\circ} \pm 4^{\circ}$ with respect to the main loading direction. Failure is set to occur if the point in the Mohr diagram corresponding to an angle of 27° with respect to the least-loaded direction (2x27° in the Mohr diagram) exceeds the threshold curve, indicated by the dashed line in Figure 4-5.

From the strains in the connections of a lattice cell, mean (ε_{mean}) and radius (R_{ε}) of the Mohr circle can be derived that define the deformations at the location of that cell, independently of its orientation:

$$\varepsilon_{mean} = \frac{\varepsilon_{11} + \varepsilon_{22}}{2} \tag{4.1}$$

$$R_{\varepsilon} = \sqrt{\left(\varepsilon_{11} - \varepsilon_{mean}\right)^2 + {\varepsilon_{12}}^2}$$

or equivalently (4.2)

$$R_{\varepsilon} = \sqrt{\left(\varepsilon_{22} - \varepsilon_{mean}\right)^2 + {\varepsilon_{21}}^2}$$

These parameters are used to find the shear strain $\varepsilon_{12;\beta}$ at orientation $\beta = 27°$, under which failure was observed in the tests:

$$\varepsilon_{12;\beta} = R_{\varepsilon} \sin 2\beta \tag{4.3}$$

Here ε_{11} and ε_{22} are the axial strain and ε_{12} and ε_{21} are the shear strain in local $\tilde{x}$ - and $\tilde{y}$ -direction of the lattice cell respectively.

The slope and intercept parameter of the dashed failure curve in Figure 4-5 were fitted to the measurement data presented in the paper by Schulson et al. (2006): -3.548 and $0.747\left|\frac{\sigma_c}{E}\right|$ respectively, where σ_c is the critical compressive stress in unconfined (uni-axial loading) condition; ~5MPa in the tests.

The critical shear strain is the shear strain at which the Mohr diagram crosses the failure curve:

$$\varepsilon_{12;\beta} = -3.548\left(\varepsilon_{mean} + R_{\varepsilon}\cos 2\beta\right) + 0.747\left|\frac{\sigma_c}{E}\right| \tag{4.4}$$

The criterion for compressive failure is:

$$\frac{R_{\varepsilon}\sin 2\beta + 3.548\left(\varepsilon_{mean} + R_{\varepsilon}\cos 2\beta\right)}{0.747} \geq \left|\frac{\sigma_c}{E}\right| \tag{4.5}$$

Tensile failure criterion

The tests reported by Schulson et al. (2006) showed splitting under unconfined loading. Schematic sketches of the failure modes of columnar-grained ice are presented in Schulson (2001) and are linked to different places in the failure envelope. In the tensile and tensile-compression quadrants the ice fails perpendicular to the main loading direction in case of dominating tensile loading, or in-line with the main compressive direction in case of dominating compression load. The transition to Coulombic shear faulting mode where the macroscopic plane of the fault had an angle of $27^{\circ} \pm 4^{\circ}$ with respect to the main loading direction takes place around the change in loading condition from the tensile-compressive to the compressive quadrant.

Figure 4-6 provides a zoom-in of the tensile part of the failure envelope that was established for the lattice model. In line with observations, the tensile failure criterion applies to the tensile and tensile-compressive quadrant and transition to the compressive failure mode, where the orientation of the fault plane changes, takes place at the transition to the compressive quadrant.

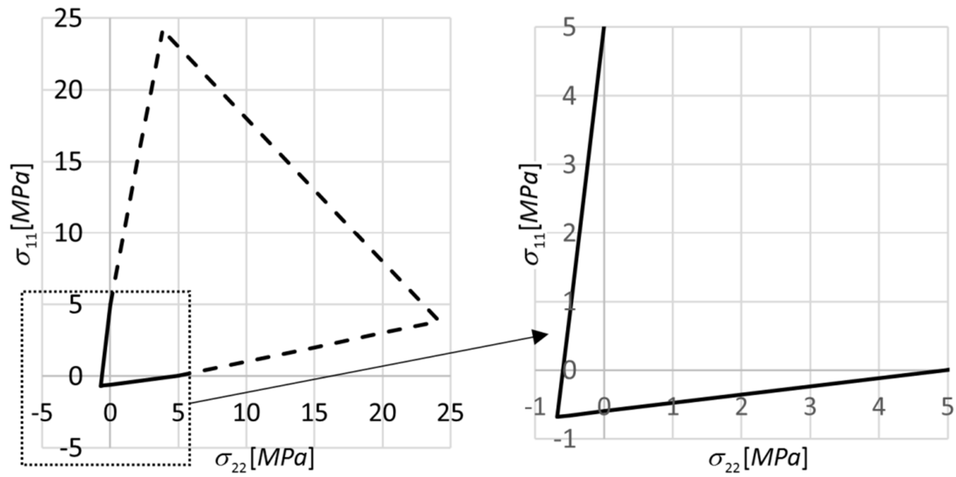

Figure 4-6: Failure envelop with a zoom-in on the tensile failure part. Tensile failure is indicated with the solid lines and compressive failure and spalling with the dashed lines.

Figure 4-4 shows Mohr diagrams for uni-axial tensile and compressive loading of magnitude of the tensile and compressive strength of the ice. Under compressive loading, depending on the amount of confinement, there are tensile strains present in the material due to the Poisson effect and part of the circle is on the positive side of the horizontal axis, which could result in a tensile failure plane perpendicular to the compressive loading direction if the strains would exceed a certain threshold. Under tensile loading conditions, the circle is for the largest part on the positive side of the horizontal axis, corresponding with a tensile failure plane in-line with the tensile loading direction, if the strains would exceed a certain threshold.

For the tensile condition, again a similar-to-Mohr-Coulomb type of failure criterion is applied in the lattice model, however now failure is set to occur if the point in the Mohr diagram in the tensile strain direction corresponding to an angle of 0° with respect to the tensile strain direction exceeds the threshold curve, indicated by the dashed lines in Figure 4-7.

The failure criterion for tensile failure is:

$$\frac{F_1\varepsilon_{mean}+R_\varepsilon}{F_2}\geq\frac{\sigma_t}{E}$$

with

$$F_1=\frac{1+\nu}{1-\nu}\frac{\frac{\sigma_c}{\sigma_t}-1}{\frac{\sigma_c}{\sigma_t}+1} \tag{4.6}$$

$$F_2=\left(1+\frac{\frac{\sigma_c}{\sigma_t}-1}{\frac{\sigma_c}{\sigma_t}+1}\right)\frac{1+\nu}{2}$$

where ε_{mean} and R_ε are the mean and radius of the Mohr circle respectively. In the previous section on compressive failure it is explained how these are derived. Factors F_1 and F_2 define the shape of the failure envelope (Figure 4-6) and depend on the ratio between the crushing strength and tensile strength and Poisson's ratio.

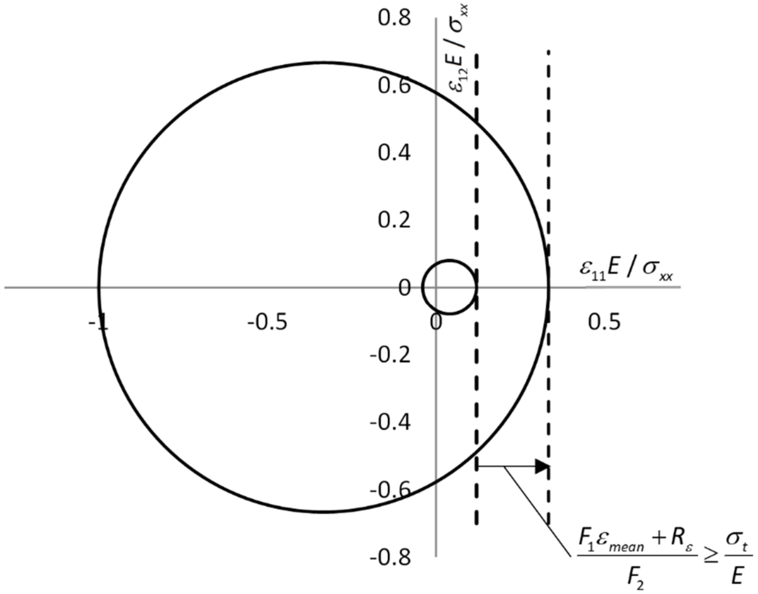

Figure 4-7: Failure occurs if the point on the Mohr diagram in the tensile direction exceeds the threshold (dashed lines). The solid lines indicate Mohr diagrams for different loading conditions: for the larger circle σ_{xx}=-5MPa and σ_{yy}=0MPa and for the smaller circle σ_{xx}=0.6MPa and σ_{yy}=0MPa. E =5MPa was used to construct this figure.

The tensile failure criterion results in the same failure mode for loading in the tensile and tensile-compressive quadrant, corresponding with observations from tests. The shape of the failure envelope is similar to that of the stress states that were measured in the winter sea ice cover on the Arctic Ocean by Richter-Menge et al. (2002) and plotted in the principal stress space by Weiss et al. (2007).

In case Poisson's ratio is set to $\frac{\sigma_t}{\sigma_c}$, which equates to $\nu = 0.12$ with the compressive and tensile strength from Schulson et al. (2006), the factors F_1 and F_2 are both 1 and the failure criterion reduces to:

$$\varepsilon_{mean} + R_\varepsilon \geq \frac{\sigma_t}{E} \tag{4.7}$$

In this case it is not necessary to assume Mohr-Coulomb like behavior to follow the failure envelope for tension. Studies of Poisson's ratio of ice are summarized by Timco and Weeks (2010). It is concluded that the Effective Poisson's ratio for sea ice is still very poorly understood and that it is influenced by many factors such as loading rate, temperature, grain size, grain structure, loading direction, state of microcracking, etc. There is no clear evidence that Poisson's ratio for ice should be $\nu = \frac{1}{3}$, which is often used in models and calculations. However, Poisson's ratio for the current study is kept to $\nu = \frac{1}{3}$, in line with other studies, as it is not proven that Poisson's ratio is linked to the failure envelope and there are no other recommended values for ice.

Spalling failure criterion

The deformations in the diagonal connections under multi-axal in-plane loading are derived in Appendix 1. When the deformations in the two diagonal connections (ε_{D1} and ε_{D2}) in the lattice cell are added-up, the total deformation depends on the applied loading, but not on the orientation of the lattice cell:

$$\left(\varepsilon_{D1} + \varepsilon_{D2}\right)\frac{E}{\sigma_{xx}} = \left(1 + \frac{\sigma_{yy}}{\sigma_{xx}}\right)(1 - \nu) \tag{4.8}$$

The deformations of the diagonal connections show opposite behaviour to the deformations of the axial connections. In case a cell is for example loaded in tension in both x- and y- direction, the tension in both directions will contribute to tensile strain in the diagonal connections of the lattice cell. The axial connections on the other hand will experience a tensile strain from the tensile loading in the direction of the connection, but will compress due to tensile loading in the opposite direction. Due to this compression, the capacity to withstand additional tensile loading increases for the axial connections. The capacity of the diagonal connections on the other hand reduces as the load in both directions contributes to strain in the same direction in the diagonal connections. In the failure envelope the behaviour of the diagonal connections results in a negative slope of the failure curve, whereas the behaviour of the axial connections gives a positive slope. This characteristic of the diagonal connections is used to derive the spalling failure criterion.

The ice tested in multi-axial compressive loading under higher confinement failed in spalling, across the columns, in through-thickness direction and cracks were created that ran roughly parallel to the plate surface. Spalling failure cannot be accurately simulated with the two-dimensional lattice model as the crack location with respect to the plate thickness is not simulated. However, a failure criterion for high confinement can be included to set a limit to the loading. The deformation in the diagonal connections in the lattice model is used here to define the failure criterion:

$$\left(\varepsilon_{D1}+\varepsilon_{D2}\right)\leq\left(1-\nu\right)\frac{\sigma_{spall}}{E}, \tag{4.9}$$

where σ_{spall} is a parameter that defines the spalling limit under highly confined compressive loading.

Failure envelope for tensile and compressive failure

By applying the failure criteria that were defined in this section (using deformation in axial connections for compressive failure under low confinement and tensile failure and deformation in the diagonal connections to define onset spalling failure under high confinement), the failure envelope in Figure 4-2 is obtained. The following critical stresses were used as input for this figure: $\sigma_c=-5$ MPa, $\sigma_t=0.6$ MPa and $\sigma_{spall}=-28$ MPa. Comparison with the failure envelope in Figure 4-1 shows that for lower confinement and tensile loading the failure envelope corresponds with measured data. For higher confinement conditions, some discrepancies are present, but the overall trends of failure under confined loading and the spalling limit are captured. A 3-dimensional model is required to simulate the spalling behaviour correctly.

4.1.2 Out-of-plane bending failure

Timco and Weeks (2010) describe the cantilever beam test and the simple beam test as the options for flexural strength analysis of ice. To find the flexural strength from these tests, it is assumed that the ice forms a homogeneous beam and deforms in a linear-elastic manner such that the failure stress is present at the outer fibre of the material. Similar to the assumptions that are made for the flexural strength measurements, the lattice model behaves linear-elastically prior to failure. It is assumed that the highest bending strains are present at the outer fibre of the material and that both compressive and tensile failure can occur at these locations, like in the in-plane failure modes. Strains from both upward and downward bending conditions are considered.

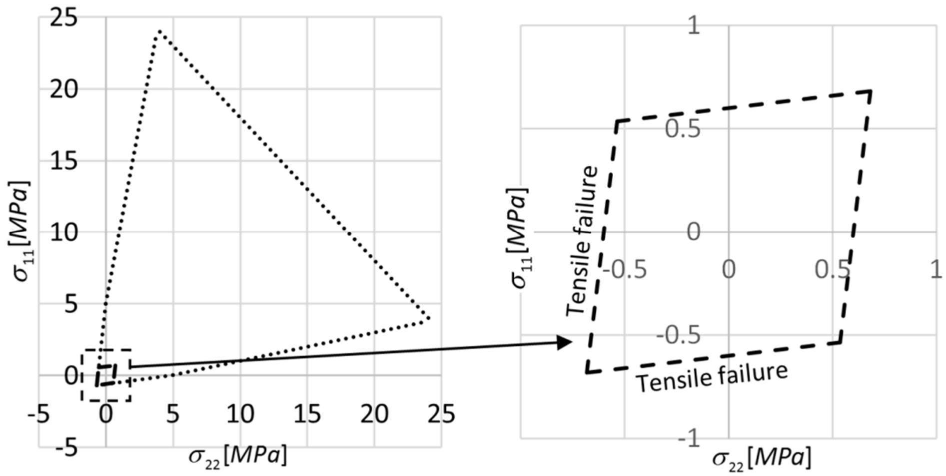

Figure 4-8: The failure envelope for bending (right) and its relation to the failure envelope for in-plane loading conditions (left). To construct this Figure, it was assumed that tensile and flexural strength as well as compressive strength and strength in bending-induced compression have the same value.

The failure envelope for bending that is constructed is presented in Figure 4-8, where it is compared to the failure envelope for in-plane loading. Bending contributes to strains at both top and bottom of the ice sheet and therefore the failure envelope is symmetrical about the line $\sigma_{11} = -\sigma_{22}$. Similar to the case of in-plane tensile failure, for bending failure a failure criterion for the axial springs is derived. No appropriate test data for multi-axial bending failure was found, and therefore the shape of the failure envelope was based on the failure envelope for in-plane deformation. In the next section, it is shown how the in-plane and out-of-plane failure criteria can be combined and how the difference between tensile and flexural strength can be captured.

Tensile failure due to bending

Figure 4-9 shows a plate with an internal lattice cell, which has orientation α with respect to the x- axis. The plate has free boundaries and is loaded in out-of-plane bending, by moment per unit length m_{xx} in x-direction and m_{yy} in y-direction. Appendix 3 explains how the bending and torsional deformations of the connections in the lattice cell under these loading conditions are calculated for varying angle α. The bending and torsional rotation in the lattice cell are normalised with the cell size and multiplied by half the plate thickness, to find the strain at the outer material fibre.

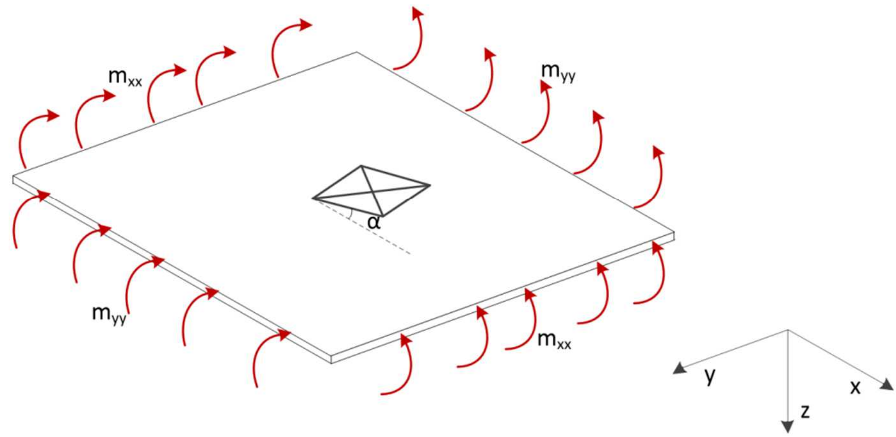

Figure 4-9: Plate loaded in multi-axial shear and bending with internal lattice cell oriented with rotation α relative to the x-axis

Figure 4-10 presents Mohr diagrams for the axial strain in the rotational spring η_{11} versus strain in the torsional spring η_{12}, multiplied by $\frac{h}{2}$ to find the strain at the outer fibre of the material and multiplied by Young's modulus over load ratio, for varying orientation of the lattice cell from 0 to 180° and varying 'confinement' (relative magnitude of $\sigma_{yy;bending}$ compared to $\sigma_{xx;bending}$). The bending stress is given by $\sigma_{xx;bending} = \frac{6m_{xx}}{h^2}$ and $\sigma_{yy;bending} = \frac{6m_{yy}}{h^2}$. Poisson's ratio of $\frac{1}{3}$ was selected as a representative value for sea ice.

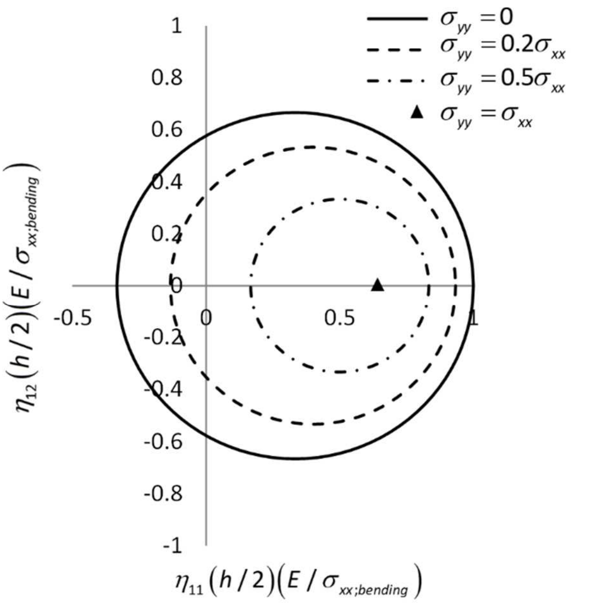

Figure 4-10: Mohr diagram for normal and torsional bending of the axial connections for multi-axial loading conditions on the tensioned side of the plate

The Mohr diagram for bending, Figure 4-10, corresponds very well to the diagram for in-plane loading, Figure 4-4, only it is mirrored about the vertical axis as the bending diagram is shown for the tensioned side of the plate. The failure criterion for bending can be derived in a similar manner to the failure criterion for tension in in-plane loading conditions. In addition, it allows to combine in-plane and bending failure into one failure criterion, which is further explained in section 3.3.

The mean η_{mean} and radius R_η of the Mohr circle for the stress state associated with bending deformations are determined by:

$$\eta_{mean;top} = -\frac{\eta_{11} + \eta_{22}}{2}\frac{h}{2} \tag{4.10}$$

$$R_{\eta;top} = \sqrt{\left(-\eta_{11}\frac{h}{2} - \eta_{mean;top}\right)^2 + \left(-\eta_{12}\frac{h}{2}\right)^2} \tag{4.11}$$

for the top of the ice plate and

$$\eta_{mean;bottom} = \frac{\eta_{11} + \eta_{22}}{2}\frac{h}{2} \tag{4.12}$$

$$R_{\eta;bottom} = \sqrt{\left(\eta_{11}\frac{h}{2} - \eta_{mean;bottom}\right)^2 + \left(\eta_{12}\frac{h}{2}\right)^2} \tag{4.13}$$

for the bottom of the ice plate.

The failure criterion for bending follows by substituting η_{mean} and radius R_η for top and bottom of the plate, multiplied by $\frac{h}{2}$ for ε_{mean} and R_ε as well as substituting flexural strength σ_f for tensile strength σ_t in equation (4.6):

$$\frac{F_1\eta_{mean}\frac{h}{2} + R_\eta\frac{h}{2}}{F_2} \geq \frac{\sigma_f}{E} \tag{4.14}$$

The failure envelope for bending failure in the lattice is presented in Figure 4-8. The following critical stresses were used as input for this figure: $\sigma_f = 0.6$ MPa and $\sigma_{crit;bending} = 5$ MPa.

Separate upward and downward failure criteria

A separate criterion for positive and negative bending could be included to account for differences in upward and downward bending that could be caused by inhomogeneous material properties of the ice over the thickness. In that case the failure criterion would be:

$$\frac{F_1\eta_{mean;bottom}\frac{h}{2}+R_{\eta;bottom}\frac{h}{2}}{F_2}\geq\frac{\sigma_{f;upward}}{E} \tag{4.15}$$

for upward bending and

$$\frac{F_1\eta_{mean;top}\frac{h}{2}+R_{\eta;top}\frac{h}{2}}{F_2}\geq\frac{\sigma_{f;downward}}{E} \tag{4.16}$$

for downward bending, where $\sigma_{f,downward}$ and $\sigma_{f,upward}$ are the flexural strength in downward and upward bending respectively.

4.1.3 Combined bending and tensile deformations

In this section, it is discussed that linear-elastic, homogeneous properties are a simplistic assumption for sea ice. In measurements of engineering properties of sea ice, a distinction is made between tensile and flexural strength. For combined bending and tensile loading conditions, the failure criteria that were derived for bending and tension are combined into a single criterion that accounts for both deformations. The bending deformation is hereto scaled with the ratio between flexural and tensile strength of the ice.

A description of typical first year sea ice by Palmer and Croasdale (2013) is summarised here. Sea ice has a complex structure, which is dependent on its history, temperature and influence of salt. Snow often, but not always, forms a top layer. Below the snow sits a layer of ice that formed first, consisting of small and randomly oriented grains. Below that layer, the ice consists of columnar grains, which are elongated vertically, and are much larger than those closer to the surface. Vertical brine channels and pockets are present between the columnar grains, some of which connect the pocket to the sea beneath, leading brine to drain out.

Timco and Weeks (2010) describe columnar and granular ice and differences in first-year and multi-year ice. Granular ice is usually isotropic. Columnar ice comes in two varieties. In one, the ice properties in the horizontal plane are independent of direction. In the other, properties measured parallel to and perpendicular to the alignment direction can be quite different and reflect the mean current direction beneath the ice. There are differences between first year ice and multi-year ice which survived a summer melt season. In contrast to first-year ice, multi-year ice usually has a very low salinity. As such, there is little porosity in the ice and it is considerably stronger than first-year sea ice.

The structure of sea ice is complex, consists of different layers and the parameters depend on the age, and influences of brine channels. The different micro-structures within the ice have different stiffness and strength, which is further affected by the presence of brine drainage channels. As such, it is simplistic to assume ice as a linear-elastic, homogeneous material.

Measurements of engineering properties of ice usually combine the behaviour of the different layers and structures in the ice in stiffness and strength parameters of the ice sheet. Tensile strength and bending strength parameters are not necessarily the same for the same ice sheet and are measured with different methods. To be able to account for these engineering properties, this section shows how different values for tensile and bending strength can be incorporated in the lattice model.

Tensile failure due to in-plane loading and out-of-plane bending is combined by evaluating the mean strains at the top and bottom of the plate, $\varepsilon_{mean;top}$ and $\varepsilon_{mean;bottom}$:

$$\varepsilon_{mean;top} = -\frac{\eta_{11}+\eta_{22}}{2}\frac{h}{2}\frac{\sigma_t}{\sigma_f}+\frac{\varepsilon_{11}+\varepsilon_{22}}{2} \tag{4.17}$$

$$\varepsilon_{mean;bottom} = \frac{\eta_{11}+\eta_{22}}{2}\frac{h}{2}\frac{\sigma_t}{\sigma_f}+\frac{\varepsilon_{11}+\varepsilon_{22}}{2} \tag{4.18}$$

as well as the radius of the Mohr diagram at the top and bottom of the plate, $R_{\varepsilon;top}$ and $R_{\varepsilon;bottom}$:

$$R_{\varepsilon;top} = \sqrt{\left(-\eta_{11}\frac{h}{2}\frac{\sigma_t}{\sigma_f}+\varepsilon_{11}-\varepsilon_{mean;top}\right)^2+\left(-\eta_{12}\frac{h}{2}\frac{\sigma_t}{\sigma_f}+\varepsilon_{12}\right)^2} \tag{4.19}$$

$$R_{\varepsilon;bottom} = \sqrt{\left(\eta_{11}\frac{h}{2}\frac{\sigma_t}{\sigma_f}+\varepsilon_{11}-\varepsilon_{mean;bottom}\right)^2+\left(\eta_{12}\frac{h}{2}\frac{\sigma_t}{\sigma_f}+\varepsilon_{12}\right)^2} \tag{4.20}$$

The failure criteria for combined axial and bending deformation in tensile mode is now found by substituting $\varepsilon_{mean;top}$ and $R_{\varepsilon;top}$ or $\varepsilon_{mean;bottom}$ and $R_{\varepsilon;bottom}$ for ε_{mean} and R_{ε} in equation (4.6).

In case of dominating in-plane compression, failure may take place due to a combination of in-plane compression and bending induced compression. The failure criteria for combined axial and bending deformation in compression mode for this condition are found by substituting $\varepsilon_{mean;top}$ and $R_{\varepsilon;top}$ or $\varepsilon_{mean;bottom}$ and $R_{\varepsilon;bottom}$ for ε_{mean} and R_{ε} in equation (4.5).

4.2 Failure criteria at discontinuities

Near a crack-tip or other discontinuities in a material, stresses and strains concentrate and the failure criteria derived in the previous section do not correctly predict failure at these locations. In this Chapter, the mesh dependency of strain concentrations in the lattice model is studied, using data from splitting and bending tests. Failure criteria with minimal dependence on cell size are derived for splitting and bending of a discontinuous plate, which replace the tensile failure criterion for cells next to a crack-tip.

4.2.1 Tensile strain concentrations – Splitting

Splitting of brittle materials is analysed using Linear Elastic Fracture Mechanics (LEFM) theory, developed by Griffith (1921). LEFM is applicable if non-linear material deformation is limited to a region around the crack tip that is small relative to the crack length. For ice plate sizes of engineering interest splitting can be accurately described with LEFM (Lu et al., 2015b). Near the melting temperature creep has significant influence on ice behaviour and LEFM is no longer applicable (Mulmule and Dempsey, 1999). In case there is significant plastic deformation at the crack tip, application of LEFM would under-predict the strength of the ice, which could lead to non-conservative ice loading when applied in engineering solutions. Mulmule & Dempsey (2000) provide size requirements for ice specimen for which LEFM is applicable. Ice dimensions for ice-structure interaction are large and it is assumed that the strongest ice, giving governing loads, has temperatures lower than the melting-point and therefore LEFM can be applied.

A typical problem in fracture mechanics of ice is that of an edge-cracked elastic square plate with a crack of length a loaded with force F at the crack mouth, as shown in Figure 4-11. Field tests for an edge-cracked ice plate have been described in Adamson and Dempsey

(1998) and Lu et al. (2015a). Using the method derived by Westergaard (1939), the normal stress near the crack tip, is given by:

$$\sigma_n = \frac{K_I}{\sqrt{2\pi r}} \tag{4.21}$$

where σ_n is the normal stress at distance r from the crack tip and K_I is the stress intensity factor of the opening mode (see for example Anderson (1991)).

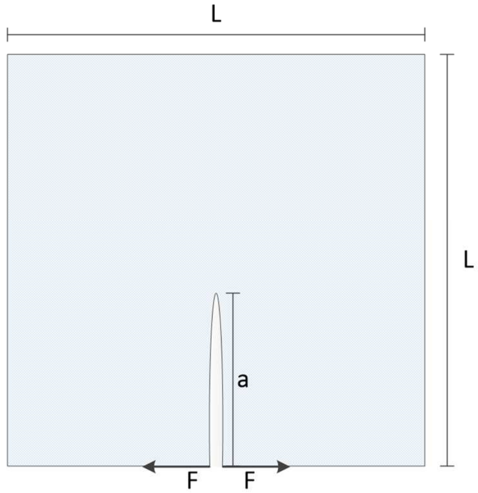

Figure 4-11: Edge-cracked elastic square plate loaded at the crack mouth

This problem was analysed by Potyondy and Cundall (2004) with a bonded-particle model for rock and is studied with the lattice model in a similar manner. The lattice cells are presented in Figure 4-12. A failure criterion for the axial connections in the first cell in front of the crack tip is derived in this section. Deformations in the connections of the lattice cell represent average deformations that occur at the location of that lattice cell. The representative normal stress $\sigma_{n;d}$ in the first cell is found by integrating the normal stress over the length of the lattice cell and dividing by this length:

$$\sigma_{n;d} = \frac{1}{d}\int_0^d \frac{K_I}{\sqrt{2\pi}}\frac{1}{\sqrt{r}}dr = \frac{\sqrt{2}K_I}{\sqrt{\pi d}} \tag{4.22}$$

For a uniform load, the failure criterion for in-plane tensile deformation is derived in the previous section, equation (4.6). Substituting $\sigma_{n;d}$ for σ_t gives the failure criterion for the lattice cell near the cracktip:

$$\frac{F_1\varepsilon_{mean}+R_\varepsilon}{F_2}\geq\frac{\sqrt{2}K_{IC}}{\sqrt{\pi d}}\frac{1}{E} \tag{4.23}$$

where K_{IC} is the critical stress concentration factor that determines whether a crack propagates or not, which can be obtained from measurements.

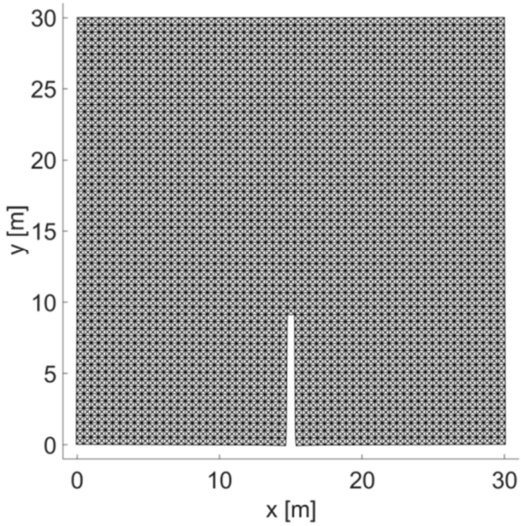

Figure 4-12: **Splitting test with the lattice model of 60x60 nodes. a/L=0.3**

For these loading conditions, the deformation of connection 1-2 as indicated in Appendix 2, is not the same as that of connection 3-4 and the same holds for connection 1-3 and 2-4. ε_{mean} is calculated by averaging the axial strain in all axial connections in the lattice cell:

$$\varepsilon_{mean}=\frac{\varepsilon_{11,1-2}+\varepsilon_{22,1-3}+\varepsilon_{11,3-4}+\varepsilon_{22,2-4}}{4} \tag{4.24}$$

Radius R_ε is the average radius from the deformations of the axial connections in the lattice cell:

$$R_\varepsilon = \left(\begin{array}{l} \sqrt{\left(\varepsilon_{11,1-2} - \varepsilon_{mean}\right)^2 + \varepsilon_{12,1-2}{}^2} + \sqrt{\left(\varepsilon_{11,3-4} - \varepsilon_{mean}\right)^2 + \varepsilon_{12,3-4}{}^2} \\ + \sqrt{\left(\varepsilon_{22,1-3} - \varepsilon_{mean}\right)^2 + \varepsilon_{21,1-3}{}^2} + \sqrt{\left(\varepsilon_{22,2-4} - \varepsilon_{mean}\right)^2 + \varepsilon_{21,2-4}{}^2} \end{array} \right) / 4 \tag{4.25}$$

In these equations the subscripts 1-2, 3-4, 1-3 and 2-4 indicate the connection for which the strain is calculated when using equations (A.2.13) to (A.2.16). For bending, which is discussed in the next section, mean and radius of the Mohr diagram are evaluated by averaging over the different connections in a similar manner.

Validation

To confirm the applicability of the splitting criterion, comparison is made to analytical prediction of crack propagation. Dempsey et al. (1995) derived weight functions for finite edge cracked geometries. Parameters for a square plate are provided in Mulmule & Dempsey (1998). The applied load on the edge cracked plate is normalized using the stress intensity factor, plate thickness and length, giving the normalised load $\tilde{F}$:

$$\tilde{F} = \frac{F}{tK_I\sqrt{L}} \tag{4.26}$$

The analytical normalised load for different initial crack lengths is compared to results obtained with the lattice model in Figure 4-13. A ratio of $\frac{\sigma_c}{\sigma_t} = 5$ was applied. For $a / L > 0.3$ the results obtained with the lattice model compare well with those obtained analytically. For smaller crack length, the solution obtained with the lattice model deviates slightly from the analytical solution, especially for very short crack lengths. The width of the crack is assumed equal to one cell size and this could cause the differences, which are larger for a larger cell size. The relative crack length for which unstable crack propagation occurs (the top of the curve) is predicted well with the lattice model, for both cell sizes.

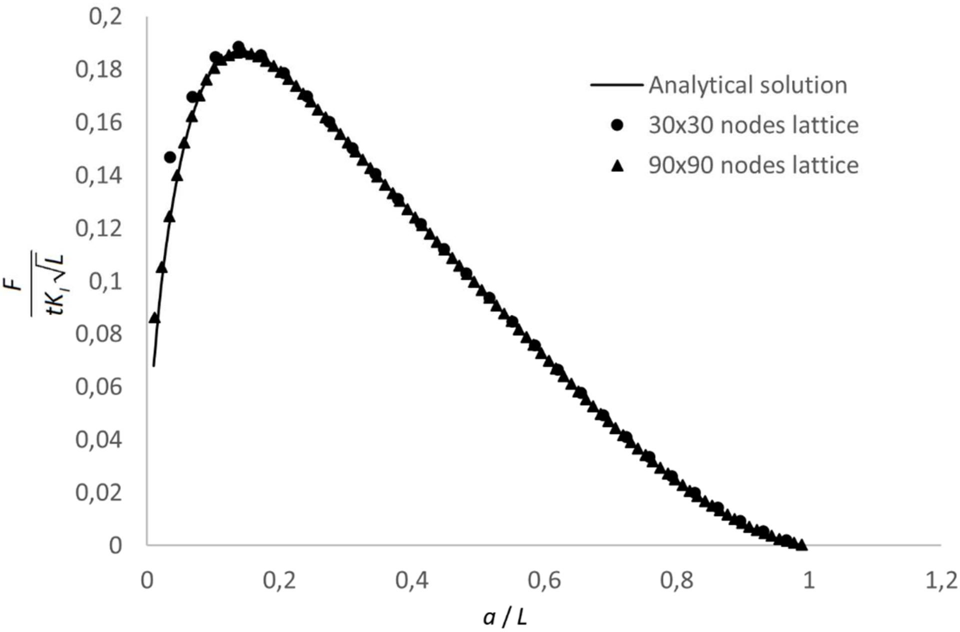

Figure 4-13: Analytical normalised load for different initial crack length of the edge-cracked plate that was obtained using the weight functions from Dempsey et al. (1995) and parameters from Appendix 1 of Mulmule and Dempsey (1998) , compared to results obtained with the lattice model

Full scale test simulation

As an example, an ice splitting test that was executed by Dempsey et al. (1999) at Resolute, N.W.T. in April/May 1993, is simulated with the lattice model. In the testing campaign, square plate specimens with dimensions of 0.5mx0.5m to 80mx80m were cut out of the ice and an initial crack was made in the plate from the midpoint of a side towards the centre of the plate. A hydraulic flatjack was used to apply a load at the crack mouth. Displacement of the crack mouth and the original crack tip were registered. A schematic drawing of the test set-up is presented in Adamson & Dempsey (1998). A test with a relatively large specimen size of 30x30m was selected to simulate with the lattice model as the larger dimensions are representative for ice-structure interaction on full scale and crack opening displacement versus flatjack pressure was reported in detail for this test in Mulmule & Dempsey (1999). An overview of the ice properties that were used to simulate the test with the lattice model are presented in Table 4-1. A schematic overview of the structure of the 60x60 nodes lattice model during the splitting test is presented in Figure 4-12.

Table 4-1: Parameters used to simulate ice splitting test with the lattice model

Parameter	Symbol	Quantity	Unit
Plate dimensions	L_x x L_y	30 x 30	m
Ice thickness	t	1.8	m
Initial crack length	a	9	m
Loading rate	dF/dt	303	N/s
Young's modulus ice	E	8.7	GPa
Poisson's ratio	v	0.33	-
Critical stress intensity factor	K_{IC}	238	kPa√m

For one of the 30x30m test specimen, crack initiation occurred at approximately 1000 s, followed by a period of stick-slip stable crack growth. Unstable fracture occurred at 1350s. This behaviour was seen for only one of the 30m specimens tested; the other ones failed by unstable crack growth after crack initiation (Mulmule and Dempsey, 1999).

For all simulations in this thesis an adaptive double precision ordinary differential equation solver for Fortran, DVODE_F90, was used, with a specified relative tolerance criterion of 10^{-8} and an absolute error tolerance of 10^{-10}. Therefore, the timestep was not continuous over the simulations, up to the moment of failure. Upon failure, the timestep was manually defined as it was found the solver did not adapt appropriately to simulate the crack propagation. A small timestep compared to the duration of the interaction process was selected and it was confirmed by variation of the timestep that there was a negligible influence of the timestep on the results. The lattice cells in the system are only connected to their direct neighbours, resulting in a sparse stiffness matrix, which was specified in the solver settings. Once the failure criterion in one of the lattice cells was met, this cell was removed by setting the stiffness of the diagonal connections to zero and by removing half of the original stiffness of the axial connections. Upon removal of the cell, the next time step was started assuming that the positions and velocities of the particles are continuous functions of time. The time step was not refined around the moment of failure as it would elongate the computations significantly. This approach introduces an error at every failure event as the exact moment of failure is not captured. It was found, however, that the crack pattern was repetitive for different values of timestep and tolerance. Based on this observation it was concluded that the adopted procedure is acceptable. A timestep of $3.8 \cdot 10^{-4}$ s was applied for the simulation of this splitting test during crack propagation. A hydrodynamic damping coefficient of $0.1\sqrt{k_s \rho h}$ was applied as well as a material damping coefficient of 10^{-3}. Effects of material damping and hydrodynamic damping of the applied magnitude on the results of the simulations are very small. Damping is further discussed in Chapter 3.

Results from the tests with the lattice model are presented in Figure 4-14. Crack Mouth Opening Displacement (CMOD), Crack Opening Displacement (COD) in the middle of the crack and Crack Tip Opening Displacement (CTOD) are plotted against loading time. The crack initiation occurred at 1186s and unstable crack growth followed, which can be seen by the slope change to almost vertical in the graph. This is in line with expectations; in Figure 4-13 the a/L-ratio of 0.3 results in unstable crack propagation as this point is beyond the peak of the graph. CMOD at crack initiation was 1250µm in the test and 722µm in the simulation with the lattice model. CTOD was 35 µm in the test and 19µm in the simulation with the lattice model. A Modulus of 8.7GPa was computed by Dempsey et al. (1999), from the CMOD and used in the simulation. Application of a lower Modulus (5GPa) would result in displacements close to the measured displacements (1255µm for CMOD and 33 µm for CTOD). This is in line with typical values for the Effective Modulus of ice, which are often ranging between 1 and 5 GPa (Timco and Weeks, 2010). Changing the modulus does not affect the time of crack initiation.

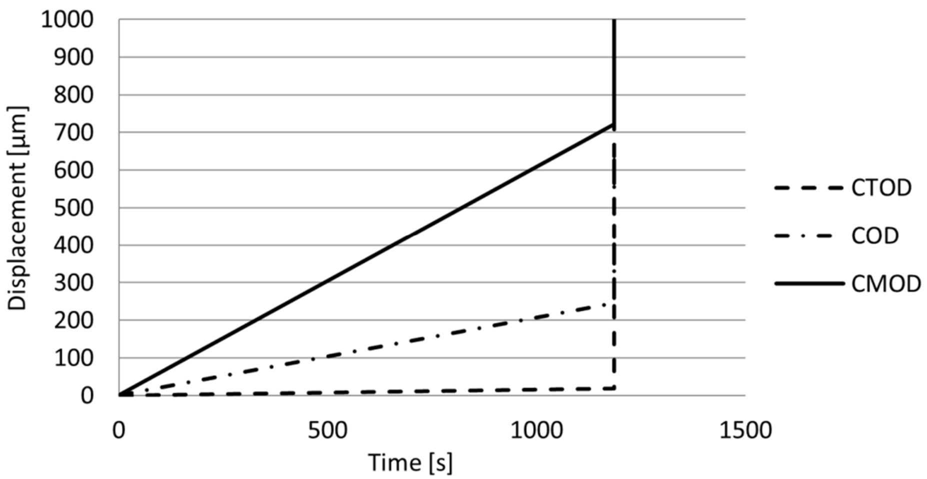

Figure 4-14; Crack Mouth Opening Displacement (CMOD), Crack Opening Displacement (COD) in the middle of the crack and Crack Tip Opening Displacement (CTOD) from the simulation with the lattice model

This example shows that the time of onset of crack propagation can be approximated with the lattice model, when applying the failure criteria for splitting. In the field, inhomogeneities are present in the ice, resulting in discrepancies with numerical simulations, such as the period of stick-slip stable crack growth in this example.

When a crack propagates in the lattice, an entire cell is assumed to break out near the tip of a crack, lengthening the crack with the cell length. Therefore the length of the cell was chosen to average the deformation. The crack path studied in this section follows a straight line through the lattice cells. The failure criterion that is derived for splitting conditions, determines based on local deformations of the cell and the cell size whether or not the cell will fail and therefore whether or not the crack will propagate and in which direction. The stress distribution near the crack tip and with that the local load distribution over the lattice cells is determined by the overall loading condition and crack shape. Strains in the lattice cells in multiple directions are considered to determine the onset of failure, by making use of the Mohr diagram. The effects of orientation of the cell relative to the crack propagation direction are therefore considered small.

4.2.2 Bending strain concentrations – Flexural strength test

Flexural strength is an important parameter for determining ice loading on sloping structures as fracture due to bending is often a governing failure mode. As described in the international standard for Arctic offshore structures engineering ISO19906 (ISO, 2010), the flexural strength of ice is either estimated by an in situ beam test or derived from measurements of the physical properties temperature and salinity which in turn give the brine volume of the ice. Timco and Weeks (2010) describe the cantilever beam test and the simple beam test as the options for flexural strength analysis.

Figure 4-15 shows an in-situ cantilever beam test. Two long sides and one short side of a beam are cut free from the ice and one short side is left attached. A load of increasing magnitude is applied at the free end until the beam fails. The failure load and often also displacement is recorded. For further information, a standardized testing method for in-situ cantilever beam tests is described by Schwarz et al. (1981). Stress concentrations can be prevented by drilling stress relief holes near the beam root (Frederking and Svec, 1985). To study strain concentrations in bending, a flexural strength test is simulated with the lattice model in this section and the concentration of strains near the beam root is analysed. In the numerical simulation, no stress relief holes are applied.

Karulina et al. (2013) describe cantilever beam tests that were executed at Van Mijen Fjord. Ice parameters obtained from these tests are used as a basis for simulation of the flexural strength tests with the lattice model. Parameters used are presented in Table 4-2.

Figure 4-15: Students perform an in-situ beam test in Svalbard to measure the flexural strength of the ice (Photo: T.S. Nord)

Table 4-2: Parameters used to simulate with the lattice model tests executed by Karulina et al. (2013)

Parameter	Symbol	Quantity	Unit
Ice thickness	h	0.39	m
Beam length	L_b	2.30	m
Beam width	w	0.46	m
Salinity ice	S	2.7	ppt
Flexural strength ice	σ_f	0.186	MPa
Loading rate	F’	236	N/s
Temperature ice	T	-1.6	°C
Young’s modulus ice	E	1.3	GPa
Poisson’s ratio	ν	0.33	-
Ice density	P_{ice}	920	kg/m^3
Sea water density	ρ_{wat}	1025	kg/m^3
Compressive strength ice	σ_c	5 σ_f	MPa

To estimate the Young's modulus of the ice, a similar process is used as described in the paper by Karulina et al. (2013). First the brine volume is determined from the salinity and temperature of the ice using the Frankenstein and Garner (1967) equation: $v_b\left[ppt\right] = S\left(\frac{49.185}{|T|}+0.532\right)$, -22.9<T<-0.5°C. Then the Young's modulus is determined using the Vaudrey (1977) equation, which is based on beam tests executed in Antarctica and Alaska in the 1970ies: $E\left[MPa\right] = 5.316 - 0.436\sqrt{v_b}$. Because Poisson ratio, ice density and seawater density were not measured, typical values were used for these parameters and a ratio of $\frac{\sigma_c}{\sigma_t} = 5$ was applied.

A plate of finite size, 4.6x4.6m was modelled and clamped at the edges to simulate support of a large ice plate. Figure 4-16 shows the deformed shape of the beam, as simulated with the lattice model of different mesh size. The horizontal dimensions x and y and vertical deflection w are not plotted on the same scale. The global deformed shape of the beam is the same for all mesh sizes. The deflection of the beam tip is 2.0 mm.

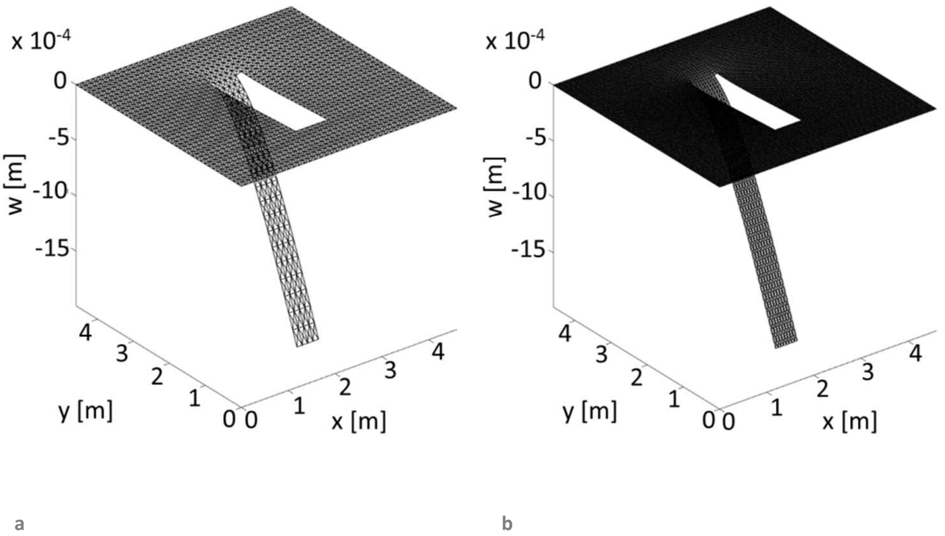

Figure 4-16: Deformed shape of the ice during the flexural strength test, simulated with the lattice model of a) 5x21 nodes beam and b) 9x41 nodes beam cut out. Horizontal x- and y- and vertical w dimensions are shown on different scales.

Locally there are differences in the results obtained with different mesh sizes. Deformations near the beam root are relatively large; comparable with stress concentrations near the crack tip in the splitting test of the previous section. For the beam test it is often assumed that the bending stress at the beam root at the moment of failure can be determined based on the stress at the root of a clamped beam:

$$\sigma_{f;beam} = \frac{6F_c L_b}{wh^2} \tag{4.27}$$

where F_c is the failure load, L_b is the length of the beam w is the width of the beam and h the thickness. Like for the un-cracked plate in bending in section 4.1.2, the deformation of the axial connections is multiplied by plate thickness to find equivalent strain in the outer fibre of the material.

The failure criterion for bending that was derived in section 4.1.2 is repeated here:

$$\frac{F_1 \eta_{mean} \frac{h}{2} + R_\eta \frac{h}{2}}{F_2} \geq \frac{\sigma_f}{E} \tag{4.28}$$

Substituting $\sigma_{f;beam}$ for σ_f and bringing all variables to the left-hand side of the equation gives:

$$\frac{F_1 \eta_{mean} \frac{h}{2} + R_\eta \frac{h}{2}}{F_2} \frac{Ewh^2}{6F_c L_b} \geq 1 \tag{4.29}$$

Figure 4-17 shows the left-hand side of equation (4.29) for different location x, normalised by half the beam width, along the root of the beam (i.e. the first row of lattice cells on the beam near the connection to the rest of the plate), for different cell sizes of the beam in the lattice plate. The deformation in the axial springs near the edge of the beam follows the curve defined by the following equation:

$$\frac{F_1 \eta_{mean} \frac{h}{2} + R_\eta \frac{h}{2}}{F_2} \frac{Ewh^2}{6F_c L_b} = \frac{1}{2} \left(\frac{1}{\sqrt{1 - \frac{2x}{w}}} + \frac{1}{\sqrt{1 + \frac{2x}{w}}} \right) f \tag{4.30}$$

where f is a factor that depends on the shape and size of the beam.

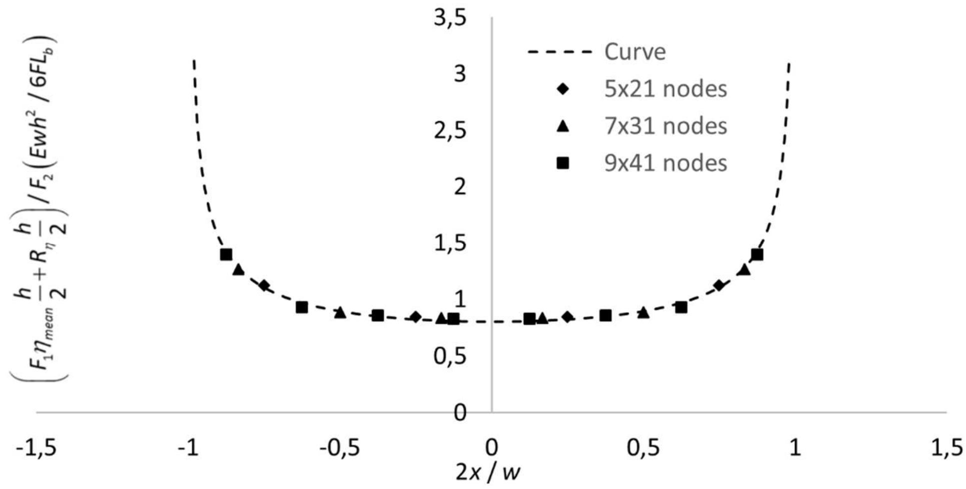

Figure 4-17: Scaled deformation of the axial connections along the root of the bending beam, at location x from the centre of the root, for various cell sizes.

The highest strain is located near the edge of the beam root, where the centre of the lattice cell is located at $x = \frac{w-d}{2}$. Substituting this in equation (4.30) gives the failure criterion:

$$\frac{F_1 \eta_{mean} \frac{h}{2} + R_\eta \frac{h}{2}}{F_2} \geq \frac{6FL_b}{Ewh^2} \frac{1}{2} \left(\frac{1}{\sqrt{\frac{d}{w}}} + \frac{1}{\sqrt{2 - \frac{d}{w}}} \right) f \tag{4.31}$$

The failure predicted with this criterion shows minimal dependence on the mesh size, for the mesh sizes studied in the example. These are the mesh sizes that would typically be applied to define the failure criterion in bending conditions with strain concentrations. A smaller mesh size of three nodes (two cells) over the beam width would not follow the curve as deformations in the centre of the beam root and deformations near the corners would be captured with the same cells. Much larger mesh sizes are considered not to be practical for the simulation that is intended with the results, as it is not expected that the cell size selected for an analysis is much smaller than 1/8th of the width of the beam-test that is used to define the onset of failure.

The sensitivity of factor f to the beam dimensions is studied to show which parameters are of influence to its value and how significant their influence is and results are presented in Table 4-3. Factor f depends on the width and the height of the beam and approaches

0.9 for large thickness or small width; conditions in which 2D effects disappear and the behaviour is approximated well by the beam model.

Table 4-3: Sensitivity study of factor f

L (m)	h (m)	E (GPa)	W (m)	Case	f
2.3	0.39	1.3	0.46	Base case	0.80
3.45	0.39	1.3	0.46	1.5 x original length, to fall within recommendation of 7-10xh by Schwarz et al., (1981)	0.80
2.3	0.78	1.3	0.46	2 x original thickness	0.84
2.3	0.39	2.6	0.46	2x original Youngs Modulus	0.80
2.3	0.39	1.3	0.23	0.5x original width	0.88

Deriving the failure criterion based on full scale test simulation

In 1977, a series of cantilever beam tests without stress relief holes were carried out in Isfjorden, Spitsbergen (Frederking and Häusler, 1978). Parameters of one of the tests are presented in Table 4-4. The test is simulated with the lattice model and at the time of failure it is found that $\eta_{mean} = 5.73 \cdot 10^{-4}$ and $R_{\eta} = 3.11 \cdot 10^{-4}$ m^{-1} near the beam root. Substituting this and the parameters from Table 4-4 in equation (4.31) gives $f = 0.8$. The failure criterion near the crack tip, for cell size d becomes:

$$\frac{F_1 \eta_{mean} \dfrac{0.44}{2} + R_{\eta} \dfrac{0.44}{2}}{F_2} \geq \frac{6 \cdot 1900 \cdot 4.04}{2.3 \cdot 10^9 \cdot 0.67 \cdot 0.44^2} \frac{1}{2} \left(\frac{1}{\sqrt{\dfrac{d}{0.67}}} + \frac{1}{\sqrt{2 - \dfrac{d}{0.67}}} \right) 0.8$$

with

$$F_1 = \frac{1 + \dfrac{1}{3}}{1 - \dfrac{1}{3}} \frac{5-1}{5+1} \tag{4.32}$$

$$F_2 = \left(1 + \frac{5-1}{5+1} \right) \frac{1 + \dfrac{1}{3}}{2}$$

The time versus deflection curves at three locations w1 at 3.8m from the beam root, w2 at 2.0m from the beam root and w3 at 0.1m from the beam root are presented in Figure 4-18. The force applied in the lattice model was a linearly increasing function of time and continued to build-up upon failure. A timestep of $1.9 \cdot 10^{-7}$ s was used for the simulation, during crack propagation. The deflections at the time of failure (0.7s) are of the same order of magnitude as the field measurements: 4.7mm at location w1 (~5mm in the field test), 1.9mm at location w2 (~2mm in the field test) and 0.18mm at location at location w3 (~0.1mm in the field test). After failure, the beam tip and centre moved downward, while the point near the root of the beam moved upward, showing as negative deflection in the plot for the lattice model. Deflection change after failure is more gradual than in the splitting test as the movement is resisted by the buoyant force of the water, which is simulated with a Kelvin foundation.

This example shows how an in-situ beam test where no stress relief holes were drilled can be used to define the failure criterion for bending near a crack tip.

Table 4-4: Parameters used to simulate with the lattice model tests executed by (Frederking and Häusler, 1978)

Parameter	**Symbol**	**Quantity**	**Unit**
Ice thickness	h	0.44	m
Beam length	L_b	4.04	m
Beam width	w	0.67	m
Failure load	F	1900	N
Loading rate	F’	2714	N/s
Young’s modulus ice	E	2.3	GPa
Poisson’s ratio	v	0.33	-
Ice density	P_{ice}	920	kg/m^3
Sea water density	ρ_{wat}	1025	kg/m^3
Compressive strength ice	σ_c	5 σ_f	MPa

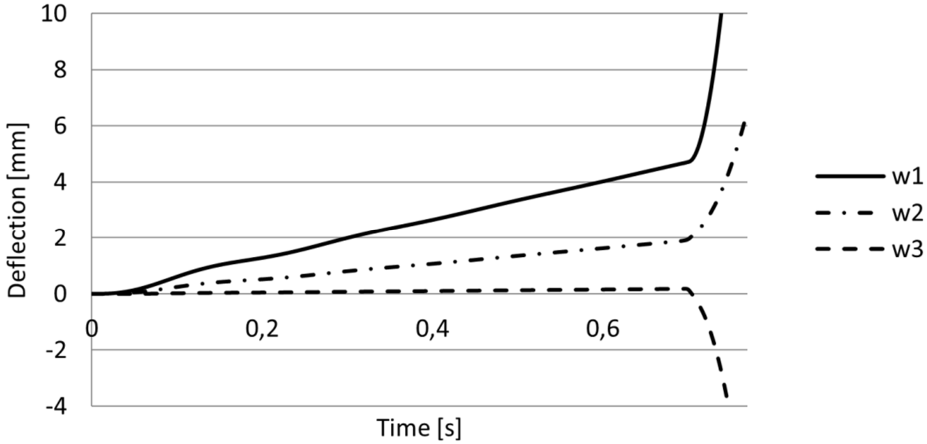

Figure 4-18: Deflection of three points along the beam during the simulation with the lattice model: w1 near the tip, w2 in the center and w3 near the root of the beam

4.3 Conclusions

Failure criteria have been developed and discussed for a numerical plate model of sea ice that account for failure in multi-directional tension, compression, bending and splitting at the same time and are linked to ice property measurements taken in the field. The failure criteria are implemented into a single model, making an important step forward in development of numerical models that enable physically sound simulation of failure processes that occur in ice-structure interaction.

In ice plate failure tests described in literature, different loading conditions resulted in different failure modes: splitting under unconfined loading, Coulombic shear friction under lower confinement and spalling under higher confinement. Mohr-Coulomb type failure criteria are derived, in which tensile, compressive and in-plane shear deformation of the connections of the lattice are used to find the strain state of the lattice cell. The radius of the Mohr diagram for axial and shear strain in the connections reduces with increasing confinement. This characteristic is used to capture the increasing capacity of the plate with increasing confinement in multi-axial compressive and tensile loading. The splitting and Coulombic shear friction failure modes are captured by linking the criterion for onset of failure to the corresponding fault orientation observed in tests. Similarly, a criterion is derived for tensile conditions that may occur at the outer fibre of the ice plate, near the surfaces, due to tension induced by bending and torsion. Deformation due to in-plane tension and out-of-plane bending can be added-up and applied in a single failure criterion while accounting for differences in tensile and flexural strength as well as potential differences in flexural strength in upward and downward bending.

The deformations of the diagonal connections show opposite behaviour to the deformations of the axial connections; the strain in the diagonal connections increases with increasing confinement, such that the capacity is reduced in multi-axial loading of the same sign, compared to uni-axial loading, when diagonal strain is used to define onset of failure. This characteristic is used to derive failure criteria for spalling failure under higher confinement.

The resulting failure envelope from the failure criteria that were derived in this Chapter captures two types of failure modes that were observed in literature: Coulombic shear failure under an angle with the loading direction and tensile and tensile-compressive failure perpendicular to the loading direction in case of dominating tension or in-line with the loading direction in case of dominating compression. In addition, a spalling failure limit is set.

Near a crack-tip or other discontinuities in the ice, stresses and strains concentrate and the failure criteria for continuous ice do not correctly predict failure in the lattice model. A separate failure criterion is developed for application near crack-tips for in-plane and out-of-plane deformation. For in-plane deformation, it is shown that the crack propagation load and onset of unstable crack propagation can be predicted well with the lattice model, when comparing to analytically obtained results. For bending deformations, it is shown that an in-situ beam test where no stress relief holes were drilled can be used to find the critical concentrated bending strain that gives onset of crack propagation.

With the failure criteria for an ice plate in compression, tension and bending and strain concentrations near discontinuities, a complete set of failure criteria is derived that is required to simulate ice-sloping-structure interaction scenarios in multi-directional loading conditions. It is shown that the failure criteria have a minimal dependence on cell-size and orientation.

5

Applicability of the lattice model to simulating ice failure in complex loading conditions

In Chapter 4, it was shown that the deformation of the springs in the different orientations in the plane of the lattice can be combined to define the strain state in the lattice and to check whether the ice fails. In this Chapter, the onset of failure is analysed for complex loading conditions: combined bending, shear and torsion. The strain state as a consequence of bending and torsional deformations studied, similar to the bending beam simulation in Chapter 4.

To keep the number of nodes in the model, and therefore the number of equations, limited there is only one layer of particles in z-direction of the plate. As a consequence of this, out-of-plane spalling failure under high confinement as described in Schulson et al. (2006) cannot be accurately simulated. A limiting failure cap is set for this failure mode in Chapter 4. To capture out-of-plane shear deformations, shear springs are present in the lattice in out-of-plane direction. In this Chapter, it is shown that in case of dominating out-of-plane shear deformations, the strain in the out-of-plane shear springs could indicate that this failure mode is likely to occur.

5.1 L-beam tests

The L-beam test is described by Murdza et al. (2016) to investigate ice failure under complex loading conditions, consisting of bending, shear and torsion. An L-shaped beam was cut in the ice, leaving the toe end of the L attached to the ice plate. Loading was applied at the free end. Three L-beam tests were performed during fieldwork in Wahlenbergfjorden, Nordaustlandet on Svalbard in April 2015, three on fast ice of Van Mijen Fjord (Spitsbergen) in March 2016 and three on fresh water lake ice in Longyearbyen in November 2014 and 2015.

The shape and dimensional parameters of the L-beam tests are shown in Figure 5-1. Five of the nine tests gave failure patterns similar to the pattern indicated with dashed line number 1. Cracks ran from a place at a distance c from corner B that varied between 0 and 8 cm. The angle relative to the beam root varied between 9.2 and 33.8°. The failure surfaces were inclined relative to the in-plane direction. Finite element simulations indicated that torsion components influenced the location at which failure started. In four of the tests a failure pattern indicated with dashed line number 2 was observed. Murdza et al. (2016) explain this by the length of the toe end, L_2, being relatively long for the mechanical ice properties in the field, resulting in a dominating bending failure component.

The L-beam test is simulated with the lattice model to study failure under complex loading conditions in more detail. Parameters of one of the tests at Wahlenbergfjorden are applied and summarised in Table 5-1. The calculated Young's modulus using Frankenstein and Garner (1967) and Vaudrey (1977) equations is 1.4GPa. Flexural strength was based on beam tests performed at Wahlenbergfjorden as part of the same testing campaign; a value of 0.339MPa was found using simple beam method (Ryghseter et al., 2015).

The failure pattern for this test is indicated in Figure 5-1 with dashed line number 1. The crack runs from a point at $c = 6$ cm from the beam root at corner B and progressed towards the opposite edge of the L under an angle of 26.6°.

Table 5-1: Input parameters for L-beam test simulations

Parameter	Symbol	Quantity	Unit
Length toe end of L	L1	1.05	m
Length free end of L	L2	1.95	m
Width at free end	a	0.55	m
Width at root	b	0.55	m
Ice thickness	h	0.565	m
Loading rate	dF/dt	500	N/s
Failure load	F	6	kN
Young's modulus ice	E	1.4	GPa
Poisson ratio	ν	0.3	-
Flexural strength ice	σ_f	0.339	MPa
Ice density	ρ_{ice}	920	kg/m^3

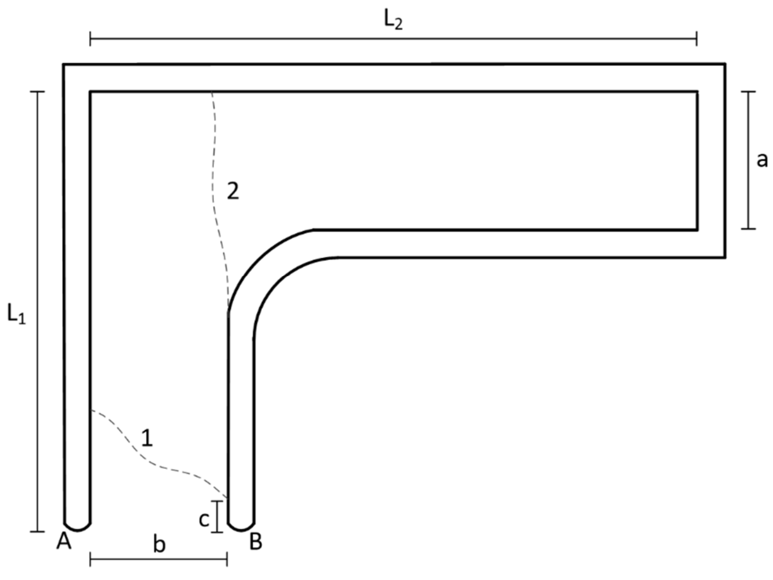

Figure 5-1: L-shaped beam indicating dimensional parameters and crack patterns that were observed in field tests by Murdza et al. (2016)

5.2 Bending and torsional strain

Figure 5-2 shows the lattice model for the L-beam test. A load of 6kN was applied to the free end of the L and the strains in the deformed state were recorded. In Chapter 4, the criterion for bending failure was derived as a function of the mean of the strain state due to bending and torsion η_{mean} as well as the associated radius of the Mohr diagram R_η and the compressive σ_c and flexural strength σ_f of the ice and Poisson's ratio ν :

$$\frac{F_1\eta_{mean}\frac{h}{2}+R_\eta\frac{h}{2}}{F_2}\frac{E}{\sigma_f}\geq 1$$

with

$$F_1=\frac{1+\nu}{1-\nu}\frac{\frac{\sigma_c}{\sigma_f}-1}{\frac{\sigma_c}{\sigma_f}+1} \tag{5.1}$$

$$F_2=\left(1+\frac{\frac{\sigma_c}{\sigma_f}-1}{\frac{\sigma_c}{\sigma_f}+1}\right)\frac{1+\nu}{2}$$

Figure 5-3 shows the magnitude of the left-hand side of equation (5.1) for the first three rows of cells near the root of the lattice. These rows are indicated in Figure 5-2. The failure criterion is exceeded for all cells (the value on the vertical axis exceeds 1); the flexural strength may have been higher than the strength applied in the simulation. Strain concentrations are found near corner A. No stress relief holes were simulated with the lattice, while in field tests these holes prevent the high bending strains near the beam root. Near corner B, the strain state has approximately the same relative magnitude for the first three rows, such that due to local material variations the onset of fracture could occur further away from the corner, as observed in the field experiment. The highest strain state in the L-beam is found in the cell indicated with "Bending failure" Figure 5-2 such that bending failure with a pattern similar to that indicated with number 2 in Figure 5-1 occurs. When rounding off the corner in a smoother manner, the strains near the corner could reduce and the strains at the root would become governing, resulting in a failure pattern similar to that indicated with number 1.

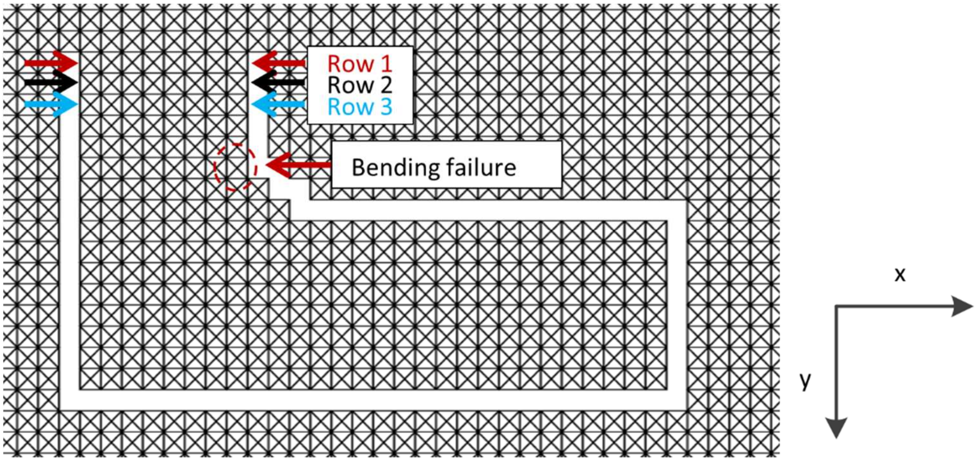

Figure 5-2: L-beam test simulated with the lattice model. Rows for which data is presented as well as the location of bending failure are indicated in the figure.

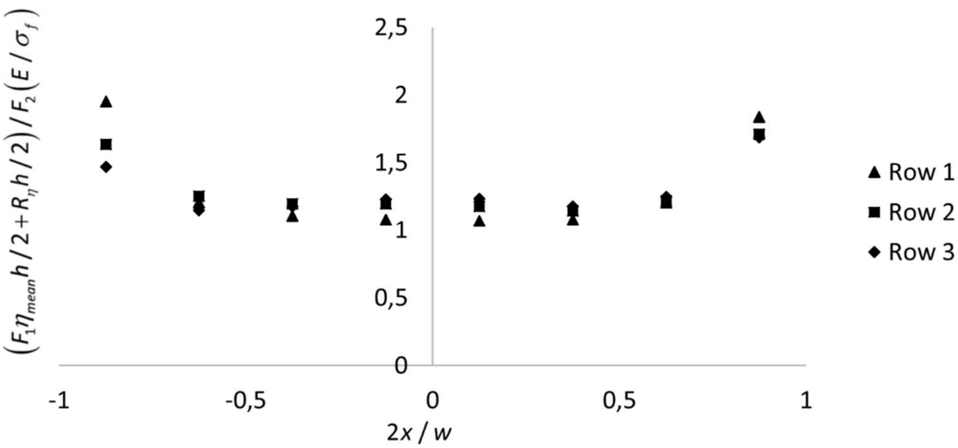

Figure 5-3: Strain state due to bending and torsion deformation normalised by the flexural strength over the first three rows of the L-beam near its root in the lattice model. x=0 corresponds with the centre of the root.

5.3 Shear strain

Figure 5-4 shows the shear deformation in the out-of-plane shear springs, normalised by the shear modulus and shear strength for the first three lattice cell rows near the L-beam root. ε_s is the maximum out-of-plane shear strain, normalised by the cell size, of the four axial connections surrounding a cell. The figure indicates that high shear strains are present, even at some distance from the corner, which is where the ice failed in some of the field tests. Timco and Weeks (2010b) describe shear strength values from the 'more reliable tests' in a range from 400 to 700kPa for granular ice and 550 to 900kPa for columnar sea ice, however shear is one of the least understood properties of sea ice. A shear strength of 700kPa was used to normalise the shear strain in this example. Extremes in shear stress with the same order of magnitude as the shear strength could indicate that the shear component may play a role in failure.

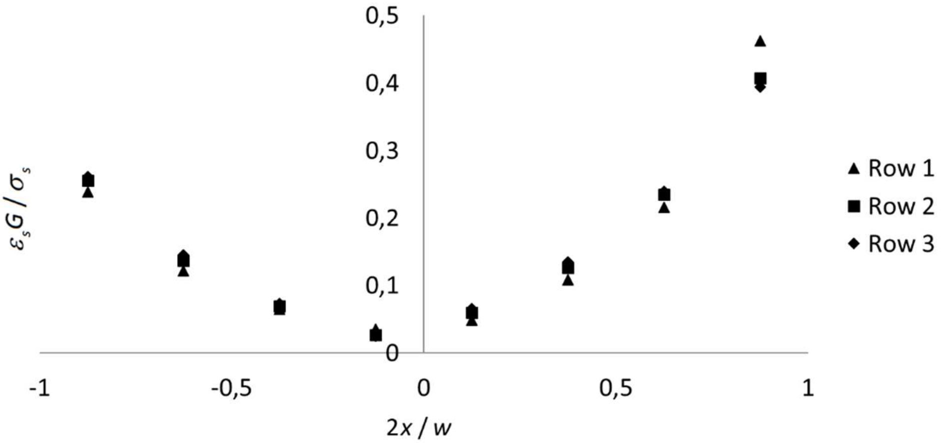

Figure 5-4: Shear deformation normalised by the shear strength over the first three rows of the L-beam near its root in the lattice model

In all field tests the failure surface was inclined with respect to the vertical plane, which cannot be reproduced with a 2D plate model. Since shear failure cannot be accurately modelled with the lattice model, it is recommended to use a 3D model to study the L-beam tests if detailed failure simulation is required. The lattice model can give an indication of shear loads and the location of shear failure. In engineering applications shear failure is usually not governing over bending and tensile failure. Therefore, the 2D plate model is appropriate in many applications.

5.4 Conclusion

The failure criterion derived in Chapter 4 could explain the locations of fracture that were observed in an L-beam tests, described in literature, where complex loading conditions of combined bending and torsion were present. In addition to bending and torsion, shear could have played a role in the onset of fracture. Out-of-plane shear failure cannot be modelled in detail over the thickness of the ice with the lattice model, however the lattice model can give an indication of high shear loads and indicate the location of shear failure. In engineering applications shear failure is often not governing over bending and tensile failure. Therefore, the 2D plate model is appropriate in many applications.

6

Simulation of interaction between ice and a conical structure

This Chapter describes a number of test cases that were simulated with the lattice model to verify its applicability in simulating ice-structure interaction and to validate the fracture criteria that were derived in Chapter 4. The test cases are based on physical model tests for a rigid downward breaking conical structure interacting with ice floes of various sizes that were done as part of a Joint Industry Project and are described by Bruun et al. (2011). Fracture in bending, splitting and combinations of these were observed in the tests and simulated with the lattice model. Interaction with ice floes of different sizes and shapes are studied.

Parts of this chapter have been published in Proceedings of the 24th International Conference on Port and Ocean Engineering under Arctic Conditions, 2017 (van Vliet and Metrikine, 2017b). Optimization of the models' failure criteria after the publication has led to updated simulation results in the current work.

6.1 Description of the basin tests

A number of basin tests from the testing campaign described in Bruun et al. (2011) were simulated with the lattice model. In these tests, a conical structure was moved through an ice field with ice floes of various sizes. The structure was rigidly connected to the carriage and moved at a velocity of 0.1 m/s. The structure is depicted in Figure 6-1 where its main dimensions are shown. An overview of the ice floe distribution before start of the tests is provided in Figure 6-2 for larger and smaller floe sizes.

Ice properties are provided in Table 6-1.

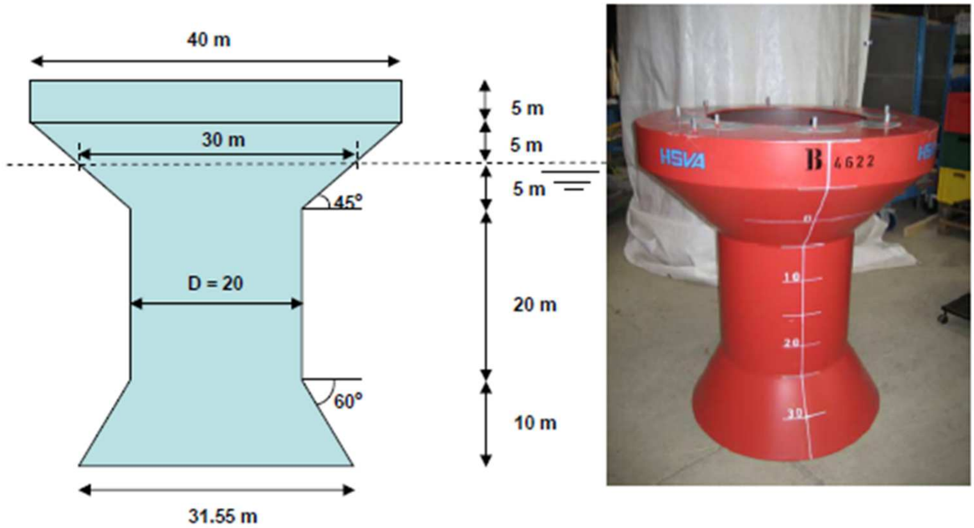

Figure 6-1: Dimensions of the structure that was used during the ice basin tests. The waterline diameter was 30m. (HSVA, 2010a)

Basin test results in this Chapter are reported with full scale quantities, in line with the presentation of the results in test reports. Froude scaling with a scaling factor of $\lambda = 36$ was used. Appendix 4 shows that the calculations performed with the lattice model are in agreement with Froude scaling laws and therefore that there is no difference in results when comparing full scale lattice model results with model test results that were scaled with Froude scaling laws, compared to comparing results obtained and simulated on model scale. There are differences between basin ice and natural ice and it is not possible to scale all strength and stiffness parameters correctly at the same time. These differences are not addressed in this work, but should be considered when using basin test results to design full-scale structures.

a b

Figure 6-2: Overview of the floe distribution in the ice basin a) large floes and b) smaller floes (HSVA, 2010a)

Table 6-1: Input parameters for ice-structure interaction simulations with the lattice model, based on model test input parameters. Froude scaling with scaling factor 36 was used for full scale quantities.

Parameter	**Quantity basin**	**Quantity full scale**	**Unit**
Ice thickness	0.083	3	m
Flexural strength	20.8	750	kPa
Young’s modulus	0.24	8.7	GPa
Ice density	846	846	kg/m3
Water density	1006	1006	kg/m3
Waterline diameter of the cone	0.83	30	m
Velocity of the cone	0.017	0.1	m/s
Compressive strength	0.11	4	MPa
Tensile strength	20.8	750	kPa
Friction coefficient	0.1	0.1	-

The Young's modulus was determined in the basin by using the plate method, where the ice cover is loaded at some locations along the centreline of the ice tank with a weight of 100g. The deflection of the ice cover at the load is measured and from this deflection the Young's modulus is calculated. Measurements were performed on an intact ice sheet, before the broken ice was created for the test. The average Modulus of Elasticity of the measurements at three locations was 242 MPa, corresponding with a value of 8.7 GPa on full scale. Measurements at the timing of the simulated tests are not available and therefore a Modulus of Elasticity of 8.7 GPa is applied for the simulations.

Ice density was measured by submerging a 120x120x83mm ice floe and measuring the displaced water and buoyant force. The average density of 5 ice samples was used for the numerical simulations: 846kg/m3. The water density in the basin was 1006kg/m3.

The uniaxial compressive strength was measured by a test frame with a hydraulic piston which applied a uniform pressure to the specimen samples of size 83x167x333mm. The flexural strength of the ice was increased to 40 to 70kPa model scale for this test (1440 to 2520kPa) as lower strength ice could not be handled. The relation between bending and compressive strength was used to evaluate the compressive strength in the basin with the ice of lower flexural strength. A ratio of 4.3 to 10.9 times the flexural strength was found in the measurements. A compressive strength of 5.3 times the flexural strength, 4MPa was selected for the numerical simulations. A value on the lower side of the reported crushing strength range was used, assuming the crushing strength is relatively low for basin ice with low flexural strength.

The flexural strength was determined in the basin by a cantilever beam test. Strength measurements were taken in the level ice, of which the broken ice sheet was made. The target flexural strength was 750kPa. The flexural strength was measured at several moments in time before starting of the test using beams of 500x166x83mm model scale; 18x6x3m full scale. The measured flexural strength was reducing from 1080kPa 7 hours before the test to 792kPa 3 hours before the test. The target flexural strength was used for the numerical simulations of the basin test as the measured strength was declining towards the target strength of 750kPa before commencement of the test. During or after the test the flexural strength was not measured.

A flexural strength of 750kPa corresponds to a failure load of 375kN, using equation (4.25) for a clamped beam. The beam test is simulated with the lattice model and a factor f=0.75 is found for the failure criterion in equation (4.29). The right-hand-side of equation (4.29) is populated with parameters from the beam test done in the basin and gives the failure criterion for bending near discontinuities.

No splitting test was done. Therefore, the strain in bending and tension is added up as described in Section 4.1.3 and the failure criterion is applied to the combined deformation.

A tensile strength test was not performed. Therefore, the tensile strength in the simulations was based on the parameters and results of the flexural strength test. The tensile strength is the stress at the root of the clamped beam when applying the failure load, giving a value of 750kPa using equation (4.25).

A friction coefficient between the cone and the ice of 0.1 was measured and applied in the simulations.

Shear strength of the ice was not measured in the basin. A shear strength of 700kPa was applied, the same as the shear strength selected in Chapter 5. Failure in shear was not observed in the results generated with this shear strength value.

6.2 Description of the numerical ice floes and contact with the structure

For the simulations with the lattice model the input parameters from the basin tests (Table 6-1) were directly applied by substituting Young's modulus, ice density and ice thickness in the mass and stiffness parameters of the lattice. Numerical ice floes of different shape and size (165x165m, 55x55m and 34x68m) were generated. Confinement was applied at the back of the ice floes, representing confinement from the other ice floes in the basin. Fracture criteria that were derived in Chapter 4 were used; the ice strength parameters were changed to those measured in the basin.

To simulate the contact load between the lattice and the conical structure, a simplified contact algorithm was applied. This algorithm works as follows: at each time step of the simulation the amount of overlap between the ice and the structure is determined, based on the structural shape, its indentation and the deflection and rotation of the ice. From this overlap, the contact area, a_{crush} in Figure 6-3, is determined. Please note that Figure 6-3 is a side view of the overlap and that contact forces are calculated in three dimensions. The force from the structure on the ice, which is a linear function of the contact area and the contact strength of the ice, and works perpendicular to the structure, is calculated and applied to the ice. A friction force acts along the slope of the structure and is related to the contact force via a friction coefficient. Initially a contact strength parameter of 200kPa was used.

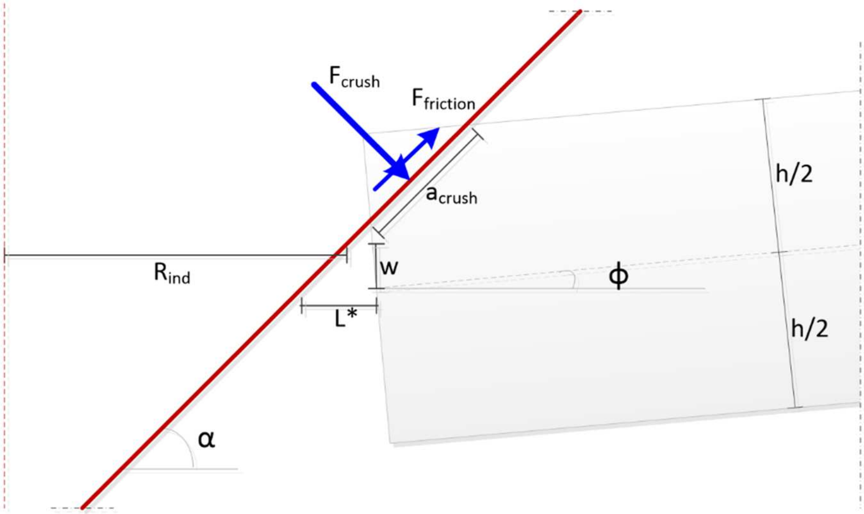

Figure 6-3: Side view indicating important parameters in determining the contact load: R_{ind} is the radius of the cone, α is the slope of the cone, L* is the distance between the centre of the ice edge and the cone, w is the deflection of the ice, φ is the tip rotation of the ice, h is ice thickness, a_{crush} is the contact length between the ice and the structure, F_{crush} is the crushing load, perpendicular to the structure and $F_{friction}$ is the friction load, directed opposite to the motion of the ice along the structure.

The square lattice structure that is used in the simulations has a straight edge where the conical structure encounters the ice. When the cone encounters the edge, only one or two lattice cells are loaded and therefore the load is applied very locally. With a high contact strength parameter, the load at the edge builds up relatively quickly and does not distribute further over multiple cells at the lattice model edge, but results in failure near the edge. In the basin ice, the edges of the ice are not perfectly straight in the simulated cases and the shape of the ice edge distributes the contact load over the ice edge. With a lower value of the contact parameter, the ice loading is distributed over multiple cells at the lattice model edge, simulating the load distribution in the basin. A relatively small contact parameter compared to the crushing strength was therefore chosen for the simulations and a sensitivity study (increasing the contact strength parameter) was performed to investigate the effect of the contact on the failure of the ice in Section 6.3.2. The contact parameter used in the simulations is purely artificial and a more sophisticated boundary element, for example the one described by Hendrikse et al. (2018), should be used in order to account for the proper redistribution of stresses at the ice edge in contact with the structure. The latter development is beyond the scope of this thesis.

6.3 Interaction with a large square-shaped ice floe

In the basin tests the structure was pulled through the centre of a large ice floe of 165x165m. First a piece of ice failed in bending, showing a circumferential breaking pattern (Figure 6-4a). This is referred to as the first encounter. Shortly after the structure encountered the new broken edge of the ice, a long crack appeared along the centre of the ice floe and the ice failed close to the structure in combined radial and circumferential fracture as shown in Figure 6-4b. This is referred to as the second encounter. During the remaining encounters between the structure and the ice floe, splitting and circumferential and radial fracture alternated.

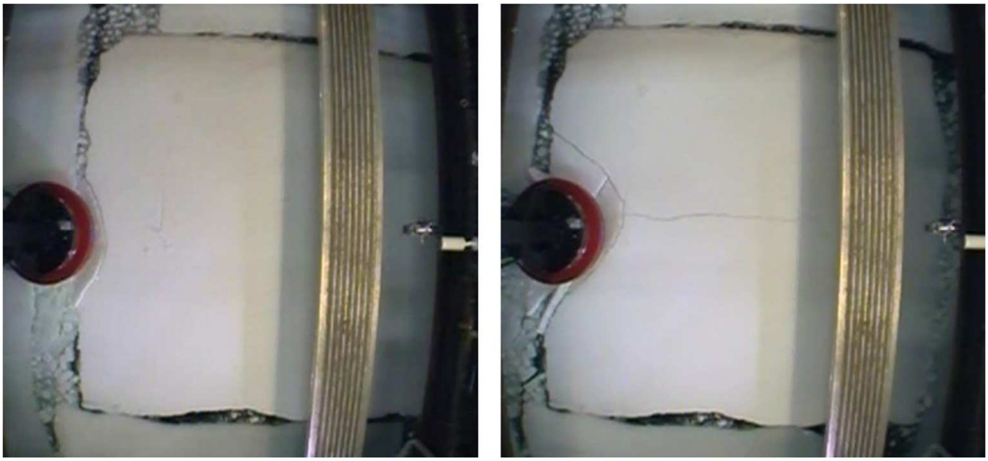

a b

Figure 6-4: Encounter between the structure and a large ice floe of 165x165m; images from model test video a) Fracture pattern at first encounter b) fracture pattern at second encounter (HSVA, 2010b)

The load on the structure that was measured during the model test campaign from the start of the encounter between the structure and the ice floe up to the moment of circumferential fracture shown in Figure 6-4b, is presented in Figure 6-6. The dashed line named Ftot in the figure is the total resultant force, Fx, Fy and Fz are the forces in x- y- and z-direction respectively, according to the axis system presented in Figure 6-5. The duration of the loading build-up is similar during both interactions, about 10s. The failure load during the second encounter is about 30% higher than at the first encounter. Upon failure, the slope of the loading curve changes in the basin tests, but the load does not immediately drop to zero. An explanation for this is that the crack can still transfer load in compression and frictional shear and the ice rubble that is present in front of the structure, as shown in Figure 6-8 keeps loading the structure. Only when the ice starts clearing away alongside the structure, the load reduces.

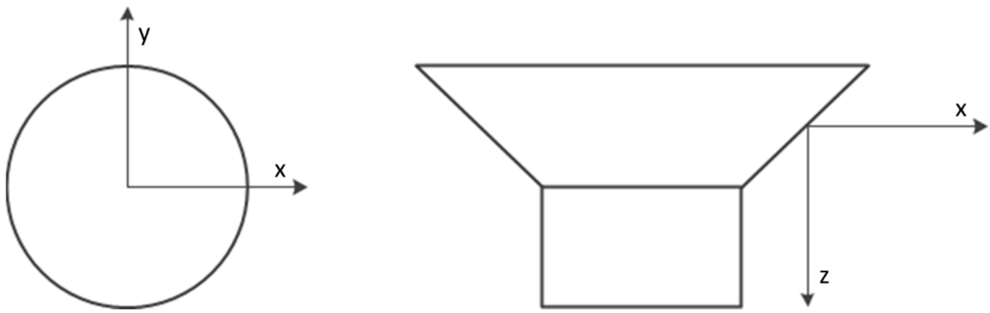

Figure 6-5: Structure axis system, left: top view, right: side view

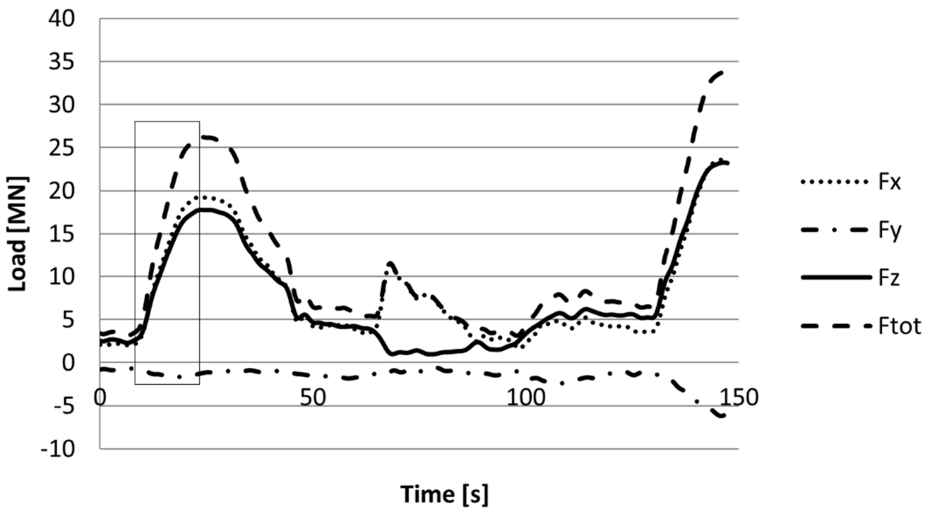

Figure 6-6: The load on the structure that was measured during the model test campaign from the start of the encounter between the structure and the ice floe up to the moment of circumferential fracture

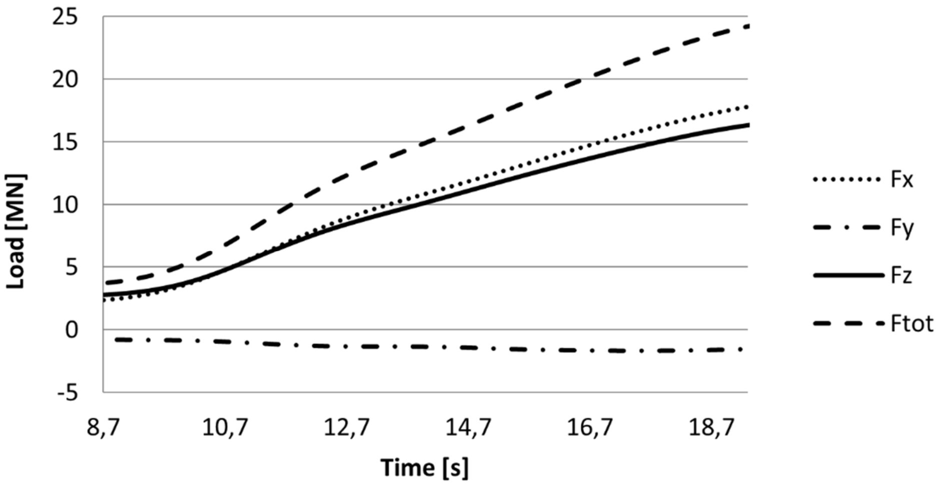

Figure 6-7: Zoom-in on the load build-up stage during interaction with a 165x165m ice floe

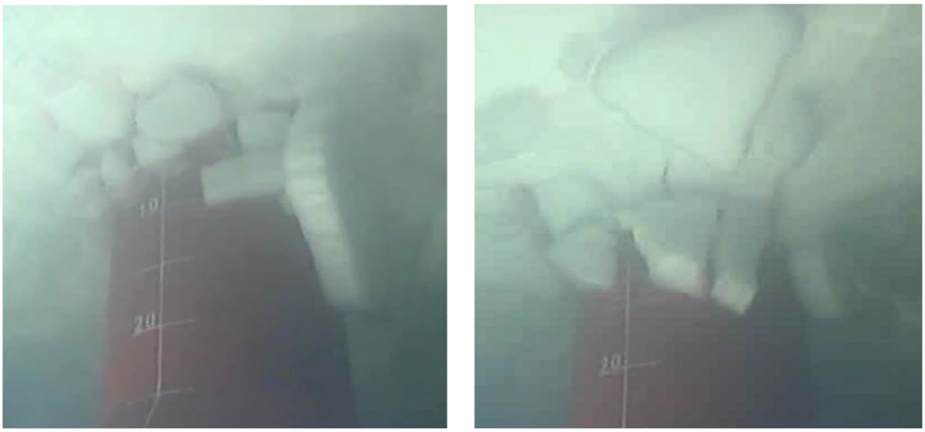

a. b.

Figure 6-8: Ice rubble accumulates near the structure, beneath the ice, images from model test video. a) At the start of encounter with the ice floe b) At the time of circumferential failure at the second encounter (HSVA, 2010a)

A comparable situation to the stages where the load builds up, up to the moment of circumferential failure, is simulated with the lattice model. One of these stages is indicated with the boxed section in Figure 6-6 and a zoom-in on this stage is provided in Figure 6-7. The lattice model was developed to simulate breaking of ice and clearance of ice around the structure is not modelled.

The resulting fracture patterns of the simulations with the lattice model are presented in Figure 6-9 for two different mesh sizes. The fracture patterns consist of a long crack forming in the centre of the ice floe and a circumferential crack near the structure, which formed after the long crack. This is comparable with the fracture pattern that was observed during the second encounter between the structure and the ice in the model tests (Figure 6-4b). The loading curve is presented in Figure 6-10 for the finer mesh and in Figure 6-11 for the coarser mesh. There is almost no difference between the graphs for the different cell sizes. Failure occurred at a load of 7MN (5.4MN in x- and 4.6MN in z-direction), which is significantly lower than the 24MN measured during the second encounter in the basin tests. A timestep after failure of 10^{-5} s was applied for the simulations. Further details of the numerical simulations are provided in Section 4.2.1.

Of the ice parameters that were measured in the basin, the tensile and flexural strength have the most influence on the breaking load. The actual flexural strength in the basin tests was close to the target strength. This parameter was used to determine failure near a crack tip. Splitting and circumferential failure did not initiate close to a crack tip and therefore initial failure load is determined from the tensile strength parameter. The tensile strength was derived from the stress at the root in the beamtest. Stress concentrations near the edges at the beam root were not accounted for and therefore it is likely that the tensile strength in the basin was in reality higher than the parameter that was used for the calculations. Frederking and Svec (1985) describe an increase of 25-33%. It is therefore not expected that the stress concentrations could explain the factor 3.5 difference in loading between simulations and basin tests. It is recommended to measure tensile strength of the ice in basin tests. Further differences in load levels could be related to the rubble that built-up in front of the structure during the model tests as well as rotation and sliding of the ice and this is discussed further in Section 6.3.1.

The duration of the load build-up simulated with the lattice model is three times longer than in the basin tests. The contact model in the lattice model may not be exactly representative for the contact in the basin. This could also explain why the split in the finer mesh is slightly longer: the load distribution near the structure is smoother in case of the fine mesh as there are more nodes in contact with the structure. The effect of the contact model is further discussed in Section 6.3.2.

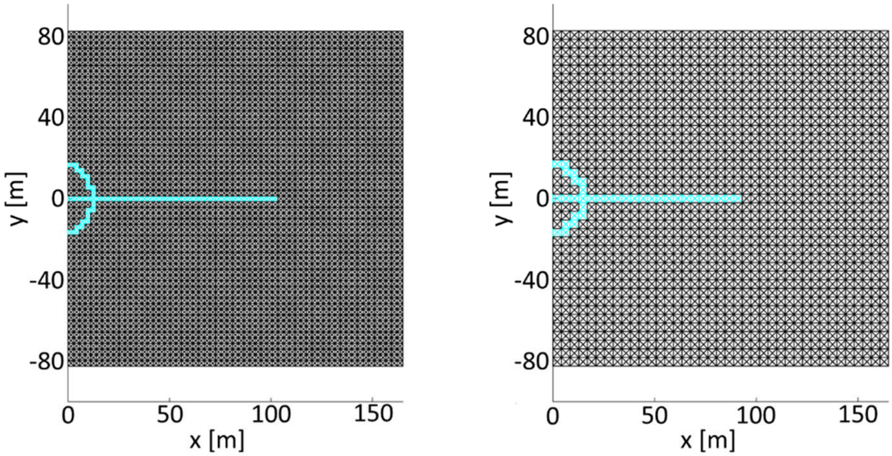

Figure 6-9: Fracture pattern from lattice model simulation of interaction between a 165x165m ice floe and a sloping structure. The lattice model was built-up from a) 60x60 masses b) 40x40 masses

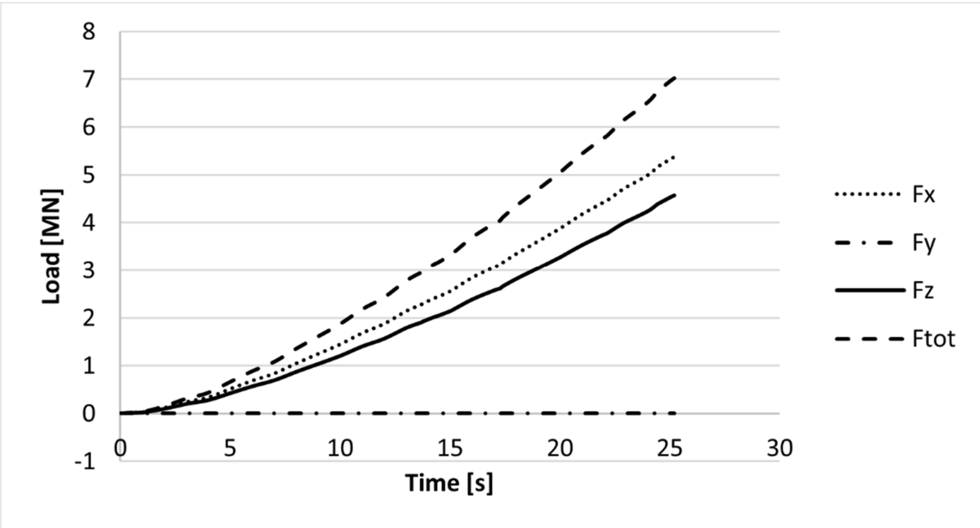

Figure 6-10: Build-up of the load until the moment of fracture during lattice model simulations of interaction between a 165x165m ice floe and a sloping structure – mesh of 60x60 masses

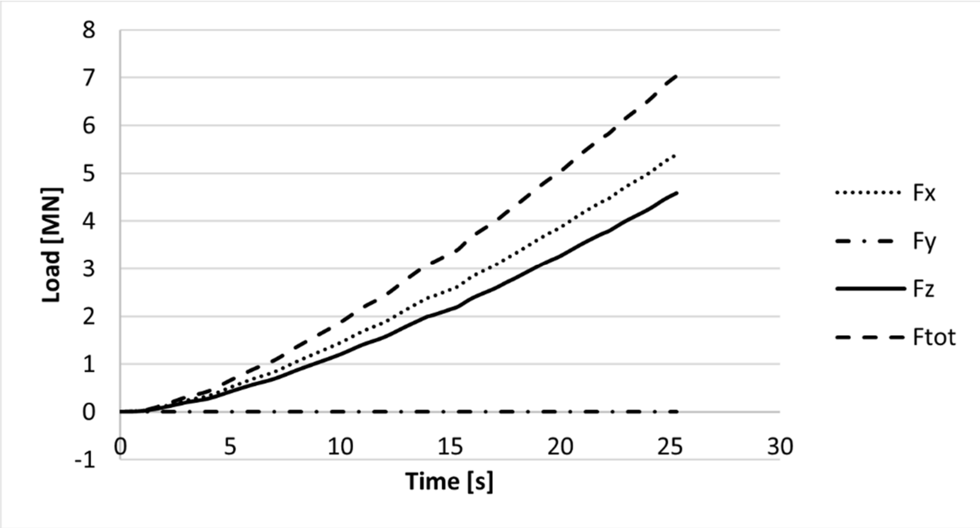

Figure 6-11: Build-up of the load until the moment of fracture during lattice model simulations of interaction between a 165x165m ice floe and a sloping structure – mesh of 40x40 masses

The fracture criterion for combined bending and in-plane loading was derived in Chapter 4 as a function of the mean strain ε_{mean} at the top or bottom of the plate as well as the associated radius of the Mohr diagram R_{ε} at the top or bottom of the plate and the compressive σ_c and flexural strength σ_f of the ice and Poisson's ratio ν :

$$\frac{F_1 \varepsilon_{mean} + R_{\varepsilon}}{F_2} \geq \frac{\sigma_f}{E}$$

with

$$F_1 = \frac{1+\nu}{1-\nu} \frac{\frac{\sigma_c}{\sigma_f} - 1}{\frac{\sigma_c}{\sigma_f} + 1} \tag{6.1}$$

$$F_2 = \left(1 + \frac{\frac{\sigma_c}{\sigma_f} - 1}{\frac{\sigma_c}{\sigma_f} + 1} \right) \frac{1+\nu}{2}$$

The mean versus radius of the strain states in the lattice model, multiplied by the Young's modulus are plotted in Figure 6-12 for all lattice cells, up to and including the moment of fracture. Strain states at the top of the lattice are indicated with blue dots, while strain states at the bottom of the lattice are represented by grey dots. Strain states causing failure of the cell are indicated with orange dots. The failure envelope that follows equation (6.1) is indicated with a dashed line. The axes where the principle stresses are zero $\sigma_{11}=0$ and $\sigma_{22}=0$ are indicated with arrows. These axes provide the boundaries of the different quadrants of the loading regime, which are indicated with letters T-T for Tensile-Tensile quadrant, T-C for Tensile-Compressive quadrant and C-C for Compressive-Compressive quadrant. The figure can be mirrored about the horizontal axis. Tensile-Compressive strain is dominant and important for the simulation of failure. Unfortunately, there is no measurement data available to define the Tensile-Compressive part of the failure envelope of ice.

Bending failure was governing over shear failure in the simulation with the lattice model. A critical out-of-plane shear stress of 0.7MPa was set in the model.

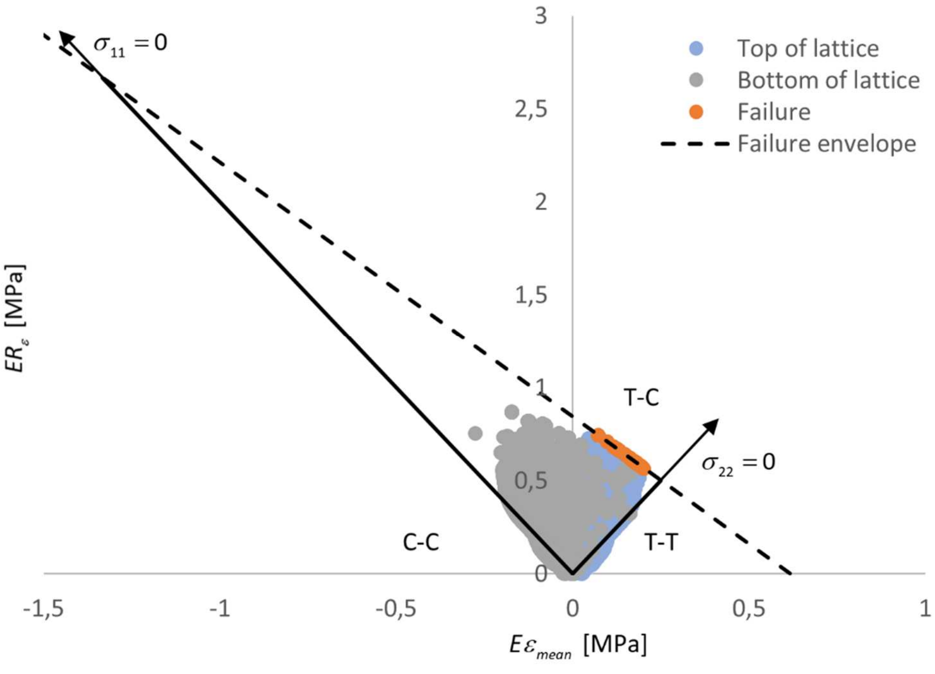

Figure 6-12: Mean and radius of the Mohr diagram for strain, multiplied with Young's Modulus, for the cells in the lattice model during the simulation of ice-structure interaction at the top and bottom of the lattice. The strain state at the moment of failure is indicated with orange dots. Tension-tension (T-T), Compression-Compression (C-C) and Tension-Compression (T-C) quadrants are indicated with letters.

6.3.1 Loads in rotating and sliding phases

The failure load in the lattice model simulation was significantly lower than the load measured in the basin tests. This could be related to the rubble that built-up in front of the structure during the model tests as well as rotation and sliding of the ice that contributed to the loading and is analysed further in this section.

In the analysis report of the basin tests (Lu and Løset, 2010), the ice loads were calculated with methods from ISO19906 (ISO, 2010) and similar to the results obtained with the lattice model, it was found that the ISO code underestimated the actual ice loads. Three interaction phases are described in the report, following Kämäräinen (2007): breaking phase, rotating phase and sliding phase. In the breaking phase, ice is loaded in interaction with the structure, until the ice strength is exceeded and a piece or multiple pieces of ice break off. After breaking, in the rotating phase, the ice pieces close to the structure are rotated to align with the structure's slope, while the area on top of the ice floe gradually fills with water. When rotated and surrounded by water, broken ice pieces pile up ahead of the structure, before clearing around the structure, loading the structure in the sliding phase. Reference is made to Valanto (2001) who showed that for a bay-class ice breaker the loads in the rotating and sliding phases contribute significantly to the total load on a structure.

Only the breaking phase is simulated with the lattice model. To find an explanation for the discrepancy between the loads measured in the basin and the loads found in simulations with the numerical model, estimates of the loads in the rotating and sliding phase are made in this section for the scenario simulated with the lattice model.

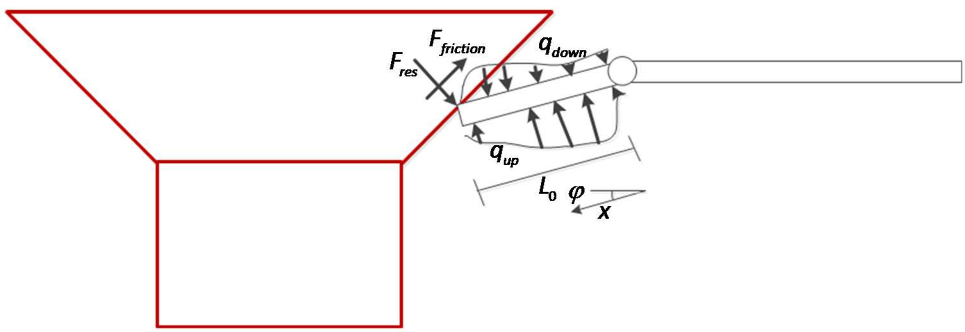

Figure 6-13: Side view of ice floe and broken ice pieces during rotating phase

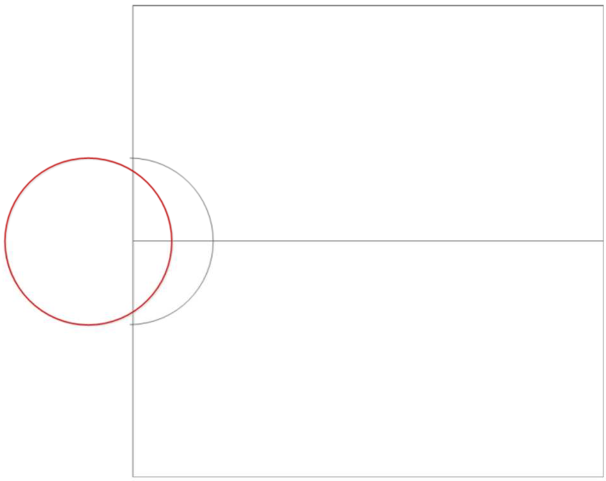

Figure 6-14: Top view of ice floe and wedge-shaped broken ice pieces

Figure 6-13 and Figure 6-14 present an overview of the loading on a broken piece of ice, during the rotating phase. It is assumed that the broken piece is rigid and wedge shaped and pushed downward at the tip. The curved side has broken off from the ice floe, but due to frictional shear forces it remains in contact with the intact part of the ice floe and this contact is simulated by a moment-free connection. The downward forces q_{down} on the ice floe consist of the mass q_{mass} and the backfill $q_{backfill}$ on the flow, which are calculated with:

$$q_{mass} = \frac{\rho_{ice} g h (L_0 - x)\pi}{2} \tag{6.2}$$

where L_0 is the radius of the broken ice piece and x is the distance from the connection to the ice floe, and

$$q_{backfill} = \frac{\rho_{water} g (x - x_1) \sin\varphi (L_0 - x)\pi}{2}, \ x \geq x_1$$

with

$$x_1 = \frac{\rho_{ice}}{\rho_{water}} \frac{h}{\sin\varphi} \tag{6.3}$$

where x_1 is the distance from the connection where the backfill reaches to and φ is the rotation of the ice floe. The backfill works perpendicular to the ice floe and the mass works in vertical z-direction. The upward forces q_{up} on the ice floe consist of initial buoyancy, which is already working on the ice floe before rotation starts, and additional buoyancy that increases with the rotation of the piece of ice; both acting perpendicular to the piece of ice:

$$q_{buoyancy} = \frac{\rho_{water} g \pi}{2} \left(\frac{\rho_{ice}}{\rho_{water}} h(L_0 - x) + x \sin\varphi (L_0 - x) \right) \tag{6.4}$$

The resulting forces on the structure are a resulting force F_{res} perpendicular to the structure and a frictional force $F_{friction}$ parallel to the structure, where

$$F_{friction} = \mu F_{res} \tag{6.5}$$

and μ is the friction coefficient between the ice and the structure. The resulting force on the structure can now be calculated by setting the sum of the bending moments at the connection with the ice floe to zero. Parameters from Table 6-1 are used for the calculation. Figure 6-15 presents the resulting force on the structure for a broken wedge of 10m radius and a wedge of 20m radius, with and without backfill. Both the length of the broken wedge and the amount of backfill have significant influence on the magnitude of the loading on the structure. The load is plotted for a single wedge. In the simulation two wedges broke of, doubling the load. With a breaking length of around 20m and assuming no complete backfill, the loading on the structure could reach about 10-20MN, corresponding with 8-16MN in x-direction and 6-13MN in z-direction. The duration of load build-up in the basin test however is around 18s, allowing for a rotation of 10 degrees of the 10m long ice floe and 5 degrees of the 20m long ice floe, giving a maximum load on the structure of 3MN.

There are additional effects that could increase the loading during the rotational phase. Loads associated with the acceleration of the mass and viscous damping of the ice floe when submerged could increase the total loading. These dynamic effects are expected to be small for the low interaction velocity in the test. The bending moment at the beam root is in reality not zero, which would result in higher interaction loads and a gradual transition from breaking to rotating phase.

In addition, rubble beneath the broken pieces (Figure 6-8) increases the downward resistance on the broken pieces of the ice floe and with that the interaction loads. Figure 6-8a shows the rubble ahead of the structure at the start of the encounter with the ice floe, that built-up in interaction with other ice in the basin. A volume of 3000m^3 of ice is estimated, giving an extra upward force of 4.7MN.

The loading in the sliding phase depends on the rubble that is present near the structure. This clearance takes place continuously during the basin test and the magnitude can be estimated from the time signal of the load measurements (Figure 6-6) as the non-zero load between the load peaks, where no breaking and rotating occurs. The load due to sliding has a magnitude of about 2-10MN and is also present during the breaking and rotating phase, resulting in further increased loading on the structure.

It is expected that the difference in loading between the basin test and the lattice model is associated with rotation and sliding of ice floes in combination with broken pieces of ice and rubble providing resistance to the rotation and sliding and applying further loads on the structure. With the lattice model only the breaking phase was simulated and therefore much lower loading was found.

To simulate ice clearance, it is recommended to link the lattice model to existing models, for example discrete element models, which have proven to be successful in simulation of ice rubbling and clearance (Hopkins, 2004; Liu and Ji, 2017).

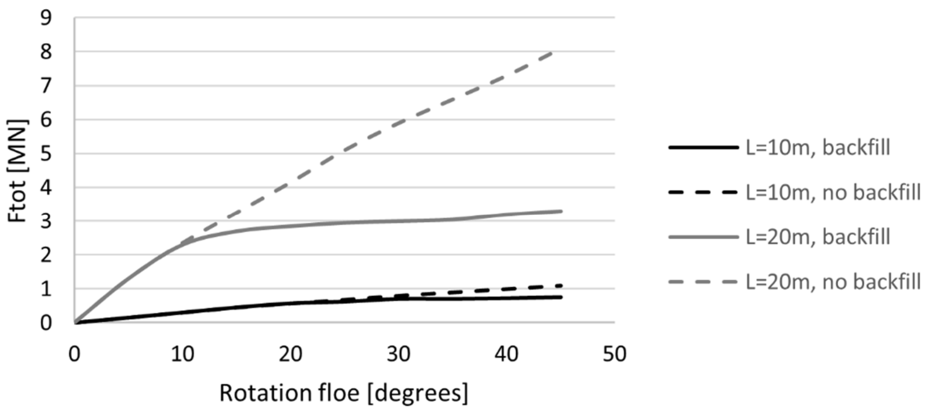

Figure 6-15: Resulting force on the structure for a broken wedge of 10m radius and a wedge of 20m radius, with and without backfill during rotating phase

6.3.2 Effect of the contact parameter on ice loading

To investigate the sensitivity to the contact loading, the contact strength parameter was changed to 2000kPa (10x higher) and the same simulation was performed with the lattice model. The resulting fracture pattern is presented in Figure 6-16. The increased contact strength gave a smaller crushed area of the ice in interaction with the structure and the ice deformed more in bending locally near the structure, while the load built up quicker and was distributed over less lattice cells. The failure pattern changed and a piece of ice broke off close to the structure.

This situation is comparable to the piece of ice that broke off during the first encounter of the ice with the structure in the basin tests. Figure 6-17 shows that the duration of the load build-up stage reduced significantly and is of similar order as in the basin tests. The failure loads remained of the same order of magnitude: 4.8MN in x- and 4.0MN in y-direction and are significantly lower than the 19MN in x- and 17.5MN in z-direction measured during the first encounter with the ice in the basin tests.

After the first encounter with the ice floe in the basin tests, the damaged edge of the ice floe had a curved shape. This was not simulated with the lattice model, but could result in a better load distribution between the ice and the structure, compared to a straight edge. This loading distribution could be achieved in the lattice model by the reduced contact stiffness parameter, giving a failure pattern comparable to that of the second encounter in the basin tests.

The contact parameter, and with that the way in which the loading is transferred from the structure to the ice, influences the failure pattern and the duration of the load build-up. In the simulations in this thesis a simplified contact model was applied, with which failure patterns observed in the basin tests could be simulated. To further improve the prediction of the duration of the loading build-up, it is recommended to further develop the contact model, taking into account locally deformed or damaged shape of the ice floe.

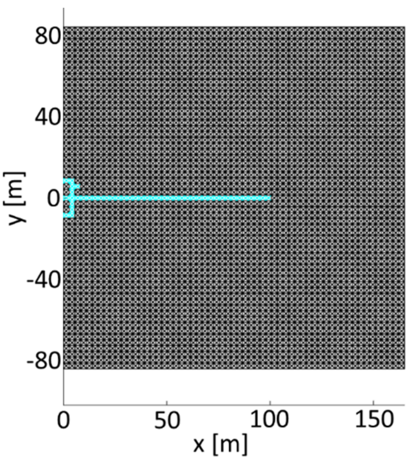

Figure 6-16: Fracture pattern after lattice model simulations of interaction between a 165x165m ice floe and a sloping structure with a relatively high contact strength parameter

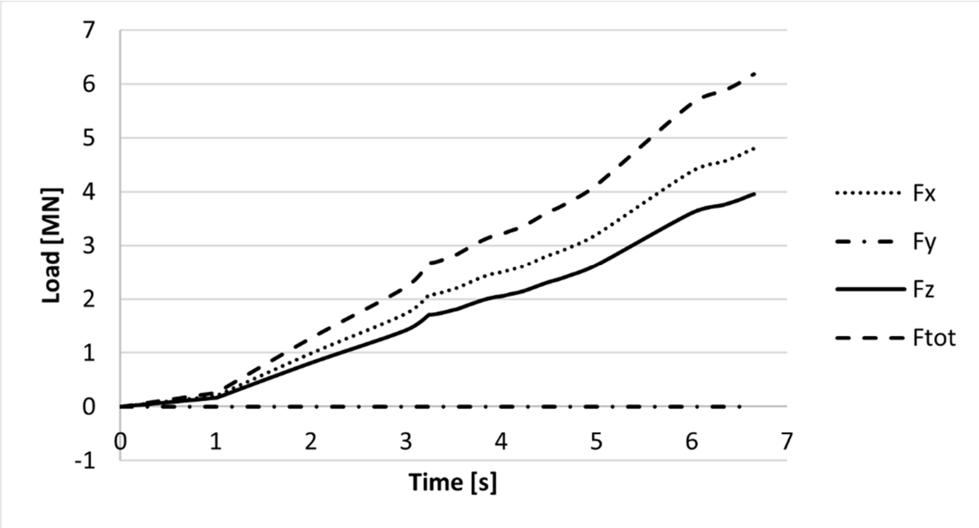

Figure 6-17: Build-up stage of the load until failure during lattice model simulations of interaction between a 165x165m ice floe and a sloping structure with a relatively high ice strength at the edge

6.4 Interaction with a smaller square ice floe

During interaction with a smaller ice floe of 55x55m in the basin, first a piece of ice broke off circumferentially. During the second encounter with the structure, the square floe split apart as shown in Figure 6-18. The time series of the load around the time of bending failure is presented in Figure 6-19. The loading on the structure is lower than for the larger ice floe of 165x165m and the build-up time is longer. The loading around the time of splitting failure is presented in Figure 6-20. The loading in z-direction hardly changes and most of the loading is in x-direction. The high loading in x-direction could be explained by the ice floes being confined by other ice floes in the basin. The rubble beneath the structure (Figure 6-21) could prevent the ice from sliding downwards along the slope, such that the resulting load in z-direction on the structure is limited.

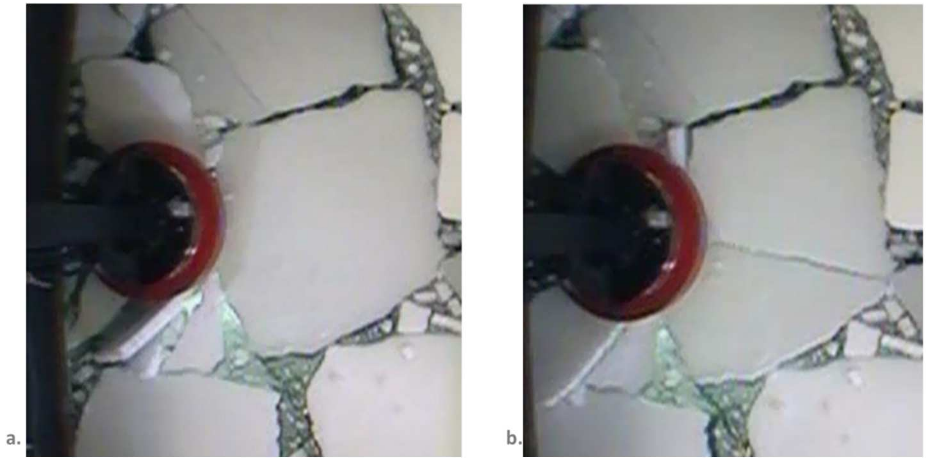

Figure 6-18: Encounter between the structure and a small square ice floe of 55x55m; image from model test video a) Fracture pattern at first encounter b) fracture pattern at second encounter (HSVA, 2010b)

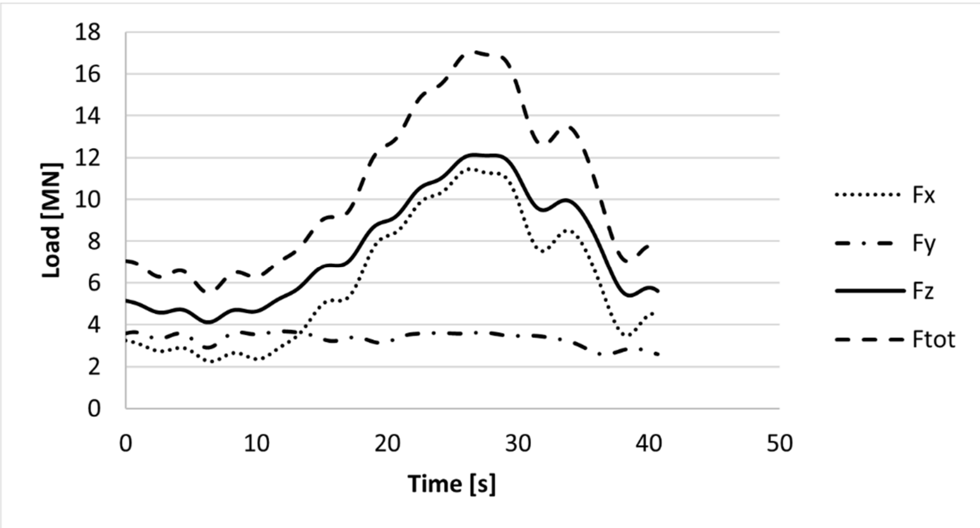

Figure 6-19: Time series of the load around the time of bending failure near the corner of the 55x55m ice floe

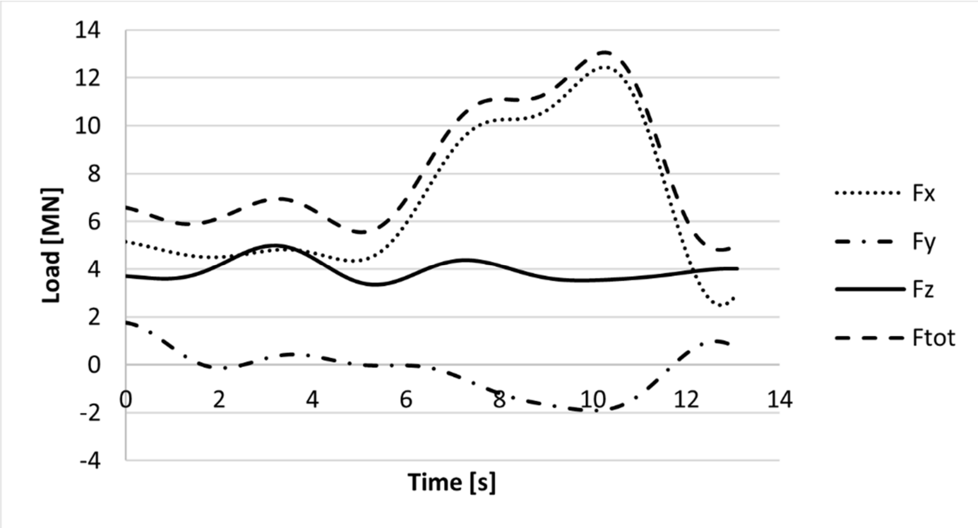

Figure 6-20: Time series of the load around the time of splitting failure of the 55x55m ice floe

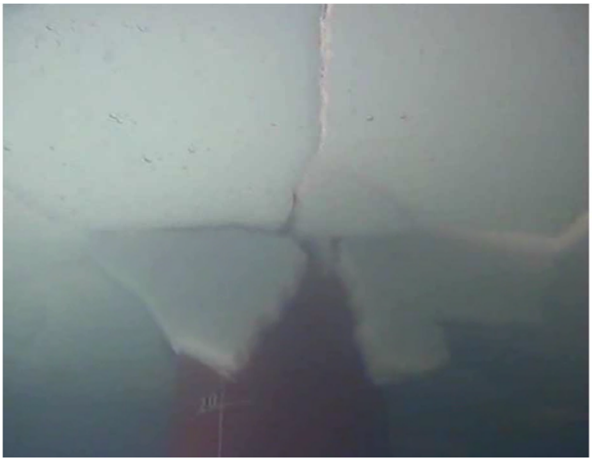

Figure 6-21: Image from underwater video just after splitting of the 55x55m ice floe (HSVA, 2010b)

Two situations are simulated with the lattice model, one where the structure encounters the ice near one of the corners and one where the structure encounters the ice floe in the centre. Fracture patterns are depicted in Figure 6-22. In case the structure encounters the ice floe near the corner, a radial crack occurs, that turns towards the ice edge. In the basin tests, also a part of the corner broke off, although with cracks that were more inclined compared to the ice floe edges. This could be a result of the locally irregular shape of the ice in the basin tests. When the structure encountered the ice floe at the centre, the ice floe split in two, similar to what was observed in the basin. A timestep after failure of $2 \cdot 10^{-5}$ s was applied for this simulation. Further details of the numerical simulations are provided in Section 4.2.1.

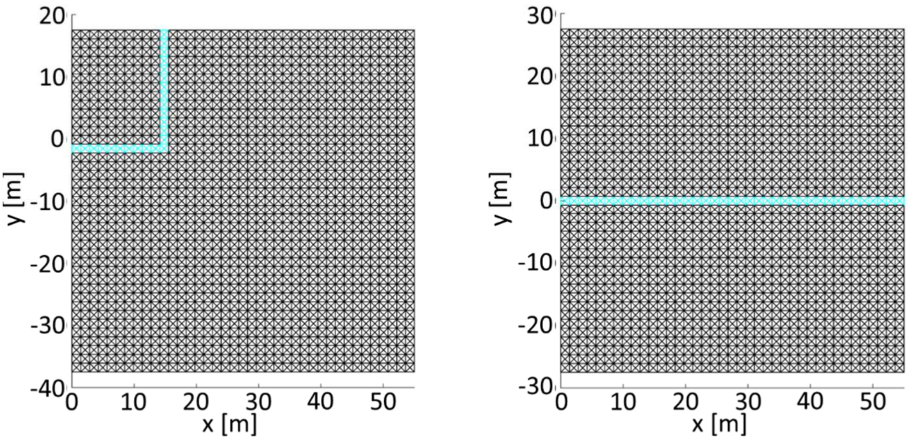

Figure 6-22: Fracture pattern from lattice model simulation of interaction between a 55x55m ice floe and a sloping structure. The structure encountered the ice plate a) near the corner b) in the centre

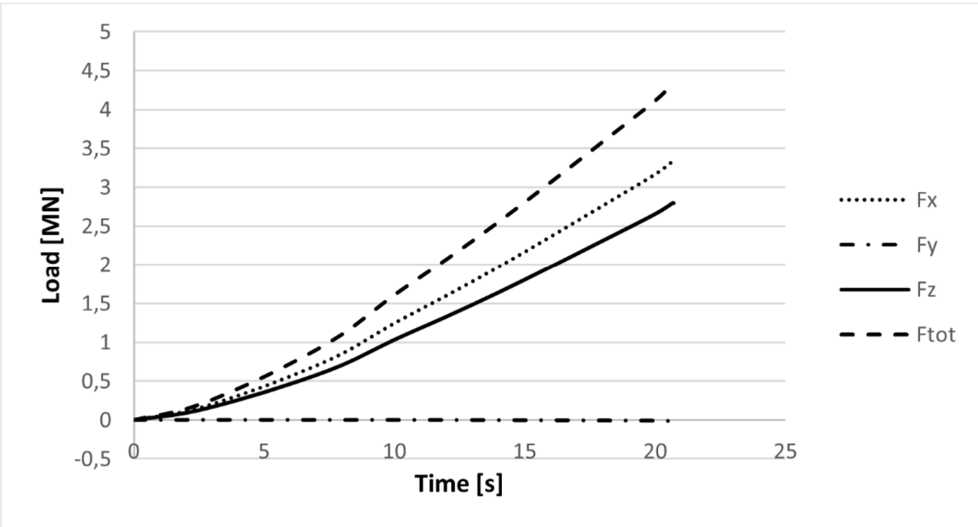

Figure 6-23: Time signal of the load from start of interaction up to the moment of failure for encounter near the edge of a 55x55m ice floe

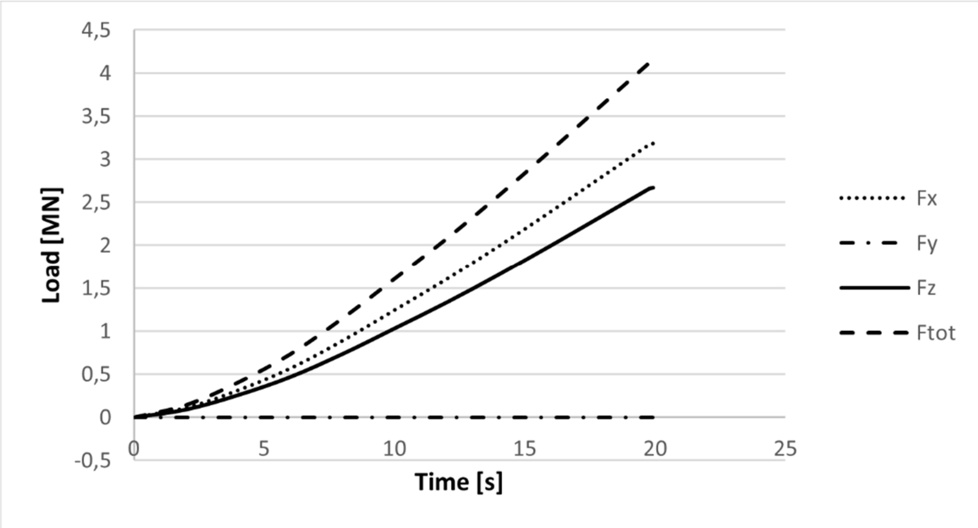

Figure 6-24: Time signal of the load from start of interaction up to the moment of failure for encounter at the centre of a 55x55m ice floe

Time series of the interaction load between the structure and the 55x55m ice floe are provided in Figure 6-23 for encounter near the corner and Figure 6-24 for encounter in the centre. In case the ice is loaded near the corner, the corner breaks off after 20.7s at a load of 3.3MN in x- and 2.8MN in z-direction. The duration of load build-up is similar to that observed in the basin.

When the ice floe is encountered in the centre, the ice floe splits at a load of 3.2MN in x- and 2.7MN in z-direction. A higher load and shorter duration of load build-up was observed in the basin tests. In the simulation with the lattice model, the load component is z-direction is higher than in the model tests, most likely because there is no rubble accumulation in front of the structure in the lattice model.

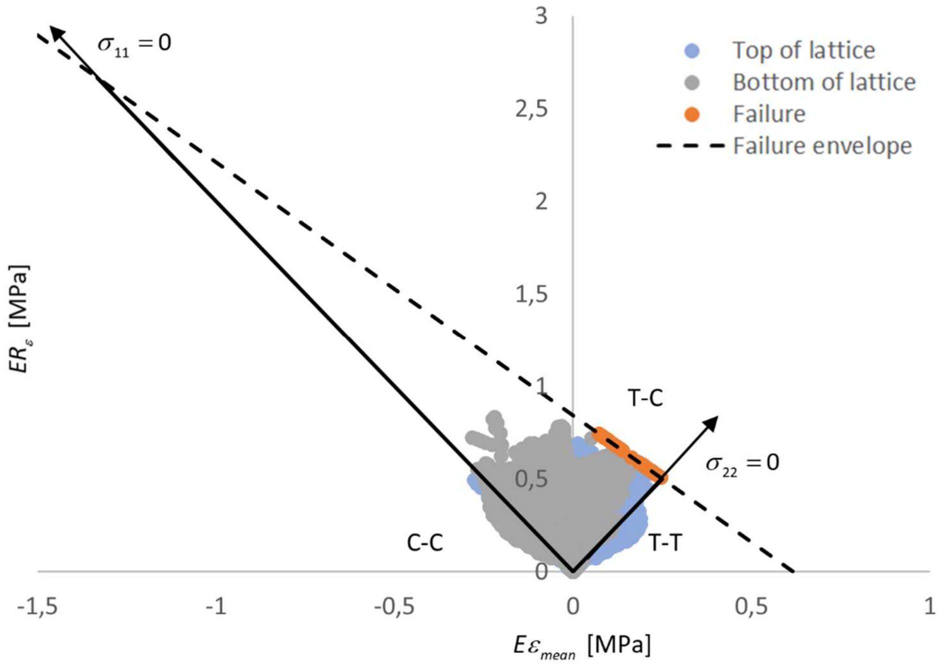

Figure 6-25: Mean and radius of the Mohr diagram for strain, multiplied with Young's Modulus, for the cells in the lattice model during the simulation of ice-structure interaction near the corner of a 55x55m ice floe at the top and bottom of the lattice. The strain state at the moment of failure is indicated with orange dots. Tension-tension (T-T), Compression-Compression (C-C) and Tension-Compression (T-C) quadrants are indicated with letters.

The mean versus radius of the strain states in the lattice model, multiplied by the Young's modulus are plotted in Figure 6-25 for encounter near the corner and Figure 6-26 for encounter in the centre, for all lattice cells, up to and including the moment of fracture. Similar to the results for interaction with the 165x165m ice floe, the Tensile-Compressive strain is dominant for deformations and fracture for interaction between the structure and the 55x55m ice floe.

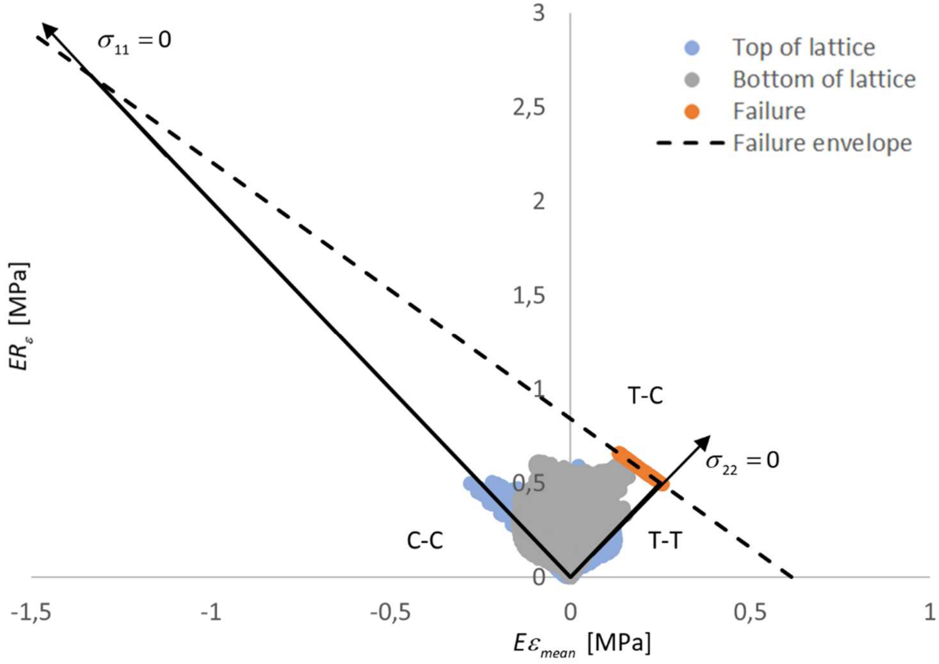

Figure 6-26: Mean and radius of the Mohr diagram for strain, multiplied with Young's Modulus, for the cells in the lattice model during the simulation of ice-structure interaction in the center of a 55x55m ice floe at the top and bottom of the lattice. The strain state at the moment of failure is indicated with orange dots. Tension-tension (T-T), Compression-Compression (C-C) and Tension-Compression (T-C) quadrants are indicated with letters.

6.5 Interaction with a smaller rectangular ice floe

In interaction with a 34x68m ice floe in the basis tests, the ice floe split apart and two triangular-shaped pieces of ice broke off as shown in Figure 6-27. The time series of the loading on the structure, measured in the basin around the time of failure is presented in Figure 6-28. The loading on the structure is less than for the 165x165m ice floe. The time series does not show a clear load reduction upon failure. Some cyclic behaviour with a period of about 5s is observed.

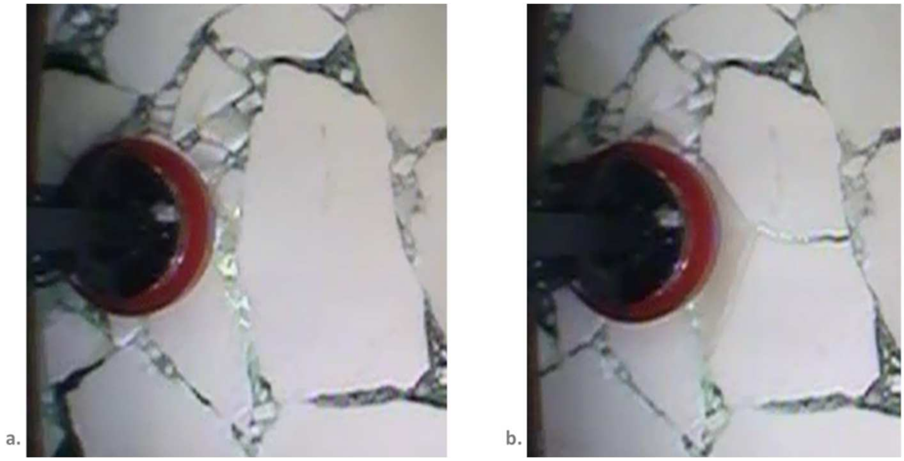

Figure 6-27: Image from model test video. Encounter between the structure and a small rectangular ice floe of 69x34m (HSVA, 2010b)

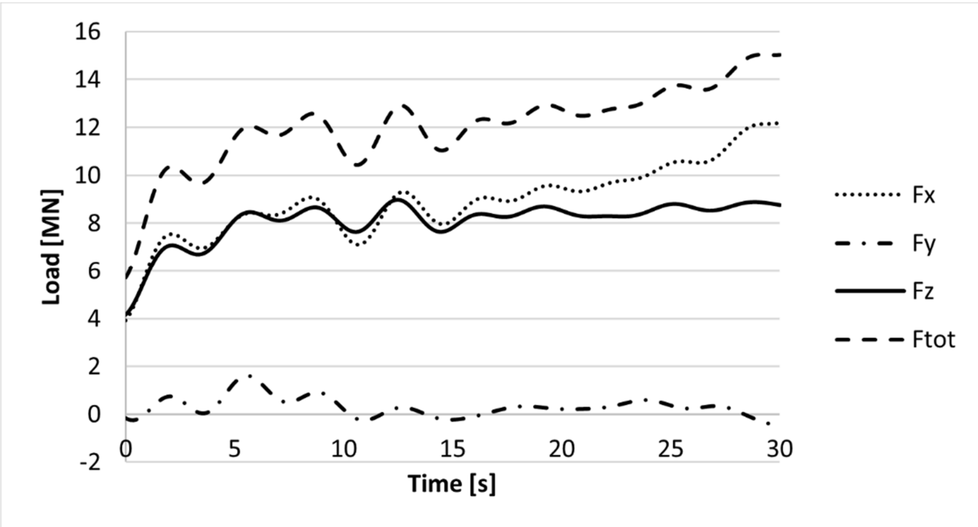

Figure 6-28: Time series of the load around failure of the rectangular ice floe, measured during basin tests

In the simulation with the lattice model, a similar failure pattern is observed as shown in Figure 6-29. The ice splits in two at the centre and two pieces break off in a shape that is wider near the structure and narrower near the intersection with the central crack. A timestep after failure of $2 \cdot 10^{-5}$ s was applied for this simulation. Further details of the numerical simulations are provided in Section 4.2.1.

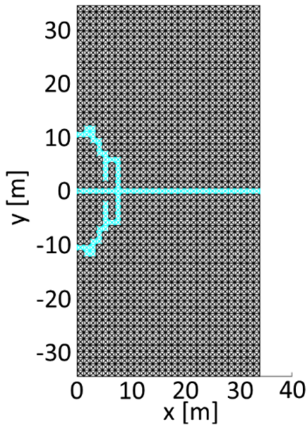

Figure 6-29: Fracture pattern from lattice model simulation of interaction between a 55x55m ice floe and a sloping structure

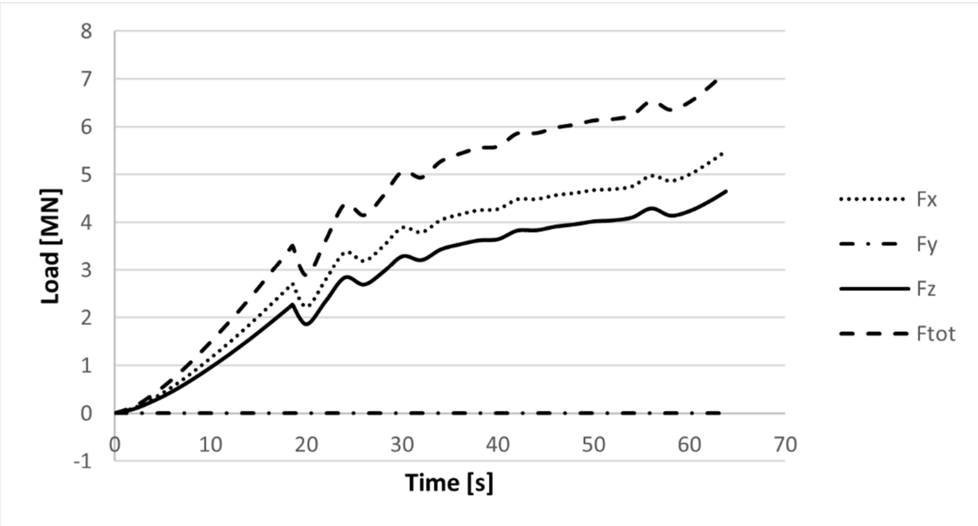

Figure 6-30: Time signal of the load from start of interaction up to the moment of failure for encounter of a 34x68m ice floe

The load signal of the interaction is presented in Figure 6-30. The split in the ice occurred at 18.5s at a load of 2.7MN in x-direction 2.3MN in z-direction and circumferential failure took place at 63.8s at a load of 5.5MN in x-direction 4.6MN in z-direction. After splitting, cyclic behaviour with a period of about 6s was observed. The load level upon fracture was closer to that of about 8MN measured in the basin, compared to the ice floes of other sizes, however there is still a discrepancy in load level between the simulations and the basin tests, where loads in the lattice model are structurally lower.

The mean versus radius of the strain states in the lattice model, multiplied by the Young's modulus for the 34x68m ice floe is plotted in Figure 6-31. Also for this floe size the Tensile-Compressive strain is dominant for deformations and fracture.

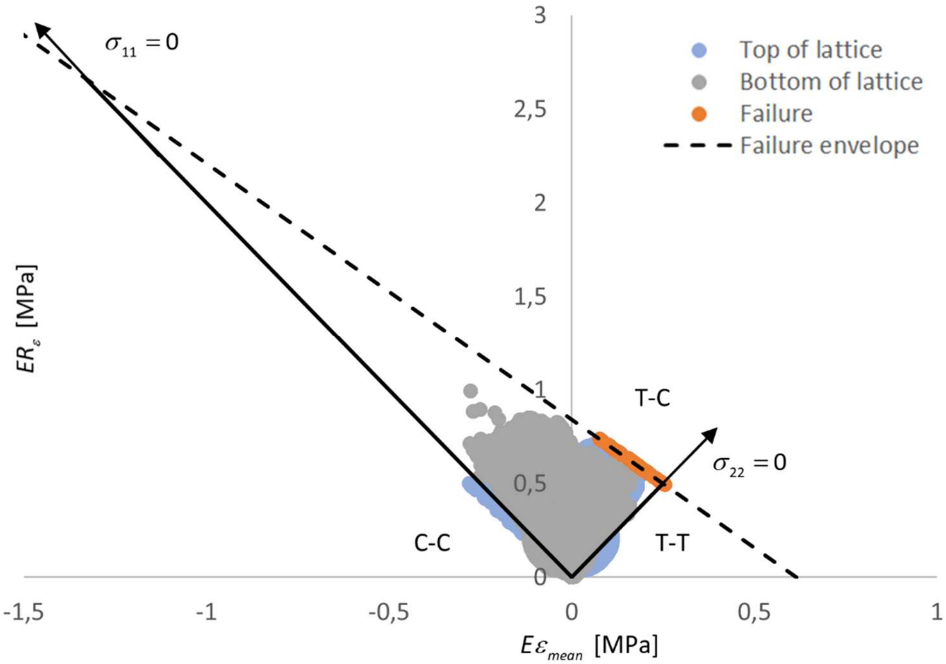

Figure 6-31: Mean and radius of the Mohr diagram for strain, multiplied with Young's Modulus, for the cells in the lattice model during the simulation of ice-structure interaction of a 34x68m ice floe at the top and bottom of the lattice. The strain state at the moment of failure is indicated with orange dots. Tension-tension (T-T), Compression-Compression (C-C) and Tension-Compression (T-C) quadrants are indicated with letters.

6.6 Conclusions and recommendations

Interaction between ice floes of different sizes and a sloping structure has been simulated with the lattice model and compared to basin tests. Deformation and failure criteria in the 2-dimensional lattice model are based on first principles, enabling physically sound simulation of deformation and fracture processes of the ice plate material. The input parameters to the lattice model are measured ice and structural properties.

Fracture patterns are comparable between basin tests and lattice simulations, for different floe sizes. Both circumferential and splitting fracture, which were observed in the basin, were observed in simulations with the lattice model. The load distribution at the interface between the structure and the ice has an influence on the velocity with which the load on the structure builds up and on the failure pattern that is observed. A simplified contact model was applied in the simulations. It is recommended to further develop the contact model, taking into account the locally deformed or damaged shape of the ice floe.

Failure loads in simulations with the lattice model are smaller than those measured in the basin. It is expected that the higher loading that was observed in the basin tests is to some extent associated with a likely underestimation of the tensile strength adopted in the numerical model and for the largest part with the rotating and sliding phases of the ice, where the ice pieces close to the structure are rotated to align with the structure's slope. Rotation and sliding of ice floes in combination with broken pieces of ice and rubble providing resistance to the rotation and sliding and applying further loads on the structure could result in the load levels that are observed in the basin tests. With the lattice model only the breaking phase was simulated and therefore significantly lower loading was found. To simulate ice clearance, it is recommended to link the lattice model to existing models, for example discrete element models, with proven success in simulation of ice rubbling and clearing. It is also recommended to measure tensile strength of the ice in basin tests.

The strain state of the lattice cells during the simulations was analysed and most of the deformations were in combined tension and compression. The Tensile-Compressive part of failure diagram is most important in simulating interaction between ice and a conical structure. However, no measurement data is available to define this part of the failure envelope. It is recommended to focus ice strength measurements on combined tensile and compressive multi-axial loading conditions.

7

Conclusions

In this thesis, a lattice model is developed to simulate deformation and fracture of an ice plate in interaction with a structure. This will facilitate the design of sloping structures for (sub-)Arctic environments. In-plane and out-of-plane vibrations in the lattice plate model correspond with those of a shear deformable plate in the long-wave approximation. The failure criteria, which have a minimal dependence on the size and orientation of the mesh, are linked to field measurement data of the ice. The deformation and failure criteria in the lattice model are based on first principles, enabling physically sound simulation of deformation and fracture processes of the ice plate material. Failure in compression, tension, bending and splitting are simulated with the lattice model, providing a complete set of failure scenarios relevant to study interaction between ice and sloping structures. By means of numerical assessment, a multitude of structures and loading conditions can be analysed and structural shapes can be optimized for interaction with ice at reasonable costs.

To enable simulation of out-of-plane deformations of the ice, a lattice model for the out-of-plane dynamics of a shear-deformable plate has been formulated. The model is composed of masses and springs whose morphology and properties were derived to match, in the long-wave approximation, the out-of-plane deformations of thick plates as described by the Mindlin-Reissner theory. A lattice model was selected to simulate the ice plate because of its simplicity and properties that are advantageous for fracture simulation: stress singularities do not occur in the lattice and simulation of failure is done by removing connections from the lattice model, such that re-meshing is not required.

The application of the lattice model is not limited to ice. However, the intention of this study is simulation of ice-structure interaction and therefore verification was done using parameters of an ice sheet. Focussing upon linear dynamics, the model is consistent with a continuum plate theory in the low frequency band. Differences emerging at higher frequencies are attributed to the dispersion, anisotropy and specific boundary effects (in case of finite dimensions) of the lattice model. Wavelengths smaller than two times the cell size cannot be described with the lattice model. Wavelengths relevant for simulation of ice-structure interaction processes are relatively long and therefore the discrepancy between the continuum and the lattice model in the high frequency band does not form a limitation for the intended purpose. Effects of hydrodynamics and material damping have been effectively included in the model and have shown good correspondence with the continuum solution.

A lattice model for in-plane vibrations of a plate in plane strain conditions is described in literature and is adjusted in the current work to plane stress conditions. Combined with the lattice model for out-of-plane deformations a single model was formed, which captures in- and out-of-plane deformations of a shear deformable plate under the assumption of small deformations.

A study of the Poisson effect showed discrepancies between expected plate deformations and those found with the lattice model. Stiffness parameters were adjusted based on a method described in literature. The steady-state response of the lattice model with original and adjusted spring stiffness parameters showed good agreement with continuum response in a dynamic simulation of the response of a simply supported plate. For higher frequency loading, the deviation obtained with the lattice model with the adjusted spring stiffness parameters was slightly larger than with the original spring parameters. The most relevant processes in interaction between ice and sloping structures are associated with the lower frequencies, where both methods provide good agreement with the continuum. The adjusted parameters resulted in proper inclusion of the Poisson effect in the lattice cells and have therefore been used for further study of sea ice fracture. The stiffness parameters that were derived with both methods are in agreement for a Poisson ratio of 1/3, which is a typical value for sea ice. This value was used for practical examples of ice failure.

In ice plate failure tests described in literature, different loading conditions resulted in different failure modes: splitting under unconfined loading, Coulombic shear friction under lower confinement and spalling under higher confinement. Mohr-Coulomb type failure criteria were derived for the lattice model, in which tensile, compressive and in-plane shear deformation of the connections are used to find the strain state of the lattice cell. The radius of the Mohr diagram for axial and shear strain in the connections reduces with increasing confinement. This characteristic is used to capture the increasing capacity of the plate with increasing confinement in multi-axial compressive and tensile loading. The splitting and Coulombic shear friction failure modes are captured by linking the criterion for onset of failure to the corresponding fault orientation observed in tests. Similarly, a criterion is derived for tensile conditions that may occur at the outer fibre of the ice plate, near the surfaces, due to tension induced by bending and torsion. Deformation due to in-plane tension and out-of-plane bending can be added-up and applied in a single failure criterion while accounting for differences in tensile and flexural strength as well as potential differences in flexural strength in upward and downward bending.

The deformations of the diagonal connections in the lattice show opposite behaviour to the deformations of the axial connections; the strain in the diagonal connections increases with increasing confinement, such that the capacity is reduced in multi-axial loading of the same sign, compared to uni-axial loading, when diagonal strain is used to define onset of failure. This characteristic is used to derive failure criteria for spalling failure under higher confinement.

The resulting failure envelope captures two types of failure modes that were observed in literature: Coulombic shear failure under an angle with the loading direction and tensile and tensile-compressive failure perpendicular to the loading direction in case of dominating tension or in-line with the loading direction in case of dominating compression. In addition, a spalling failure limit is set.

Near a crack-tip or other discontinuities in the ice, stresses and strains concentrate and the failure criteria for continuous ice do not correctly predict failure in the lattice model. A separate failure criterion is developed for application near crack-tips for in-plane and out-of-plane deformation. For in-plane deformation, it is shown that the crack propagation load and onset of unstable crack propagation can be predicted well with the lattice model, when comparing to analytically obtained results. For bending deformations, it is shown that an in-situ beam test where no stress relief holes were drilled can be used to find the critical concentrated bending strain that gives onset of crack propagation.

With the failure criteria for an ice plate in compression, tension, bending and strain concentrations near discontinuities, a complete set of failure criteria is derived that is required to simulate ice-sloping-structure interaction scenarios in multi-directional loading conditions. It is shown that the failure criteria have a minimal dependence on cell-size and orientation.

An L-beam test was simulated with the lattice model, where complex loading conditions of combined bending, shear and torsion were present as described in literature. The failure criteria derived for the lattice model, which use bending and torsion deformation to define the strain state in the lattice and compare it to the critical strain state, explain the locations of fracture observed in the field. In addition to bending and torsion, shear could have played a role in the onset of fracture. Out-of-plane shear failure cannot be accurately modelled with the lattice model and it is recommended to use a 3D model to study the L-beam tests if detailed failure simulation is required. The lattice model can give an indication of high shear loads and indicate the location of shear failure. In engineering applications shear failure is often not governing over bending and tensile failure, therefore the 2D plate model is appropriate in many applications, such as interaction between ice and sloping structures.

To further validate the lattice model, interaction between ice floes of different sizes and a sloping structure has been simulated and compared to results from basin tests. Fracture patterns are comparable between basin tests and lattice simulations, for different floe sizes. Both circumferential and splitting fractures, which were observed in the basin, were found in simulations with the lattice model. The load distribution at the interface between the structure and the ice has an influence on the velocity with which the load on the structure builds up and failure pattern that is observed. A simplified contact model was applied in the simulations. It is recommended to further develop the contact model, taking into account the locally deformed or damaged shape of the ice floe.

Failure loads in simulations with the lattice model are smaller than those measured in the basin. It is expected that the higher loading that was observed in the basin tests is to some extent associated with a likely underestimation of the tensile strength adopted in the numerical model and for the largest part with the rotating and sliding phases of the ice, where the ice pieces close to the structure are rotated to align with the structure's slope. Rotation and sliding of ice floes in combination with broken pieces of ice and rubble providing resistance to the rotation and sliding and applying further loads on the structure could result in the load levels that are observed in the basin tests. With the lattice model only the breaking phase was simulated and therefore significantly lower loading was found. To simulate ice clearance, it is recommended to link the lattice model to existing models, for example discrete element models, with proven success in simulation of ice rubbling and clearing. It is also recommended to measure tensile strength of the ice in basin tests.

The strain state of the lattice cells during the simulations of the basin tests was analysed and most of the deformations were in combined tension and compression. The Tensile-Compressive part of the failure diagram is most important in simulating interaction between ice and a conical structure. However, no measurement data is available to define this part of the failure envelope. It is recommended to focus ice strength measurements on combined tensile and compressive multi-axial loading conditions.

References

Adamson, R.M., Dempsey, J.P., 1998. Field-scale in-situ compliance of arctic first-year sea ice. J. Cold Reg. Eng. 12, 52–63.

Aksnes, V., 2010. A simplified interaction model for moored ships in level ice. Cold Reg. Sci. Technol. 63, 29–39.

Anderson, T.L., 1991. Fracture Mechanics Fundamentals and Applications. CRC Press, Inc.

Askar, A., 1985. Lattice Dynamical Foundations of Continuum Theories. World Scientific Publishing Co. Pte. Ltd.

Attar, M., Karrech, A., Regenauer-Lieb, K., 2014. Free vibration analysis of a cracked shear deformable beam on a two-parameter elastic foundation using a lattice spring model. J. Sound Vib. 333, 2359–2377.

Bolander, J.E., Shiraishi, T., Isogawa, Y., 1996. An adaptive procedure for fracture simulation in extensive lattice networks. Eng. Fract. Mech. 54, 325–334.

Bonnemaire, B., Serré, N., Lundamo, T., Fredriksen, A., Jensen, A., Gürtner, A., Teigen, S., 2014. Ice breaking and accumulation around a moored structure: Ice basin tests and numerical simulations, in: Society of Petroleum Engineers - Arctic Technology Conference 2014.

Brown, T.G., Tibbo, J.S., Tripathi, D., Obert, K., Shrestha, N., 2010. Extreme ice load events on the Confederation Bridge. Cold Reg. Sci. Technol. 60, 1–14.

Bruun, P.K., Gudmestad, O.T., 2006. A comparison of ice loads from level ice and ice ridges on sloping offshore structures calculated in accordance with different international and national standards, in: 25th International Conference on Offshore Mechanics and Arctic. pp. 655–665.

Bruun, P.K., Løset, S., Gürtner, A., Kuiper, G., Kokkinis, T., Arild, S., Hannus, H., 2011. Ice model testing of structures with a downward breaking cone, in: OMAE.

Chen, H., Lin, E., Jiao, Y., Liu, Y., 2014. A generalized 2D non-local lattice spring model for fracture simulation. Comput. Mech. 54, 1541–1558.

Comfort, G., Singh, S., Spencer, D., 1999. Evaluation of ice model test data for moored structures.

Coulomb, C.A., 1776. Essai sur une application des regles des maximis et minimis a quelquels problemesde statique relatifs, a la architecture. Mem. Acad. Roy. Div. Sav. 7, 343–387.

Croasdale, K., Jordaan, I., Verlaan, P., 2011. Offshore platforms and deterministic ice actions: Kashagan phase 2 development: North Caspian Sea, in: Proceedings of the 21st International Conference on Port and Ocean Engineering under Arctic Conditions.

Croasdale, K.R., 1980. “Ice forces on fixed, rigid structures,” Cold Regions Research and Engineering Laboratory Special Report No. 80-26.

Croasdale, K.R., Cammaert, A.B., 1994. An improved method for the calculation of ice loads on sloping structures in first-year ice. Hydrotechnical Constr. 28, 174–179.

Cusatis, G., Bažant, Z.P., Cedolin, L., 2003. Confinement-shear lattice model for concrete damage in tension and compression: I. theory. J. Eng. Mech. 129, 1439–1448.

Dai, H., Frantziskonis, G., 1994. Heterogeneity, spatial correlations, size effects and dissipated energy in brittle materials. Mech. Mater. 18, 103–118.

Dempsey, J.P., Adamson, R.M., Defranco, S.J., 1995. Fracture analysis of base-edge-cracked reverse-tapered plates. Int. J. Fract. 69, 281–294.

Dempsey, J.P., Adamson, R.M., Mulmule, S. V, 1999. Scale effects on the in-situ tensile strength and fracture of ice. Part II: First-year sea ice at Resolute, N.W.T. Int. J. Fract. 95, 325–345.

Donzé, F., Magnier, S.-A., 1995. Formulation of a 3-D numerical model of brittle bahaviour. Geophys. J. Int. 122, 790–802.

Dorival, O., Metrikine, A.V., Simone, A., 2008. A lattice model to simulate ice-structure interaction, in: ASME 2008 27th International Conference on Offshore Mechanics and Arctic Engineering, Jun 2008, Estoril, Portugal. pp. 989–996.

Edvardsson, S., Uesaka, T., 2010. System dynamics of the open-draw with web adhesion: particle approach. J. Appl. Mech. 77, 1–11.

Frankenstein, G., Garner, R., 1967. Equations for determining the brine volume of sea ice from - 0.5° to - 22.9 °C. J. Glaciol. 6, 943–944.

Frederking, R., Häusler, F.U., 1978. The flexural behaviour of ice from in situ cantilever beam tests, in: IAHR International Symposium on Ice Problems Luleå Sweden.

Frederking, R.M.W., Svec, O.J., 1985. Stress-relieving techniques for cantilever beam tests in an ice cover. Cold Reg. Sci. Technol. 11, 247–253.

Grassl, P., Bazant, Z.P., Cusatis, G., 2006. Lattice-cell approach to quasibrittle fracture modeling. Comput. Modelling Concr. Struct. 263–268.

Griffith, A.A., 1921. The Phenomena of Rupture and Flow in Solids. Philos. Trans. R. Soc. London. Ser. A, Contain. Pap. a Math. or Phys. Character 221, 163–198.

Hansen, E.H., Løset, S., 1999a. Modelling floating offshore units moored in broken ice : comparing simulations with ice tank tests. Cold Reg. Sci. Technol. 29, 107–119.

Hansen, E.H., Løset, S., 1999b. Modelling floating offshore units moored in broken ice : model description. Cold Reg. Sci. Technol. 29, 97–106.

Hendrikse, H., Ziemer, G., Owen, C., 2018. Experimental validation of a model for prediction of dynamic ice-structure interaction. Cold Reg. Sci. Technol. 151.

Herman, A., 2016. Discrete-Element bonded-particle Sea Ice model DESIgn , version 1.3a – model description and implementation. Geosci. Model Dev. 9, 1219–1241.

Herrmann, H., Hansen, A., Roux, S., 1989. Fracture of disordered, elastic lattices in two dimensions. Phys. Rev. B 39, 637–648.

Herrmann, H., Roux, S., 1990. Statistical models for the fracture of disordered media. Elsevier Science Publishers B.V.

Hoikkanen, J., 1985. Measurement and analysis of ice forces against a conical structure., in: The 8th International Conference on Port and Ocean Engineering under Arctic Conditions. pp. 1203–1220.

Hopkins, M.A., 2004. Discrete element modeling with dilated particles.

Hrennikoff, A.P., 1940. Plane stress and bending of plates by method of articulated framework. Massachusetts Institute of Technology.

HSVA, 2010a. JIP Phase II Ice Model Testing of Structures in Ice.

HSVA, 2010b. JIP Phase II Model test videos.

Iliescu, D., Schulson, E.M., 2004. The brittle compressive failure of freshwater columnar ice loaded biaxially. Acta Mater. 52, 5723–5735.

Irani, M.B., Timco, G.W., 1993. Ice loading on a multifaceted conical structure. Int. J. Offshore Polar Eng. 3.

ISO, 2010. Petroleum and natural gas industries — Arctic offshore structures.

Izumiyama, K., Irani, M.B., Timco, G.W., 1993. Computation of sheet ice forces on a faceted conical structure, in: The 12th International Conference on Port and Ocean Engineering under Arctic Conditions. pp. 517–526.

Ji, S., Di, S., Liu, S., 2015. Analysis of ice load on conical structure with discrete element method. Eng. Comput. Int. J. Comput. Eng. Softw. 32, 1121–1134.

Jirasek, M., Bazant, Z.P., 1995. Particle model for quasibrittle fracture and application to sea ice. J. Eng. Mech. 121, 1016–1025.

Kämäräinen, J., 2007. Theoretical investigation on the effect of fluid flow between the hull of a ship and ice floes on ice resistance in level ice.

Karulina, M., Karulin, E., Marchenko, A., 2013. Field investigations of first year ice mechanical properties in North-West Barents Sea, in: Proceedings of the International Conference on Port and Ocean Engineering under Arctic Conditions, POAC. Lulea University of Technology.

Kawai, T., 1978. New discrete models and their application to seismic response analysis of structures. Nucl. Eng. Des. 48, 207–229.

Kot, M., Nagahashi, H., 2017. Mass spring models with adjustable Poisson's ratio. Vis. Comput. 33, 283–291.

Lakes, R., 1991. Deformation mechanisms in negative Poisson's ratio materials: structural aspects. J. Mater. Sci. 26, 2287–2292.

Lau, M., 2001. A three dimensional discrete element simulation of ice sheet impacting a 60° conical structure, in: Proceedings of the 16th International Conference on Port and Ocean Engineering under Arctic Conditions. pp. 431–440.

Lau, M., 1999. An analysis of ice breaking pattern and ice piece size around sloping structures., in: Proc. 18th Int. Conf. on Offshore Mechanics and Arctic Engineering. pp. 199–207.

Li, F., Yue, Q., Shkhinek, K.N., Kärnä, T., 2003. A qualitative analysis of breaking length of sheet ice against conical structures, in: Proceedings of the 17th POAC Ice Symposium.

Lilja, V., Polojärvi, A., Tuhkuri, J., Paavilainen, J., 2017. Effective Tensile Strength of an Ice Sheet Using a Three-Dimensional FEM-DEM Approach Ville-Pekka, in: Proceedings of the 24th International Conference on Port and Ocean Engineering under Arctic Conditions June 11-16, 2017, Busan, Korea.

Lilliu, G., van Mier, J.G.M., 2007. On the relative use of micro-mechanical lattice analysis of 3-phase particle composites. Eng. Fract. Mech. 74, 1174–1189.

Liu, L., Ji, S., 2017. Bond model of dilated polyhedral DEM and its applications in sea ice simulation, in: Proceedings of the 24th International Conference on Port and Ocean Engineering under Arctic Conditions June 11-16, 2017, Busan, Korea.

Lu, W., 2014. Floe Ice-Sloping Structure Interactions (Doctoral Thesis).

Lu, W., Løset, S., 2010. JIP – Ice Model Testing of Structures In Ice; Phase II - Analysis of Test Results.

Lu, W., Løset, S., Shestov, A., Lubbad, R., 2015a. Design of a field test for measuring the fracture toughness of sea ice. Proc. 23rd Int. Conf. Port Ocean Eng. under Arct. Cond.

Lu, W., Lubbad, R., Løset, S., 2015b. In-plane fracture of an ice floe: A theoretical study on the splitting failure mode. Cold Reg. Sci. Technol. 110, 77–101.

Lubbad, R., Løset, S., 2011. A numerical model for real-time simulation of ship-ice interaction. Cold Reg. Sci. Technol. 65.

Marchenko, A., Cole, D., 2017. Three physical machanisms of wave energy dissipation in solid ice, in: Proceedings of the 24th International Conference on Port and Ocean Engineering under Arctic Conditions.

Metrikin, I., Kerkeni, S., Jochmann, P., Løset, S., 2015. Experimental and numerical investigation of dynamic positioning in level ice. J. Offshore Mech. Arct. Eng. 137.

Monette, L., Anderson, M.P., 1999. Elastic and fracture properties of the two-dimensional triangular and square lattices. Model. Simul. Mater. Sci. Eng. 2, 53–66.

Mulmule, S. V., Dempsey, J.P., 2000. LEFM size requirements for the fracture testing of sea ice. Int. J. Fract.

Mulmule, S. V., Dempsey, J.P., 1998. A viscoelastic fictitious cack model for the fracture of sea ice. Mech. Time-Dependent Mater. 1, 331–356.

Mulmule, S. V, Dempsey, J.P., 1999. Scale effects on sea ice fracture. Mech. Cohes.-Frict. Mater 4, 505–524.

Murdza, A., Marchenko, A., Sakharov, A., Chistyakov, P., Karulin, E., Karulina, M., 2016. Test with L-shaped cantilever beam for complex shear and bending strength, in: Proceedings of the 23rd IAHR International Symposium on Ice. pp. 1–9.

Nevel, D.E., 1992. Ice forces on cones from floes, in: Proceedings of IAHR '92, 11th International Symposium on Ice Problems 3. pp. 1391–1404.

Ostoja-starzewski, M., 2002. Lattice models in micromechanics. Appl. Mech. Rev. 55, 35–60.

Ostoja-Starzewski, M., 2008. Microstructural Randomness and Scaling in Mechanics of Materials. Chapman & Hall/CRC Press.

Ostoja-Starzewski, M., Sheng, P.Y., Jasiuk, I., 1997. Damage patterns and constitutive response of random matrix-inclusion composites. Eng. Fract. Mech. 58, 581–606.

Palmer, A., Croasdale, K., 2013. Arctic offshore engineering. World Scientific Publishing Co. Pte. Ltd., Singapore.

Paavilainen, J., Tuhkuri, J., Polojärvi, A., 2009. 2D combined finite-discrete element method to model multi-fracture of beam structures. Eng. Comput. Int. J. Comput. Aided Eng. Softw. 26, 578–598.

Potyondy, D.O., Cundall, P.A., 2004. A bonded-particle model for rock. Int. J. Rock Mech. Min. Sci. 41, 1329–1364.

Ralston, T.D., 1977. Ice force design considerations for conical offshore structures, in: POAC-77. pp. 741–752.

Rao, S., 2007. Vibration of continuous systems. John Wiley & Sons Inc.

Reddy, J.N., 1999. Theory and Analysis of Elastic Plates. Taylor & Francis.

Richter-Menge, J.A., Jones, K.F., 1993. The tensile strength of first-year sea ice. J. Glaciol.

Richter-Menge, J.A., Mcnutt, S.L., Overland, J.E., Kwok, R., 2002. Relating arctic pack ice stress and deformation under winter conditions. J. Geophys. Res. 107, 8040.

Ryghseter, D., Curth, A., Kildal, K., Mandfloen, P., Molden, T.K., Grevsgård, S.M., Murdza, A., 2015. Boat Cruise Report AT-211 Ice Mechanics, Loads on Structures and Instrumentation.

Sand, B., Fransson, L., 2006. Nonlinear finite element simulations of ice sheet forces on conical structures, in: 25th International Conference on Offshore Mechanics and Arctic Engineering. pp. 1–10.

Sayed, M., 1997. Discrete and lattice models of floating ice covers, in: The Seventh International Offshore and Polar Engineering Conference. pp. 428–433.

Sayed, M., Timco, G.W., 1998. A lattice model of ice failure. Ottawa.

Schlangen, E., Garboczi, E.J., 1997. Fracture simulations of concrete using lattice models: Computational aspects. Eng. Fract. Mech. 57, 319–332.

Schlangen, E., van Mier, J.G.M., 1992. Experimental and numerical analysis of micromechanisms of fracture of cement-based composites. Cem. Concr. Compos. 14, 105–118.

Schulson, E.M., 2001. Brittle failure of ice. Eng. Fract. Mech. 68, 1839–1887.

Schulson, E.M., Fortt, A.L., Iliescu, D., Renshaw, C.E., 2006. Failure envelope of first-year Arctic sea ice: The role of friction in compressive fracture. J. Geophys. Res. Ocean. 111, 1–13.

Schwarz, J., Frederking, R., Gavrillo, V., Petrov, I.G., Hirayama, K.-I., Mellor, M., Tryde, P., Vaudrey, K.D., 1981. Standardized testing methods for measuring mechanical properties of ice. Cold Reg. Sci. Technol. 4, 245–253.

Shi, W., Tan, X., Gao, Z., Moan, T., 2016. Numerical study of ice-induced loads and responses of a monopile-type offshore wind turbine in parked and operating conditions. Cold Reg. Sci. Technol. 123, 121–139.

Sih, G.C., 1977. Elastodynamic crack problems. Noordhoff International Publishing, Leiden.

Sodhi, D.S., 1995. Ice forces on a downward-breaking conical structure from partially consolidated rubble ice, in: 13th International Conference on Port and Ocean Engineering under Arctic Condition. pp. 72–83.

Suiker, A.S.J., Metrikine, A.V., de Borst, R., 2001a. Dynamic behaviour of a layer of discrete particles, part 1: analysis of body waves and eigenmodes. J. Sound Vib. 240, 1–18.

Suiker, A.S.J., Metrikine, A.V., de Borst, R., 2001b. Dynamic bahaviour of a layer of discrete particles, part 2: response to a uniformly moving, harmonically vibrating load. J. Sound Vib. 240, 19–39.

Suiker, A.S.J., Metrikine, A.V., de Borst, R., 2001c. Comparison of wave propagation characteristics of the Cosserat continuum model and corresponding discrete lattice models. Int. J. Solids Struct. 38, 1563–1583.

Timco, G.W., Weeks, W.F., 2010. A review of the engineering properties of sea ice. Cold Reg. Sci. Technol. 60.

Valanto, P., 2001. The Resistance of Ships in Level Ice. SNAME Trans. 109, 53–83.

van den Berg, M., 2016. A 3-D Random Lattice Model of Sea Ice, in: Arctic Technology Conference.

van Mier, J.G.M., 1986. Multiaxial strain-softening of concrete. Mater. Struct. 19, 179–190.

van Mier, J.G.M., van Vliet, M.R.A., Wang, T.K., 2002. Fracture mechanisms in particle composites: Statistical aspects in lattice type analysis. Mech. Mater. 34, 705–724.

van Vliet, R., Metrikine, A.V., 2017a. Derivation and verification of a lattice model for bending vibration of a plate. J. Appl. Math. Mech.

van Vliet, R., Metrikine, A.V., 2017b. Simulating Interaction Between Level Ice and Conical Structures with a 2D Lattice Model, in: Proceedings of the 24th International Conference on Port and Ocean Engineering under Arctic Conditions. pp. POAC17-057.

Vaudrey, K.D., 1977. Ice engineering: Study of related properties of floating sea-ice sheets and summary of elastic and viscoelastic analysis. Port Hueneme, CA.

Weiss, J., Schulson, E.M., Stern, H.L., 2007. Sea ice rheology from in-situ , satellite and laboratory observations : Fracture and friction. Earth Planet. Sci. Lett. 255, 1–8.

Westergaard, H.M., 1939. Bearing Pressures and Cracks. J. Appl. Mech. 61, A-49-A-53.

Wille, S.F., Kuiper, G.L., Metrikine, A.V., 2011. On the dynamic interaction between drifting level ice and moored downward conical structures: A critical assessment of the applicability of a beam model for the ice, in: Proceedings of the ASME 2011 30th International Conference on Ocean, Offshore and Arctic Engineering.

Woźniak, C., 1970. Surface Lattice Structures (in Polish). PWN - Polish Sci. Publ., Warsaw.

Wright, B., 2001. Ice loads on the Kulluk in managed ice conditions, in: Proceedings of the 16th International Conference on Port and Ocean Engineering under Arctic Conditions. p. Vol 2. pp 553-566.

Zhao, G., 2017. Developing a four-dimensional lattice spring model for mechanical responses of solids. Comput. Methods Appl. Mech. Eng. 315, 881–895.

Zubelewicz, A., Bažant, Z.P., 1987. Interface Element Modeling of Fracture in Aggregate Composites. J. Eng. Mech. 113, 1619–1630.

Appendix 1: analytical solution for the response of a rectangular plate to sinusoidal loading

The analytical solution of the rectangular plate, supported by a Kelvin foundation over the complete area, simply supported at the edges and loaded by a sinusoidal point load in out-of-plane direction is derived in this appendix.

Applying Navier's method, w φ_x and φ_y are represented in the form of a double trigonometric series which satisfy the boundary conditions at all-time. These series are substituted in equation system (2.27) - (2.29):

$$w(x,y,t)=e^{i\omega t}\sum_{m=1}^{\infty}\sum_{n=1}^{\infty}A_w(m,n)\sin\left(\frac{m\pi x}{L_x}\right)\sin\left(\frac{n\pi y}{L_y}\right) \tag{A.1.1}$$

$$\varphi_x(x,y,t)=e^{i\omega t}\sum_{m=1}^{\infty}\sum_{n=1}^{\infty}A_{\varphi_x}(m,n)\cos\left(\frac{m\pi x}{L_x}\right)\sin\left(\frac{n\pi y}{L_y}\right) \tag{A.1.2}$$

$$\varphi_y(x,y,t)=e^{i\omega t}\sum_{m=1}^{\infty}\sum_{n=1}^{\infty}A_{\varphi_y}(m,n)\sin\left(\frac{m\pi x}{L_x}\right)\cos\left(\frac{n\pi y}{L_y}\right) \tag{A.1.3}$$

which results in the following system of equations:

$$\begin{aligned}&\left(-\rho h\omega^2+i\omega c_s+k_s\right)e^{i\omega t}\sum_{m=1}^{\infty}\sum_{n=1}^{\infty}A_w(m,n)\sin\left(\frac{m\pi x}{L_x}\right)\sin\left(\frac{n\pi y}{L_y}\right)\\&=k^2Gh\left(1+\alpha\frac{\partial}{\partial t}\right)\left(\frac{\partial^2 w}{\partial x^2}+\frac{\partial^2 w}{\partial y^2}+\frac{\partial\varphi_x}{\partial x}+\frac{\partial\varphi_y}{\partial y}\right)+\mathrm{Re}\left(Fe^{i\omega t}\right)\delta(x-x_0)\delta(y-y_0),\end{aligned} \tag{A.1.4}$$

with:

$$\frac{\partial^2 w}{\partial x^2}=-e^{i\omega t}\sum_{m=1}^{\infty}\sum_{n=1}^{\infty}\left(\frac{m\pi}{L_x}\right)^2 A_w(m,n)\sin\left(\frac{m\pi x}{L_x}\right)\sin\left(\frac{n\pi y}{L_y}\right)$$

$$\frac{\partial^2 w}{\partial y^2}=-e^{i\omega t}\sum_{m=1}^{\infty}\sum_{n=1}^{\infty}\left(\frac{n\pi}{L_y}\right)^2 A_w(m,n)\sin\left(\frac{m\pi x}{L_x}\right)\sin\left(\frac{n\pi y}{L_y}\right)$$

$$\frac{\partial\varphi_x}{\partial x}=e^{i\omega t}\sum_{m=1}^{\infty}\sum_{n=1}^{\infty}\left(\frac{m\pi}{L_x}\right)A_{\varphi_x}(m,n)\sin\left(\frac{m\pi x}{L_x}\right)\sin\left(\frac{n\pi y}{L_y}\right)$$

$$\frac{\partial\varphi_y}{\partial x}=e^{i\omega t}\sum_{m=1}^{\infty}\sum_{n=1}^{\infty}\left(\frac{n\pi}{L_y}\right)A_{\varphi_y}(m,n)\sin\left(\frac{m\pi x}{L_x}\right)\sin\left(\frac{n\pi y}{L_y}\right)$$

$$\frac{\rho h^3}{12}\ddot{\varphi}_x = \frac{D}{2}\left(1+\alpha\frac{\partial}{\partial t}\right)\left[\left(1-\nu\right)\left(\frac{\partial^2\varphi_x}{\partial x^2}+\frac{\partial^2\varphi_x}{\partial y^2}\right)+\left(1+\nu\right)\left(\frac{\partial^2\varphi_x}{\partial x^2}+\frac{\partial^2\varphi_y}{\partial x\partial y}\right)\right]$$

$$-k^2Gh\left(1+\alpha\frac{\partial}{\partial t}\right)\left(\varphi_x+\frac{\partial w}{\partial x}\right), \tag{A.1.5}$$

with:

$$\ddot{\varphi}_x = -\omega^2 e^{i\omega t}\sum_{m=1}^{\infty}\sum_{n=1}^{\infty}A_{\varphi_x}(m,n)\cos\left(\frac{m\pi x}{L_x}\right)\sin\left(\frac{n\pi y}{L_y}\right)$$

$$\frac{\partial w}{\partial x} = e^{i\omega t}\sum_{m=1}^{\infty}\sum_{n=1}^{\infty}-\left(\frac{m\pi}{L_x}\right)A_w(m,n)\cos\left(\frac{m\pi x}{L_x}\right)\sin\left(\frac{n\pi y}{L_y}\right)$$

$$\varphi_x(x,y,t) = e^{i\omega t}\sum_{m=1}^{\infty}\sum_{n=1}^{\infty}A_{\varphi_x}(m,n)\cos\left(\frac{m\pi x}{L_x}\right)\sin\left(\frac{n\pi y}{L_y}\right)$$

$$\frac{\partial^2\varphi_x}{\partial x^2} = e^{i\omega t}\sum_{m=1}^{\infty}\sum_{n=1}^{\infty}-\left(\frac{m\pi}{L_x}\right)^2 A_{\varphi_x}(m,n)\cos\left(\frac{m\pi x}{L_x}\right)\sin\left(\frac{n\pi y}{L_y}\right)$$

$$\frac{\partial^2\varphi_x}{\partial y^2} = e^{i\omega t}\sum_{m=1}^{\infty}\sum_{n=1}^{\infty}-\left(\frac{n\pi}{L_y}\right)^2 A_{\varphi_x}(m,n)\cos\left(\frac{m\pi x}{L_x}\right)\sin\left(\frac{n\pi y}{L_y}\right)$$

$$\frac{\partial^2\varphi_y}{\partial x\partial y} = e^{i\omega t}\sum_{m=1}^{\infty}\sum_{n=1}^{\infty}-\left(\frac{m\pi}{L_x}\right)\left(\frac{n\pi}{L_y}\right)A_{\varphi_y}(m,n)\cos\left(\frac{m\pi x}{L_x}\right)\sin\left(\frac{n\pi y}{L_y}\right)$$

$$\frac{\rho h^3}{12}\ddot{\varphi}_y = \frac{D}{2}\left(1+\alpha\frac{\partial}{\partial t}\right)\left[(1-\nu)\left(\frac{\partial^2\varphi_y}{\partial x^2}+\frac{\partial^2\varphi_y}{\partial y^2}\right)+(1+\nu)\left(\frac{\partial^2\varphi_x}{\partial x\partial y}+\frac{\partial^2\varphi_y}{\partial y^2}\right)\right]$$
$$-k^2Gh\left(1+\alpha\frac{\partial}{\partial t}\right)\left(\varphi_y+\frac{\partial w}{\partial y}\right), \tag{A.1.6}$$

with:

$$\ddot{\varphi}_y = -\omega^2 e^{i\omega t}\sum_{m=1}^{\infty}\sum_{n=1}^{\infty}A_{\varphi_y}(m,n)\sin\left(\frac{m\pi x}{L_x}\right)\cos\left(\frac{n\pi y}{L_y}\right)$$

$$\frac{\partial^2\varphi_y}{\partial x^2} = e^{i\omega t}\sum_{m=1}^{\infty}\sum_{n=1}^{\infty}-\left(\frac{m\pi}{L_x}\right)^2 A_{\varphi_y}(m,n)\sin\left(\frac{m\pi x}{L_x}\right)\cos\left(\frac{n\pi y}{L_y}\right)$$

$$\frac{\partial^2\varphi_y}{\partial y^2} = e^{i\omega t}\sum_{m=1}^{\infty}\sum_{n=1}^{\infty}-\left(\frac{n\pi}{L_y}\right)^2 A_{\varphi_y}(m,n)\sin\left(\frac{m\pi x}{L_x}\right)\cos\left(\frac{n\pi y}{L_y}\right)$$

$$\frac{\partial^2\varphi_x}{\partial x\partial y} = e^{i\omega t}\sum_{m=1}^{\infty}\sum_{n=1}^{\infty}-\left(\frac{m\pi}{L_x}\right)\left(\frac{n\pi}{L_y}\right)A_{\varphi_x}(m,n)\sin\left(\frac{m\pi x}{L_x}\right)\cos\left(\frac{n\pi y}{L_y}\right)$$

$$\frac{\partial^2\varphi_y}{\partial y^2} = e^{i\omega t}\sum_{m=1}^{\infty}\sum_{n=1}^{\infty}-\left(\frac{n\pi}{L_y}\right)^2 A_{\varphi_y}(m,n)\sin\left(\frac{m\pi x}{L_x}\right)\cos\left(\frac{n\pi y}{L_y}\right)$$

$$\varphi_y = e^{i\omega t}\sum_{m=1}^{\infty}\sum_{n=1}^{\infty}A_{\varphi_y}(m,n)\sin\left(\frac{m\pi x}{L_x}\right)\cos\left(\frac{n\pi y}{L_y}\right)$$

$$\frac{\partial w}{\partial y} = e^{i\omega t}\sum_{m=1}^{\infty}\sum_{n=1}^{\infty}-\left(\frac{n\pi}{L_y}\right)A_w(m,n)\sin\left(\frac{m\pi x}{L_x}\right)\cos\left(\frac{n\pi y}{L_y}\right)$$

Multiplying both left-hand and right-hand side of the system of equations with

$$\sin\left(\frac{m_0\pi x}{L_x}\right)\sin\left(\frac{n_0\pi y}{L_y}\right), \tag{A.1.7}$$

integrating over the interval $\left[0,L_x\right]$ with respect to x and $\left[0,L_y\right]$ with respect to y gives, using the orthogonality principle:

$$\frac{1}{4}L_xL_y\left(-\rho h\omega^2+i\omega c_s+k_s\right)A_w(m_0,n_0)=$$

$$\frac{1}{4}L_xL_yk^2Gh\left(1+\alpha i\omega\right)\cdot$$

$$\left(-\left(\left(\frac{m_0\pi}{L_x}\right)^2+\left(\frac{n_0\pi}{L_y}\right)^2\right)A_w(m_0,n_0)+\left(\frac{m_0\pi}{L_x}\right)A_{\varphi_x}(m_0,n_0)+\left(\frac{n_0\pi}{L_y}\right)A_{\varphi_y}(m_0,n_0)\right) \tag{A.1.8}$$

$$+F\sin\left(\frac{m_0\pi x_0}{L_x}\right)\sin\left(\frac{n_0\pi y_0}{L_y}\right)$$

$$-\frac{\rho h^3}{12}\omega^2A_{\varphi_x}(m_0,n_0)= \tag{A.1.9}$$

$$\frac{D}{2}(1+\alpha i\omega)\left[(-1+\nu)A_{\varphi_x}(m_0,n_0)\left(\left(\frac{m_0\pi}{L_x}\right)^2+\left(\frac{n_0\pi}{L_y}\right)^2\right)\right.$$

$$\left.-(1+\nu)\left(\left(\frac{m_0\pi}{L_x}\right)^2A_{\varphi_x}(m_0,n_0)+\left(\frac{m_0\pi}{L_x}\right)\left(\frac{n_0\pi}{L_y}\right)A_{\varphi_y}(m_0,n_0)\right)\right]$$

$$-k^2Gh\left(1+\alpha i\omega\right)\left(A_{\varphi_x}(m_0,n_0)-\left(\frac{m_0\pi}{L_x}\right)A_w(m_0,n_0)\right)$$

$$-\frac{\rho h^3}{12}\omega^2A_{\varphi_y}(m_0,n_0)= \tag{A.1.10}$$

$$\frac{D}{2}(1+\alpha i\omega)\left[(-1+\nu)A_{\varphi_y}(m_0,n_0)\left(\left(\frac{m_0\pi}{L_x}\right)^2+\left(\frac{n_0\pi}{L_y}\right)^2\right)\right.$$

$$\left.-(1+\nu)\left(\left(\frac{n_0\pi}{L_y}\right)^2A_{\varphi_y}(m_0,n_0)+\left(\frac{m_0\pi}{L_x}\right)\left(\frac{n_0\pi}{L_y}\right)A_{\varphi_x}(m_0,n_0)\right)\right]$$

$$-k^2Gh\left(1+\alpha i\omega\right)\left(A_{\varphi_y}(m_0,n_0)-\left(\frac{n_0\pi}{L_y}\right)A_w(m_0,n_0)\right)$$

From equations (A.1.8) to (A.1.10) $A_w\left(m,n\right)$, $A_{\varphi_x}\left(m,n\right)$ and $A_{\varphi_y}\left(m,n\right)$ are determined.

Appendix 2: Deformations of a lattice cell in multi-axial in-plane loading

A lattice cell with orientation α relative to the orientation of the bi-axial in-plane loading σ_{xx} in x- and σ_{yy} in y-direction in a square plate is analysed, as depicted in Figure 4-3. The loads on the lattice cell are shown in Figure A2-1 and applied as nodal loads to the lattice cell, as depicted in Figure A2-2.

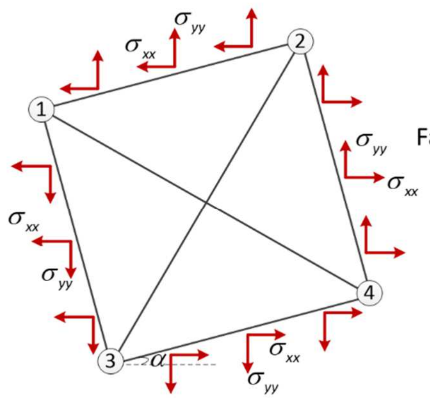

Figure A2-1: Tensile loads working on the lattice cell

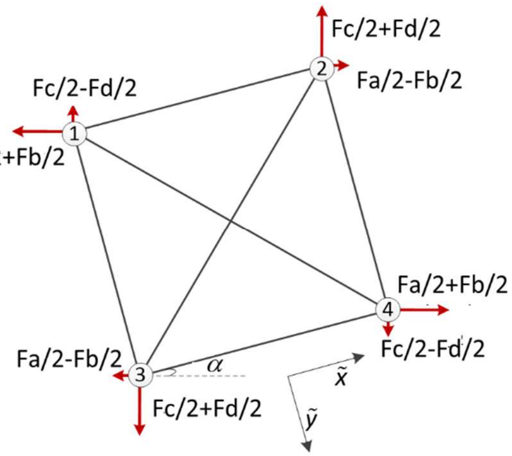

Figure A2-2: Tensile loads transferred to the nodes of the lattice cell

The nodal loads follow from the loads on the lattice cell by multiplying the stress working at the lattice cell location with the area of the lattice cell that faces in the direction of that stress:

$$F_A = \sigma_{xx} hd \cos(\alpha) \tag{A.2.1}$$

$$F_B = \sigma_{xx} hd \sin(\alpha) \tag{A.2.2}$$

$$F_C = \sigma_{yy} hd \cos(\alpha) \tag{A.2.3}$$

$$F_D = \sigma_{yy} hd \sin(\alpha) \tag{A.2.4}$$

The nodal loads are equally distributed over the masses at both ends of the connection. The displacements of the lattice cell nodes are found by solving the equilibrium of external loads on the lattice cell and lattice cell deformation:

$$\begin{aligned}&\frac{F_A+F_B}{2}\cos(\alpha)-\frac{F_C-F_D}{2}\sin(\alpha)\\&=\frac{1}{2}K_{n;axi}\left(u_{\tilde{x},2}-u_{\tilde{x},1}\right)+\frac{1}{2}K_{\text{n;dia}}\left(u_{\tilde{x},4}-u_{\tilde{x}1}+u_{\tilde{y},4}-u_{\tilde{y},1}\right)+\frac{1}{2}K_{\text{s};axi}\left(u_{\tilde{x},3}-u_{\tilde{x},1}\right)\end{aligned} \tag{A.2.5}$$

$$\begin{aligned}&\frac{F_A+F_B}{2}\sin(\alpha)+\frac{F_C-F_D}{2}\cos(\alpha)\\&=\frac{1}{2}K_{n;axi}\left(u_{\tilde{y},3}-u_{\tilde{y},1}\right)+\frac{1}{2}K_{\text{n;dia}}\left(u_{\tilde{x},4}-u_{\tilde{x},1}+u_{\tilde{x},4}-u_{\tilde{x},1}\right)+\frac{1}{2}K_{\text{s};axi}\left(u_{\tilde{y},2}-u_{\tilde{y},1}\right)\end{aligned} \tag{A.2.6}$$

$$\begin{aligned}&\frac{F_A-F_B}{2}\cos(\alpha)+\frac{F_C+F_D}{2}\sin(\alpha)\\&=\frac{1}{2}K_{n;axi}\left(u_{\tilde{x},2}-u_{\tilde{x},1}\right)+\frac{1}{2}K_{\text{n;dia}}\left(u_{\tilde{x},2}-u_{\tilde{x},3}-u_{\tilde{y},2}+u_{\tilde{y},3}\right)-\frac{1}{2}K_{\text{s};axi}\left(u_{\tilde{x},4}-u_{\tilde{x},2}\right)\end{aligned} \tag{A.2.7}$$

$$\begin{aligned}&\frac{F_A-F_B}{2}\sin(\alpha)-\frac{F_C+F_D}{2}\cos(\alpha)\\&=-\frac{1}{2}K_{n;axi}\left(u_{\tilde{y},4}-u_{\tilde{y},2}\right)-\frac{1}{2}K_{\text{n;dia}}\left(u_{\tilde{x},2}-u_{\tilde{x},3}-u_{\tilde{y},2}+u_{\tilde{y},3}\right)+\frac{1}{2}K_{\text{s};axi}\left(u_{\tilde{y},2}-u_{\tilde{y},1}\right)\end{aligned} \tag{A.2.8}$$

$$\begin{aligned}&\frac{F_A-F_B}{2}\cos(\alpha)+\frac{F_C+F_D}{2}\sin(\alpha)\\&=\frac{1}{2}K_{n;axi}\left(u_{\tilde{x},4}-u_{\tilde{x},3}\right)+\frac{1}{2}K_{\text{n;dia}}\left(u_{\tilde{x},2}-u_{\tilde{x},3}-u_{\tilde{y},2}+u_{\tilde{y},3}\right)-\frac{1}{2}K_{\text{s};axi}\left(u_{\tilde{x},3}-u_{\tilde{x},1}\right)\end{aligned} \tag{A.2.9}$$

$$\begin{aligned}&\frac{F_A-F_B}{2}\sin(\alpha)-\frac{F_C+F_D}{2}\cos(\alpha)\\&=\frac{1}{2}K_{n;axi}\left(u_{\tilde{y},1}-u_{\tilde{y},3}\right)-\frac{1}{2}K_{\text{n;dia}}\left(u_{\tilde{x},2}-u_{\tilde{x},3}-u_{y,2}+u_{y,3}\right)+\frac{1}{2}K_{\text{s};axi}\left(u_{\tilde{y},4}-u_{\tilde{y},3}\right)\end{aligned} \tag{A.2.10}$$

$$\begin{aligned}&\frac{F_A+F_B}{2}\cos(\alpha)-\frac{F_C-F_D}{2}\sin(\alpha)\\&=\frac{1}{2}K_{n;axi}\left(u_{\tilde{x},4}-u_{\tilde{x},3}\right)+\frac{1}{2}K_{\text{n;dia}}\left(u_{\tilde{x},4}-u_{\tilde{x},1}+u_{\tilde{y},4}+u_{\tilde{y},1}\right)+\frac{1}{2}K_{\text{s};axi}\left(u_{\tilde{x},4}-u_{\tilde{x},2}\right)\end{aligned} \tag{A.2.11}$$

$$\begin{aligned}&\frac{F_A+F_B}{2}\sin(\alpha)+\frac{F_C-F_D}{2}\cos(\alpha)\\&=\frac{1}{2}K_{n;axi}\left(u_{\tilde{y},4}-u_{\tilde{y},2}\right)+\frac{1}{2}K_{\text{n;dia}}\left(u_{\tilde{x},4}-u_{\tilde{x},1}+u_{\tilde{y},4}-u_{\tilde{y},1}\right)+\frac{1}{2}K_{\text{s};axi}\left(u_{\tilde{y},4}-u_{\tilde{y},3}\right)\end{aligned} \tag{A.2.12}$$

The lattice cells are numbered 1-2 on the top row and 3-4 on the bottom row as shown in Figure A2-2. $u_{\tilde{x},i}$ and $u_{\tilde{y},i}$ are the deformation in $\tilde{x}$ - and $\tilde{y}$ - direction of node *i* respectively, in the local axis system, which is orientated under an angle α with respect to the global axis system. The strain in $\tilde{x}$ - and $\tilde{y}$ -direction over the axial connections is normalised by the cell size. Parallel connections have the same strain in the applied loading conditions. This gives:

$$\varepsilon_{11} = \frac{u_{\tilde{x},2} - u_{\tilde{x},1}}{d} = \frac{u_{\tilde{x},4} - u_{\tilde{x},3}}{d} \tag{A.2.13}$$

$$\varepsilon_{12} = \frac{u_{\tilde{y},2} - u_{\tilde{y},1}}{d} = \frac{u_{\tilde{y},4} - u_{\tilde{y},3}}{d} \tag{A.2.14}$$

$$\varepsilon_{22} = \frac{u_{\tilde{y},3} - u_{\tilde{y},1}}{d} = \frac{u_{\tilde{y},4} - u_{\tilde{y},2}}{d} \tag{A.2.15}$$

$$\varepsilon_{21} = \frac{u_{\tilde{x},3} - u_{\tilde{x},1}}{d} = \frac{u_{\tilde{x},4} - u_{\tilde{x},2}}{d} \tag{A.2.16}$$

where ε_{11} and ε_{22} are the normalised axial strain and ε_{12} and ε_{21} are the normalised shear strain in $\tilde{x}$ - and $\tilde{y}$ -direction respectively. The strain in the diagonal connections is evaluated as follows:

$$\varepsilon_{D1} = \frac{\frac{\sqrt{2}}{2}\left(u_{\tilde{x},4} - u_{\tilde{x},1} + u_{\tilde{y},4} - u_{\tilde{y},1}\right)}{\sqrt{2}d} \tag{A.2.17}$$

$$\varepsilon_{D2} = \frac{\frac{\sqrt{2}}{2}\left(u_{\tilde{x},2} - u_{\tilde{x},3} - u_{\tilde{y},2} + u_{\tilde{y},3}\right)}{\sqrt{2}d} \tag{A.2.18}$$

where ε_{D1} is the strain in the connection between node 1 and node 4 and ε_{D2} is the strain in the connection between node 2 and node 3.

Appendix 3: Deformations of a lattice cell in multi-axial bending

A lattice cell with orientation α relative to the x-axis of a plate in bi-axial bending is analysed, as depicted in Figure 4-9. The bending loads on the lattice cell are shown in Figure A3-1 and translated to nodal loads in the lattice, as depicted in Figure A3-2.

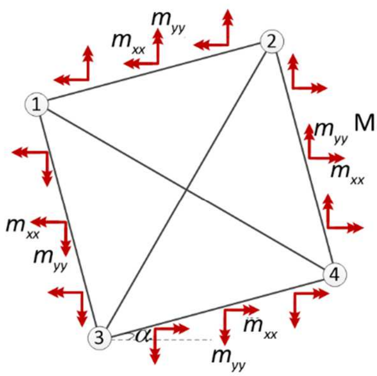

Figure A3-1: Bending and shear loads working on the lattice cell

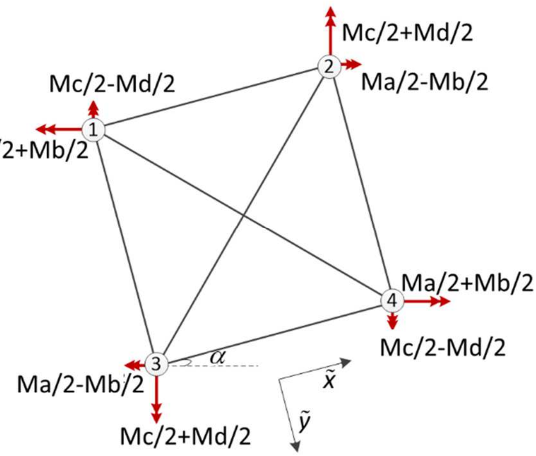

Figure A3-2: Bending and shear loads transferred to the nodes of the lattice cell

m_{xx} and m_{yy} are the global bending moment per unit length of the plate in x- and y-direction respectively. α is the orientation of the lattice cell relative to the x-axis. M_A, M_B, M_C and M_D are the bending moments working on the lattice cells at different connections and directions, as depicted in Figure A3-2. These are evaluated as follows:

$$M_A = m_{xx} d \cos(\alpha) \tag{A.3.1}$$

$$M_B = m_{xx} d \sin(\alpha) \tag{A.3.2}$$

$$M_C = m_{yy} d \cos(\alpha) \tag{A.3.3}$$

$$M_D = m_{yy} d \sin(\alpha) \tag{A.3.4}$$

The rotation of the lattice nodes can be found by solving the equilibrium bending loads for the four nodes of the lattice cell:

$$\frac{M_A+M_B}{2}\cos(\alpha)-\frac{M_C+M_D}{2}\sin(\alpha)=\frac{1}{2}G_{r;axi}\left(\varphi_{\tilde{x},2}-\varphi_{\tilde{x},1}\right)$$
$$+\frac{1}{2}G_{r;\text{dia}}\left(\varphi_{\tilde{x},4}-\varphi_{\tilde{x},1}+\varphi_{\tilde{y},4}-\varphi_{\tilde{y},1}\right) \quad \text{(A.3.5)}$$
$$+\frac{1}{2}G_{\text{t};axi}\left(\varphi_{\tilde{x},1}-\varphi_{\tilde{x},3}\right)+\frac{1}{4}K_{\text{s};axi}d\left(w_1-w_2-\varphi_{\tilde{x},2}\frac{d}{2}-\varphi_{\tilde{x},1}\frac{d}{2}\right)$$

$$\frac{M_A+M_B}{2}\sin(\alpha)+\frac{M_C-M_D}{2}\cos(\alpha)=\frac{1}{2}G_{r;axi}\left(\varphi_{\tilde{y},3}-\varphi_{\tilde{y},1}\right)$$
$$+\frac{1}{2}G_{r;\text{dia}}\left(\varphi_{\tilde{x},4}-\varphi_{\tilde{x},1}+\varphi_{\tilde{y},4}-\varphi_{\tilde{y},1}\right)+\frac{1}{2}G_{\text{t};axi}\left(\varphi_{\tilde{y}1}-\varphi_{\tilde{y},2}\right) \quad \text{(A.3.6)}$$
$$+\frac{1}{4}K_{\text{s};axi}d\left(w_1-w_3-\varphi_{\tilde{y},3}\frac{d}{2}-\varphi_{\tilde{y},1}\frac{d}{2}\right)$$

$$\frac{M_A-M_B}{2}\cos(\alpha)+\frac{M_C+M_D}{2}\sin(\alpha)=\frac{1}{2}G_{r;axi}\left(\varphi_{\tilde{x},2}-\varphi_{\tilde{x},1}\right)$$
$$+\frac{1}{2}G_{r;\text{dia}}\left(\varphi_{\tilde{x},2}-\varphi_{\tilde{x},3}+\varphi_{\tilde{y},3}-\varphi_{\tilde{y},2}\right)+\frac{1}{2}G_{\text{t};axi}\left(\varphi_{\tilde{x},4}-\varphi_{\tilde{x},2}\right) \quad \text{(A.3.7)}$$
$$+\frac{1}{4}K_{\text{s};axi}d\left(w_2-w_1+\varphi_{\tilde{x},2}\frac{d}{2}+\varphi_{\tilde{x},1}\frac{d}{2}\right)$$

$$\frac{M_A-M_B}{2}\sin(\alpha)+\frac{M_C+M_D}{2}\cos(\alpha)=\frac{1}{2}G_{r;axi}\left(\varphi_{\tilde{y},4}-\varphi_{\tilde{y},2}\right)$$
$$+\frac{1}{2}G_{r;\text{dia}}\left(\varphi_{\tilde{x},2}-\varphi_{\tilde{x},3}+\varphi_{\tilde{y},3}-\varphi_{\tilde{y},2}\right) \quad \text{(A.3.8)}$$
$$+\frac{1}{2}G_{\text{t};axi}\left(\varphi_{\tilde{y},2}-\varphi_{\tilde{y},1}\right)+\frac{1}{4}K_{\text{s};axi}d\left(w_2-w_4-\varphi_{\tilde{y},4}\frac{d}{2}-\varphi_{\tilde{y},2}\frac{d}{2}\right)$$

$$\frac{M_A-M_B}{2}\cos(\alpha)+\frac{M_C+M_D}{2}\sin(\alpha)=\frac{1}{2}G_{r;axi}\left(\varphi_{\tilde{x},4}-\varphi_{\tilde{x},3}\right)$$
$$+\frac{1}{2}G_{r;\text{dia}}\left(\varphi_{\tilde{x},2}-\varphi_{\tilde{x},3}+\varphi_{\tilde{y},3}-\varphi_{\tilde{y},2}\right) \quad \text{(A.3.9)}$$
$$+\frac{1}{2}G_{\text{t};axi}\left(\varphi_{\tilde{x},3}-\varphi_{\tilde{x},1}\right)+\frac{1}{4}K_{\text{s};axi}d\left(w_3-w_4-\varphi_{\tilde{x},3}\frac{d}{2}-\varphi_{\tilde{x},4}\frac{d}{2}\right)$$

$$-\frac{M_A-M_B}{2}\sin(\alpha)+\frac{M_C+M_D}{2}\cos(\alpha)=\frac{1}{2}G_{r;axi}\left(\varphi_{\tilde{y},3}-\varphi_{\tilde{y},1}\right)$$
$$+\frac{1}{2}G_{r;\text{dia}}\left(\varphi_{\tilde{x},2}-\varphi_{\tilde{x},3}+\varphi_{\tilde{y},3}-\varphi_{\tilde{y},2}\right) \quad \text{(A.3.10)}$$
$$+\frac{1}{2}G_{\text{t};axi}\left(\varphi_{\tilde{y},4}-\varphi_{\tilde{y},3}\right)+\frac{1}{4}K_{\text{s};axi}d\left(w_3-w_1+\varphi_{\tilde{y},3}\frac{d}{2}+\varphi_{\tilde{y},1}\frac{d}{2}\right)$$

$$\frac{M_A + M_B}{2}\cos(\alpha) - \frac{M_C - M_D}{2}\sin(\alpha) = \frac{1}{2}G_{r;axi}\left(\varphi_{\tilde{x},4} - \varphi_{\tilde{x},3}\right)$$
$$+\frac{1}{2}G_{r;\text{dia}}\left(\varphi_{\tilde{x},4} - \varphi_{\tilde{x},1} + \varphi_{\tilde{y},4} - \varphi_{\tilde{y},1}\right) \tag{A.3.11}$$
$$+\frac{1}{2}G_{\text{t};axi}\left(\varphi_{\tilde{x},2} - \varphi_{\tilde{x},4}\right) + \frac{1}{4}K_{\text{s};axi}d\left(w_4 - w_3 + \varphi_{\tilde{x},3}\frac{d}{2} + \varphi_{\tilde{x},4}\frac{d}{2}\right)$$

$$\frac{M_A + M_B}{2}\sin(\alpha) + \frac{M_C - M_D}{2}\cos(\alpha) = \frac{1}{2}G_{r;axi}\left(\varphi_{\tilde{y},4} - \varphi_{\tilde{y},2}\right)$$
$$+\frac{1}{2}G_{r;\text{dia}}\left(\varphi_{\tilde{x},4} - \varphi_{\tilde{x},1} + \varphi_{\tilde{y},4} - \varphi_{\tilde{y},1}\right) \tag{A.3.12}$$
$$+\frac{1}{2}G_{\text{t};axi}\left(\varphi_{\tilde{y},3} - \varphi_{\tilde{y},4}\right) + \frac{1}{4}K_{\text{s};axi}d\left(w_4 - w_2 + \varphi_{\tilde{y},4}\frac{d}{2} + \varphi_{\tilde{y},2}\frac{d}{2}\right)$$

The lattice cells are numbered 1-2 on the top row and 3-4 on the bottom row as shown in Figure A3-2. $\varphi_{\tilde{x},i}$ and $\varphi_{\tilde{y},i}$ are the deformation in $\tilde{x}-$ and $\tilde{y}-$ direction of node i respectively, in the local axis system, which is orientated under an angle α with respect to the global (x, y) axes system. In this loading condition the deformation in the parallell connections is the same. The resulting rotational deformation in the lattice connections is normalized by the mesh size:

$$\eta_{11} = \frac{\varphi_{\tilde{x},2} - \varphi_{\tilde{x},1}}{d} = \frac{\varphi_{\tilde{x},4} - \varphi_{\tilde{x},3}}{d} \tag{A.3.13}$$

$$\eta_{22} = \frac{\varphi_{\tilde{y},3} - \varphi_{\tilde{y},1}}{d} = \frac{\varphi_{\tilde{y},4} - \varphi_{\tilde{y},2}}{d} \tag{A.3.14}$$

The same is done for the torsional deformations:

$$\eta_{12} = \frac{\varphi_{\tilde{y},2} - \varphi_{\tilde{y},1}}{d} = \frac{\varphi_{\tilde{y},4} - \varphi_{\tilde{y},3}}{d} \tag{A.3.15}$$

$$\eta_{21} = \frac{\varphi_{\tilde{x},3} - \varphi_{\tilde{x},1}}{d} = \frac{\varphi_{\tilde{x},4} - \varphi_{\tilde{x}2}}{d} \tag{A.3.16}$$

where η_{11} and η_{22} are the normalised rotational axial deformation and η_{12} and η_{21} are the normalised rotational shear deformation in $\tilde{x}$ - and $\tilde{y}$ -direction respectively.

The loading in the diagonal connections is normalized by the connection length:

$$\eta_{D1} = \frac{\frac{\sqrt{2}}{2}\left(\varphi_{x,4} - \varphi_{x,1} + \varphi_{y,4} - \varphi_{y,1}\right)}{\sqrt{2}d} \tag{A.3.17}$$

$$\eta_{D2} = \frac{\frac{\sqrt{2}}{2}\left(\varphi_{x,2} - \varphi_{x,3} - \varphi_{y,2} + \varphi_{y,3}\right)}{\sqrt{2}d} \tag{A.3.18}$$

where η_{D1} is the bending deformation, normalised by the cell size, in the diagonal connection between node 1 and node 4 and η_{D2} is the bending deformation, normalised by the cell size, in the diagonal connection between node 2 and node 3.

Appendix 4: Dimensionless form of equations and scaling

To improve accuracy of the numerical calculation and study scaling effects, the equations of motion (equation 2.7-2.9 in this theses and the equations of motion presented by Suiker et al., 2001a) are rewritten in dimensionless form, such that all relevant parameters are of similar order of magnitude. The following dimensionless constants are hereto introduced, using scaling parameter b :

$$\eta = \frac{w}{b} \tag{A.4.1}$$

$$u_{\chi} = \frac{u_x}{b} \tag{A.4.2}$$

$$u_{\xi} = \frac{u_y}{b} \tag{A.4.3}$$

$$\chi = \frac{x}{b} \tag{A.4.4}$$

$$\xi = \frac{y}{b} \tag{A.4.5}$$

$$\tau = \sqrt{\frac{K_{s,axi} + 2K_{s,dia}}{M}}t \tag{A.4.6}$$

$$\tilde{d} = \frac{d}{b} \tag{A.4.7}$$

$$\tilde{I} = \frac{I}{a^2 M} \tag{A.4.8}$$

$$\tilde{K}_{nip,axi} = \frac{K_{nip,axi}}{K_{s,axi} + 2K_{s,dia}} \tag{A.4.9}$$

$$\tilde{K}_{sip,axi} = \frac{K_{sip,axi}}{K_{s,axi} + 2K_{s,dia}} \tag{A.4.10}$$

$$\tilde{K}_{nip,dia} = \frac{K_{nip,dia}}{K_{s,axi} + 2K_{s,dia}} \tag{A.4.11}$$

$$\tilde{K}_{sip,dia} = \frac{K_{sip,dia}}{K_{s,axi} + 2K_{s,dia}} \tag{A.4.12}$$

$$\tilde{K}_{s,axi} = \frac{K_{s,axi}}{K_{s,axi} + 2K_{s,dia}} \tag{A.4.13}$$

$$\tilde{K}_{s,dia} = \frac{K_{s,dia}}{K_{s,axi} + 2K_{s,dia}} \tag{A.4.14}$$

$$\tilde{G}_{r,axi} = \frac{G_{r,axi}}{b^2(K_{s,axi} + 2K_{s,dia})} \tag{A.4.15}$$

$$\tilde{G}_{r,dia} = \frac{G_{r,dia}}{b^2(K_{s,axi} + 2K_{s,dia})} \tag{A.4.16}$$

$$\tilde{G}_{t,axi} = \frac{G_{t,axi}}{b^2(K_{s,axi} + 2K_{s,dia})} \tag{A.4.17}$$

$$\tilde{G}_{t,dia} = \frac{G_{t,dia}}{b^2(K_{s,axi} + 2K_{s,dia})} \tag{A.4.18}$$

This dimensionless form of the equations of motion, using these parameters is:

$$\begin{aligned}
\frac{\partial^2 u_\chi}{\partial \tau^2}^{(m,n)} &= -\frac{1}{2}\tilde{K}_{nip,axi}\left(4u_\chi^{(m,n)} - 2u_\chi^{(m+1,n)} - 2u_\chi^{(m-1,n)}\right) \\
&-\frac{1}{2}\tilde{K}_{sip,axi}\left(4u_\chi^{(m,n)} - 2u_\chi^{(m,n-1)} - 2u_\chi^{(m,n+1)}\right) \\
&-\frac{1}{2}\tilde{K}_{nip,dia}\begin{pmatrix} 4u_\chi^{(m,n)} - u_\chi^{(m+1,n-1)} - u_\chi^{(m-1,n-1)} - u_\chi^{(m-1,n+1)} - u_\chi^{(m+1,n+1)} \\ -u_\xi^{(m+1,n-1)} - u_\xi^{(m-1,n-1)} + u_\xi^{(m-1,n+1)} + u_\xi^{(m+1,n+1)} \end{pmatrix} \\
&-\frac{1}{2}\tilde{K}_{sip,dia}\begin{pmatrix} 4u_\chi^{(m,n)} - u_\chi^{(m+1,n-1)} - u_\chi^{(m-1,n-1)} - u_\chi^{(m-1,n+1)} - u_\chi^{(m+1,n+1)} \\ -u_\xi^{(m+1,n-1)} + u_\xi^{(m-1,n-1)} - u_\xi^{(m-1,n+1)} + u_\xi^{(m+1,n+1)} \end{pmatrix}
\end{aligned} \tag{A.4.19}$$

$$\begin{aligned}
\frac{\partial^2 u_\xi}{\partial \tau^2}^{(m,n)} &= -\frac{1}{2}\tilde{K}_{nip,axi}\left(4u_\xi^{(m,n)} - 2u_\xi^{(m+1,n)} - 2u_\xi^{(m-1,n)}\right) \\
&-\frac{1}{2}\tilde{K}_{sip,axi}\left(4u_\xi^{(m,n)} - 2u_\xi^{(m,n-1)} - 2u_\xi^{(m,n+1)}\right) \\
&-\frac{1}{2}\tilde{K}_{nip,dia}\begin{pmatrix} 4u_\xi^{(m,n)} - u_\xi^{(m+1,n-1)} - u_\xi^{(m-1,n-1)} - u_\xi^{(m-1,n+1)} - u_\xi^{(m+1,n+1)} \\ +u_\chi^{(m+1,n-1)} + u_\chi^{(m-1,n-1)} - u_\chi^{(m-1,n+1)} - u_\chi^{(m+1,n+1)} \end{pmatrix} \\
&-\frac{1}{2}\tilde{K}_{sip,dia}\begin{pmatrix} 4u_\xi^{(m,n)} - u_\xi^{(m+1,n-1)} - u_\xi^{(m-1,n-1)} - u_\xi^{(m-1,n+1)} - u_\xi^{(m+1,n+1)} \\ -u_\chi^{(m+1,n-1)} + u_\chi^{(m-1,n-1)} - u_\chi^{(m-1,n+1)} + u_\chi^{(m+1,n+1)} \end{pmatrix}
\end{aligned} \tag{A.4.20}$$

$$\frac{\partial^2 \eta}{\partial \tau^2}^{(m,n)} = -\frac{1}{2}\tilde{K}_{s,axi}\begin{pmatrix} 8\eta^{(m,n)} - 2\eta^{(m+1,n)} - 2\eta^{(m,n-1)} - 2\eta^{(m-1,n)} - 2\eta^{(m,n+1)} \\ -\tilde{d}\varphi_{\chi}^{(m+1,n)} + \tilde{d}\varphi_{\chi}^{(m-1,n)} + \tilde{d}\varphi_{\xi}^{(m,n-1)} - \tilde{d}\varphi_{\xi}^{(m,n+1)} \end{pmatrix}$$

$$-\frac{1}{2}\tilde{K}_{s,dia}\begin{pmatrix} 8\eta^{(m,n)} - 2\eta^{(m+1,n-1)} - 2\eta^{(m-1,n-1)} - 2\eta^{(m-1,n+1)} - 2\eta^{(m+1,n+1)} \\ -\tilde{d}\varphi_{\chi}^{(m+1,n-1)} + \tilde{d}\varphi_{\chi}^{(m-1,n-1)} + \tilde{d}\varphi_{\chi}^{(m-1,n+1)} - \tilde{d}\varphi_{\chi}^{(m+1,n+1)} \\ +\tilde{d}\varphi_{\xi}^{(m+1,n-1)} + \tilde{d}\varphi_{\xi}^{(m-1,n-1)} - \tilde{d}\varphi_{\xi}^{(m-1,n+1)} - \tilde{d}\varphi_{\xi}^{(m+1,n+1)} \end{pmatrix} \qquad \text{(A.4.21)}$$

$$\tilde{I}\tilde{d}^2 \frac{\partial \varphi_x}{\partial \tau^2}^{(m,n)} = -\frac{1}{2}\tilde{K}_{s,axi}\begin{pmatrix} \tilde{d}\eta^{(m+1,n)} - \tilde{d}\eta^{(m-1,n)} + \tilde{d}^2\varphi_{\chi}^{(m,n)} \\ +\frac{1}{2}\tilde{d}^2\varphi_{\chi}^{(m+1,n)} + \frac{1}{2}\tilde{d}^2\varphi_{\chi}^{(m-1,n)} \end{pmatrix}$$

$$-\frac{1}{2}\tilde{G}_{r,axi}\left(4\varphi_{\chi}^{(m,n)} - 2\varphi_{\chi}^{(m+1,n)} - 2\varphi_{\chi}^{(m-1,n)}\right)$$

$$-\frac{1}{2}\tilde{G}_{t,axi}\left(4\varphi_{\chi}^{(m,n)} - 2\varphi_{\chi}^{(m,n-1)} - 2\varphi_{\chi}^{(m,n+1)}\right)$$

$$-\frac{1}{2}\tilde{K}_{s,dia}\begin{pmatrix} \tilde{d}\eta^{(m+1,n-1)} - \tilde{d}\eta^{(m-1,n-1)} - \tilde{d}\eta^{(m-1,n+1)} + \tilde{d}\eta^{(m+1,n+1)} + 2\tilde{d}^2\varphi_{\chi}^{(m,n)} \\ +\frac{1}{2}\tilde{d}^2\varphi_{\chi}^{(m+1,n-1)} + \frac{1}{2}\tilde{d}^2\varphi_{\chi}^{(m-1,n-1)} + \frac{1}{2}\tilde{d}^2\varphi_{\chi}^{(m-1,n+1)} + \frac{1}{2}\tilde{d}^2\varphi_{\chi}^{(m+1,n+1)} \\ -\frac{1}{2}\tilde{d}^2\varphi_{\xi}^{(m+1,n-1)} + \frac{1}{2}\tilde{d}^2\varphi_{\xi}^{(m-1,n-1)} - \frac{1}{2}\tilde{d}^2\varphi_{\xi}^{(m-1,n+1)} + \frac{1}{2}\tilde{d}^2\varphi_{\xi}^{(m+1,n+1)} \end{pmatrix} \qquad \text{(A.4.22)}$$

$$-\frac{1}{2}\tilde{G}_{r,dia}\begin{pmatrix} 4\varphi_{\chi}^{(m,n)} - \varphi_{\chi}^{(m+1,n-1)} - \varphi_{\chi}^{(m-1,n-1)} - \varphi_{\chi}^{(m-1,n+1)} - \varphi_{\chi}^{(m+1,n+1)} \\ +\varphi_{\xi}^{(m+1,n-1)} - \varphi_{\xi}^{(m-1,n-1)} + \varphi_{\xi}^{(m-1,n+1)} - \varphi_{\xi}^{(m+1,n+1)} \end{pmatrix}$$

$$-\frac{1}{2}\tilde{G}_{t,dia}\begin{pmatrix} 4\varphi_{\chi}^{(m,n)} - \varphi_{\chi}^{(m+1,n-1)} - \varphi_{\chi}^{(m-1,n-1)} - \varphi_{\chi}^{(m-1,n+1)} - \varphi_{\chi}^{(m+1,n+1)} \\ +\varphi_{\xi}^{(m+1,n-1)} - \varphi_{\xi}^{(m-1,n-1)} + \varphi_{\xi}^{(m-1,n+1)} - \varphi_{\xi}^{(m+1,n+1)} \end{pmatrix}$$

$$\tilde{I}\tilde{d}^2 \frac{\partial^2 \varphi_\xi}{\partial \tau^2}^{(m,n)} = -\frac{1}{2}\tilde{K}_{s,axi}\begin{pmatrix} \tilde{d}\eta^{(m,n+1)} - \tilde{d}\eta^{(m,n-1)} + \tilde{d}^2 \varphi_\xi^{(m,n)} \\ +\frac{1}{2}\tilde{d}^2 \varphi_\xi^{(m,n-1)} + \frac{1}{2}\tilde{d}^2 \varphi_\xi^{(m,n+1)} \end{pmatrix}$$

$$-\frac{1}{2}\tilde{G}_{r,axi}\left(4\varphi_\xi^{(m,n)} - 2\varphi_\xi^{(m,n-1)} - 2\varphi_\xi^{(m,n+1)}\right)$$

$$-\frac{1}{2}\tilde{G}_{t,axi}\left(4\varphi_\xi^{(m,n)} - 2\varphi_\xi^{(m+1,n)} - 2\varphi_\xi^{(m-1,n)}\right)$$

$$-\frac{1}{2}\tilde{K}_{s,dia}\begin{pmatrix} -\tilde{d}\eta^{(m+1,n-1)} - \tilde{d}\eta^{(m-1,n-1)} + \tilde{d}\eta^{(m-1,n+1)} + \tilde{d}\eta^{(m+1,n+1)} + 2\tilde{d}^2\varphi_\xi^{(m,n)} \\ -\frac{1}{2}\tilde{d}^2\varphi_\chi^{(m+1,n-1)} + \frac{1}{2}\tilde{d}^2\varphi_\chi^{(m-1,n-1)} - \frac{1}{2}\tilde{d}^2\varphi_\chi^{(m-1,n+1)} + \frac{1}{2}\tilde{d}^2\varphi_\chi^{(m+1,n+1)} \\ +\frac{1}{2}\tilde{d}^2\varphi_\xi^{(m+1,n-1)} + \frac{1}{2}\tilde{d}^2\varphi_\xi^{(m-1,n-1)} + \frac{1}{2}\tilde{d}^2\varphi_\xi^{(m-1,n+1)} + \frac{1}{2}\tilde{d}^2\varphi_\xi^{(m+1,n+1)} \end{pmatrix} \tag{A.4.23}$$

$$-\frac{1}{2}\tilde{G}_{r,dia}\begin{pmatrix} 4\varphi_\xi^{(m,n)} + \varphi_\chi^{(m+1,n-1)} - \varphi_\chi^{(m-1,n-1)} + \varphi_\chi^{(m-1,n+1)} - \varphi_\chi^{(m+1,n+1)} \\ -\varphi_\xi^{(m+1,n-1)} - \varphi_\xi^{(m-1,n-1)} - \varphi_\xi^{(m-1,n+1)} - \varphi_\xi^{(m+1,n+1)} \end{pmatrix}$$

$$-\frac{1}{2}\tilde{G}_{t,dia}\begin{pmatrix} 4\varphi_\xi^{(m,n)} + \varphi_\chi^{(m+1,n-1)} - \varphi_\chi^{(m-1,n-1)} + \varphi_\chi^{(m-1,n+1)} - \varphi_\chi^{(m+1,n+1)} \\ -\varphi_\xi^{(m+1,n-1)} - \varphi_\xi^{(m-1,n-1)} - \varphi_\xi^{(m-1,n+1)} - \varphi_\xi^{(m+1,n+1)} \end{pmatrix}$$

The Kelvin foundation is included by adding the term $-\tilde{k}_{Kelvin}\eta$ to the right-hand side of equation (A.4.21). Where:

$$\tilde{k}_{Kelvin} = \frac{k_{Kelvin}}{K_{s,axi} + 2K_{s,dia}} \tag{A.4.24}$$

The effect of scaling can be studied with the dimensionless form as starting point. Simulations on different scales would be obtained by multiplying results of solving the dimensionless equations of motion with a different scaling parameter b. The effects of scaling are compared in this Appendix with Froude scaling factors, which are presented in Table A4-1.

.

Table A4-1: Froude scaling factors

Parameter	**Scaling factor**
Length	λ
Time	$\sqrt{\lambda}$
Force	λ^3
Moment	λ^4
Mass	λ^3
Angle	1
Modulus of Elasticity	λ

All length parameters in the dimensionless form are scaled with factor b, in line with Froude scaling if scaling factor λ is substituted for b.

Stiffnesses of normal and shear springs scale with factor $K_{s,axi} + 2K_{s,dia}$, which according to equation 2.23 in the main body of the thesis is k^2Gh. h is a length parameter and scales with factor b. k is dimensionless and $G = E/2(1+\nu)$. This parameter scales with the same factor as the modulus of elasticity, λ, and therefore with factor b if λ is substituted for b. The stiffnesses of normal and shear springs therefore scale with factor b^2. With the same logic, the stiffnesses of rotational and torsional springs scale with factor b^4.

Time scales with a factor related to the square root of $K_{s,axi} + 2K_{s,dia}$, which scales with factor b^2, divided by M. Here $M = \rho hd^2$. No scaling is applied on density and therefore M scales with factor b^3, due to the length parameters h and d. Scaling of time is therefore with factor $\sqrt{b}$, in line with Froude scaling if scaling factor λ is substituted for b.

Force is made dimensionless in the numerical model as follows:

$$\tilde{F} = \frac{F}{b\left(K_{s,axi} + 2K_{s,dia}\right)} \qquad \text{(A.4.25)}$$

And scales therefore with a factor b^3, again in line with Froude scaling if scaling factor λ is substituted for b.

Moment is made dimensionless in the numerical model as follows:

$$\widetilde{Mom} = \frac{Mom}{b^2\left(K_{s,axi} + 2K_{s,dia}\right)\tilde{a}^2\tilde{l}} \tag{A.4.26}$$

And using the same logic as for the other parameters scales with a factor b^4, in line with Froude scaling if scaling factor λ is substituted for b

The Kelvin foundation scales with factor b^2. The density of water and gravity keep the same value and the cell size d adjusts with the scaling factor that is used, agreeing with scaling factor b^2.

In this Appendix it is shown how the equations of motion of the lattice model are translated in dimensionless form. Based on this dimensionless form, it is shown that the behaviour of the lattice model is in agreement with Froude scaling laws. Therefore, there is no difference in results when comparing full scale lattice model results with model test results that were scaled with Froude scaling laws, compared to comparing results obtained and simulated on model scale.

Acknowledgements

Before this book ends, there are a few people I should mention, without whom I would never have been able to successfully complete this PhD study.

This project was a collaboration between Shell and TU Delft, set up by Guido Kuiper, Mitch Winkler and Andrei Metrikine. After I indicated being interested in doing a PhD study in combination with a job as Offshore Structures engineer at Shell, they identified the research topic and set-up the collaboration. Mitch is very experienced in running Arctic projects provided business support and made sure I could continue working on the project even when the interest in Arctic projects reduced in Shell. Guido supervised the project and gave me great input and advice. He was very supportive throughout the project and quick with reviews with very helpful feedback. Later on in the project Frank Lange joined as additional supervisor and gave good input on the approaches for my research. Andrei taught me about lattice models, how to set them up and verify them. This formed the basis of the project. Throughout the project he provided good feedback and ideas and improved my writing skills. The time and effort that he spend supporting me with finalizing the thesis helped me reach the finish line and I appreciate this very much.

Most weeks I worked 3-4 days in the Shell office in Rijswijk and 1-2 days in the Arctic Room at TU Delft, named after the research topic the majority of people in the room were doing. I already miss the coffee breaks where we discussed the broadest range of topics. Thanks to Chris, Hayo and Marnix for providing input to my work and for the good discussions we had.

In Shell all my colleagues were very supportive of me not working on Shell projects for 2 days per week. I appreciate that people tried very hard not to plan meetings on my TU Delft days. I also appreciate the interest shown by my colleagues in the progress and the results I had found.

A number of researchers provided input to my PhD. There are many who inspired me with their publications. Erland Schulson gave me some great advise when I asked him if I could use a figure from his paper in a publication, resulting in a drastic change of Chapter 4 and a few weeks delay on the delivery of my PhD, but a better end result. I would like to thank Prof. Marchenko and Prof. Sammonds for taking me on a cruise to Svalbard to see real ice-structure interaction.

Outside my PhD there are many friends and family members who I should thank for providing the necessary distraction from my work and PhD from time to time. I believe that it is important to take proper breaks and friends and family found great ways to fill those breaks: cycling, drinking, concerts, lunch…

My parents supported me throughout the project and encouraged me to do the PhD and not to worry about the effect on my career. I am very glad they were so supportive and interested in the progress. They also introduced me to ice-structure-interaction, as shown on the cover of the thesis.

And finally the one who suffered the most from this adventure: Kevin. I could not thank you more for your patience and support in difficult times. I am convinced that I would not have finished this thesis without you.

Curriculum Vitæ

Renate van Vliet was born in Leiderdorp, The Netherlands on September 12th, 1987. After finishing her secondary education at the Visser 't Hooft Lyceum in Leiden in 2005, she studied Civil Engineering at Delft University of Technology. During her bachelor education she started working as student-assistant Structural Mechanics. After completing the bachelor education in three years, she spent a year as treasurer in the board of Study association Het Gezelschap "Practische Studie", where she was involved in budget preparation and monitoring for the study association for Civil Engineering students and supervised several committees.

Hereafter she followed a master in Structural Engineering, during which she did an internship in Perth, Australia in an engineering office specialized in coastal, port and harbour engineering called JFA Consultants, where she was involved in numerical modelling of the building process of a breakwater. She enjoyed experiencing a different country and culture and the year after she went to Vietnam to study flooding problems in Ho Chi Minh City with a project team from TU Delft. During an internship at Shell Projects and Technology in Rijswijk, she wrote her master thesis titled "Design and numerical modelling of cooling water intake risers for deep ocean applications". She graduated in 2012.

Renate joined Shell Projects and Technology as Offshore Structures Engineer after her graduation, where she worked on the design of several floating production systems. She performed numerical analysis of global motions and mooring and riser loads as well as analysis of hydrodynamic and ice loading on both fixed and floating offshore structures. She performed several basin tests campaigns and she represented Shell in a number of joint research projects. At Shell she followed Graduate and Advanced Technical programme courses for offshore structures discipline engineers.

Renate enjoyed working on her master thesis and was interested to continue doing research. Colleagues in Shell Projects and Technology and Shell International Exploration and Production Inc. as well as TU Delft supported this and she commenced a part-time PhD study in prediction of ice failure in interaction with sloping structures in 2013. During her PhD study, she supervised several MSc students and was involved in a number of Arctic research projects as company representative.

At present, Renate works as project engineer for Penguins Redevelopment project at Shell UK Limited in Aberdeen where she is responsible for delivery of the anchors and mooring system.

List of publications

van Vliet, R., Metrikine, A.V., 2017. Derivation and verification of a lattice model for bending vibration of a plate. J. Appl. Math. Mech.

Metrikine, A.V., Kudarova, A.M., Hoving, J.S., **van Vliet, R.,** 2015. On the minimization of wave reflection at the interface of a discrete system and a dispersively similar continuum. J. Sound Vib. 346, 191–199.

van Vliet, R., Metrikine, A.V., 2017. Simulating Interaction Between Level Ice and Conical Structures with a 2D Lattice Model, in: Proceedings of the 24th International Conference on Port and Ocean Engineering under Arctic Conditions. pp. POAC17-057.